FLOW PATTERN TRANSITIONS IN OIL-WATER FLOWS PAST A BLUFF BODY

Kyeong Hyeon Park

Ph.D Thesis

ThAMeS Multiphase Group
Department of Chemical Engineering
University College London

2018

Declaration

I, Kyeong Hyeon Park, declare that the work presented in thesis is the result of my own work. Where information has been consciously derived from other sources, as to show previous work, present the author's result, make comparison etc… I confirm that this is indicated in the text.

I further state that no substantial part of my thesis has been submitted, or, is being concurrently submitted for any such degree.

Kyeong Hyeon Park
Sept 2018

Acknowledgements

First of all, I would like to express my sincere gratitude to Professor Panagiota Angeli for giving me constant encouragement and close guidance throughout the period of my PhD. A journey in completing a PhD is certainly not an easy process for the majority of people and I was no exception. I sometimes had difficult times but thanks to her patience and waiting, and precious time she devoted on the project, the writing of this thesis was less stressful than expected. My research project has been supported by the EPSRC Programme Grant MEMPHIS. I would like to acknowledge UCL for my studentship which I feel grateful. I thank all the members of ThAMeS Multiphase group under the supervision of Prof. Angeli for the joy, conversation and drinks shared. I would like to thank especially the members from within the walls of LB21a, Dr Maxime Chinaud, Dr Victor Volgaropoulos, Mr Mohd Izzudin Izzat Zainal Abidin, Dr Alberto Barral and Dr Lawrence Edomwonyi-Otu, for all the help and support. I would like to thank Dr Simon Barras and Mr Mike Gorecki for the technical support of instruments and ensuring the safety of the laboratory environment. I also would like to thank Mr Erich Hermann and the departmental workshop team for their kind help with the rig and the design of the inlets. The support from Mr Martyn Vale and his IT team is also appreciated. Finally and most importantly, I would like to thank my family for their encouragement and trust throughout the course of my studies, especially to my mother for her everlasting love and care.

Abstract

In this Thesis a novel approach is followed to facilitate the experimental investigations on the flow pattern transitions from separated to dispersed flows using a cylindrical bluff body in horizontal oil-water flows. A transverse cylindrical rod is used as a bluff body which is placed under the interface of the two immiscible liquids and near the test section inlet to passively generate interfacial perturbations and breaking waves. This approach was inspired from the use of hydrofoils in ships that reduce frictional drag via increased air entrainment. Studies are carried out using two flow facilities and high speed imaging combined with laser based measurements are performed at two axial locations along the test section, immediately after the cylinder and at large distance away from the cylinder. The effect of a confined geometry on the characteristics of the von Karman vortices and on the general flow behaviour immediately downstream of the cylinder are investigated in single phase water flows. It is found that the 3D pipe geometry does not affect significantly the vortex shedding behind the cylinder at least in the central plane of the pipe. The frequencies of the vortex shedding were comparable to those from a cylinder in an unconfined liquid. The results from two phase flows reveal that the cylinder reduces the mixture velocity for the transition separated to dispersed flows. It also actuates interfacial waves that are found to be non-linear and convective. In many cases the waves have the same frequencies as the von Karman vortices depending on the submergence depth of the cylinder underneath the oil-water interface and on the Froude number of the water layer. The observations suggest that strongly non-linear waves are responsible for forming thin ligaments that eventually break up into droplets.

Impact Statement

Research on the flow dynamics and flow pattern transitions in liquid-liquid pipe flows have been rather limited compared to other multiphase flows and particularly gas-liquid ones. Most generally the studies from the past and present were intended to improve the safety and efficiency of crude oil production and transportation. As part of the enhanced oil recovery often water is injected into the well to maintain the pressure and this in return increases the overall amount of water in the mixture that needs to be transported. The presence of water flowing along with oil caused a significant interest in further investigating the behaviour of oil-water mixture. Early studies revealed the presence of water, more specifically in annular flows, could reduce pressure drop during the transportation of heavy oil over long distances. In addition, it is well known that when oil-water flow together in a confined geometry, different flow patterns occur and they can be associated to the pressure drop and other transport properties such as the mass and heat transfer rates. The current Thesis aimed to develop a novel way to aid the study of the transitions between different flow patterns in general as well as to control the transitions using a cylindrical bluff body.

The obtained experimental data and the findings from this Thesis could be used in several ways and can be split into two categories; 1) research and 2) industry. In research, the current work can be attributed towards improving the physical understanding of the phenomena that govern the flow pattern transitions. In addition, the experimental techniques and the data analysis procedures developed in the current work may be applied in other research fields. The gathered data will be valuable to researchers and industrialists (mainly in oil and gas) to validate the developed models. In industries, generation of dispersion and droplet detachment using a cylindrical bluff body can find applications during transportation of multiphase mixtures in oil industry. The findings from this Thesis is not limited to oil and gas industries - considering different industrial areas, presence of the bluff body enhances mixing inside pipes and can be used in mixing in process units and heat exchangers. In addition, the findings can be useful for building designs such as bridges or pipelines under installed on the sea bed.

Contents

List of Figures

List of tables

List of Symbols

All symbols used in this Thesis are explained in the text. However, a list of most used symbols is presented below for convenience.

A	Area
a_L	Ligament radius
D	Cylinder diameter
f	Frequency
FFT	Fast Fourier Transform
Fr	Froude number
g	Gravitational force
h	Distance between the top of the cylinder and the interface
H	Distance between the bottom of the cylinder and the wall
h*	Depth of submergence
HHT	Hilbert Huang Transform
i, j, k, x_m	Subscripts
N, M, P	Number of data / intervals
IMF	Intrinsic Mode Function
L	Distance between two parallel walls
n	Refractive index
PSD	Power spectrum density
Q_o	Volumetric oil flow rate
Q_w	Volumetric water flow rate
r	Oil-water input flow rate ratio
Re	Reynolds number
Re_{crit}	Critical Reynolds number
St	Strouhal number
STDV	Standard deviation
t	Time
u	Phase velocity

Umax	Maximum phase velocity
Umix	Mixture velocity
Uref	Reference frame velocity
Uso	Superficial oil velocity
Usw	Superficial water velocity
Uw	Actual water phase velocity
V	Average wave velocity
γ	Gap ratio
γ_{crit}	Critical gap raio
μ	Viscosity
π	Pi
ρ	Density
Γ	Average circulation
τ	Instantaneous time
$\overline{h}_{x_m}$	Local average interface height
$\overline{A}_{x_m}$	Local average wave amplitude
$\overline{v}_{x_{mn}}$	Local wave velocity
$h_{x_m,i}$	Local interface height of an interval
ω_z	Vorticity
$A_{x_m,j}$	Local wave amplitude of an interval
λ_{x_m}	Local average wavelength
λ_2	Parameter discriminating the regions of swirling and shearing

CHAPTER 1. INTRODUCTION

1.1 Background

Two phase liquid-liquid flows are commonly encountered in many industries and one of the well-known examples is found during the production of crude oil. Oil reservoirs are usually found deep underground or in deep sea beds where the oil is usually kept within the layers of porous rocks under pressure. The existing pressure within the reservoir can be used to push the fluids out through an artificially drilled hole. However, overtime, the pressure inside the reservoir gradually decrease. In order to overcome this, a recovery mechanism which is commonly used is injection of other fluids, usually water, to displace what is inside the production well. As most wells mature, the water/oil ratio inevitably increases with production and the ratio can be as high as 3 barrels of water per barrel of oil produced (Bailey et al., 2000); this means that both oil and water flow inside pipelines simultaneously during transportation.

Owing to this fact, a large number of studies have been conducted to understand the flow behaviour of oil-water mixtures which include the identification and boundaries of flow patterns. The term flow pattern refers to different geometrical distribution of the phases as they flow together inside a pipe. Flow patterns are usually identified from visual observations and different names have been reported for similar patterns from different researchers (Russel et al., 1959; Malinowsky, 1975; Oglesby, 1979; Trallero, 1995; Angeli and Hewitt, 1998; Shi and Jepson, 1999). However, classically the patterns can be categorized into two groups depending on the presence of droplets of either phase; namely separated to dispersed flow. Stratified flow is characterized by either smooth or wavy interface without any appearance of droplets. Both oil and water phases retain their continuity where the heavier phase is found at the bottom of the pipe and the lighter phase (usually oil) on the top. On the other hand, non-Stratified flow refers to any pattern where either or both drops of oil and water appear, and the transition is considered to have taken place when the first few drops appear. This flow pattern transition, usually for a given system occurs as the phase velocities are increased.

It is known that each flow pattern affects the essential flow characteristics such as the pressure drop, velocity, holdup profiles as well as transport properties such as the mass and heat transfer coefficients along pipes. Therefore being able to accurately predict and identify the pattern is very important. However, the detailed mechanisms of flow pattern transition from separated to dispersed flow is not fully understood and experimental data is rather limited. The investigations on drop entrainment in liquid-liquid systems is relatively limited in comparison to gas-liquid flows. Brauner and Maron (1989;

1992a, b) and Trallero (1995) suggested the drop entrainment from one phase into another happens as drops detach from the waves in stratified wavy flows. Such waves are generated due to Kelvin-Helmholtz (KH) instability, which is caused by the difference between the velocities of the two immiscible phases. These works served as the starting point for further investigations on the drop detachment from interfacial waves.

Later, Al-Wahaibi and Angeli (2007a, b) suggested a stability criterion of waves at given flow rates. The model was used to predict whether the waves with a certain wavelength and amplitude are stable or not. A mechanism describing the drop formation unstable waves were also proposed. In the proposed model drops detached from waves when the drag force caused by the differences in velocities of the two phases is greater than the stabilizing surface tension force. The author performed further experimental studies to validate the model although later results by Al-Waihaibi and Angeli (2011) were inconclusive. Other experimental works have also been performed to look into the stability of the waves in terms of the flow parameters (Barnea and Taitel, 1993; Trallero, 1995; de Castro and Rodriguez, 2015; Barral et al., 2015; de Castro et al., 2015) although information on the drop formation mechanism from waves is still incomplete.

In general it is challenging to study experimentally the breakage of drops from waves. This is because at the beginning of the transition only a few drops form from the breaking waves while the exact breakage location along the pipeline is not known. Firstly previous literature and data for oil-water flow in pipes are rather scattered and they are difficult to correlate (as the flow is characterised by many interrelated factors including physical properties of the fluids, pipe diameter and roughness, inclination / declination angle of the pipe and velocities of each fluid) which makes it difficult to model the phenomena.

1.2 Motivation and objectives

One possible way to facilitate the experimental studies on the flow pattern transition from separated to dispersed flow is spatially localise the formation and breakage of waves. This can be achieved through the use of a bluff body.

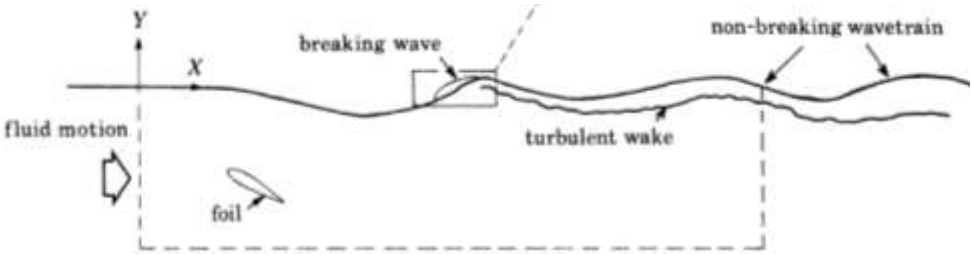

Figure 1.1 Breaking waves behind a hydrofoil (Duncan, 1981)

The motivation of using a bluff to localise the onset of droplet detachment came from the work of Duncan (1981) who studied the effect of a hydrofoil on the creation of breaking waves behind it (Figure 1.1). Hydrofoils are used to induce breaking waves and generate bubbles and thus reduce frictional drag in applications such as e.g. design of ships. As the hydrofoil moves horizontally across the fluid, the flow around the hydrofoil is deflected downward towards the end tip of the foil. This flow motion leads to low pressure region on the upper part of the foil which disturbs the interface to generate waves. For this study a round cylindrical rod was chosen instead as an initial design of the bluff body since flows around a circular bluff body is generally better understood.

The main goal of this thesis is to study the transition from stratified to non-stratified flows, focusing on the onset of droplet detachment through passive actuation of the interface using a spatially fixed cylindrical bluff body. Through localisation of the transition phenomena from stratified to non-stratified flows, the current work enables to gather reliable data and gain deeper insight into the mechanism of the flow pattern transition.

In this Thesis the main objectives are as follows:

- Passively actuate the flow pattern map using a bluff body and identify the boundaries between stratified and non-stratified flows. i.e shift the flow pattern transition boundary.
- Generate spatially localised breaking waves and obtain quantitative information on their characteristics (e.g wave amplitude, frequency, wavelength, velocity).
- Describe the mechanism of interfacial wave generation and droplet detachment from it.

1.3 Thesis outline

The thesis consists of a total of 7 Chapters. Chapter 2 reviews the literature related to the current topic and it entails 3 sub-sections. The first section gives a summary of previous works conducted on liquid-liquid as well as gas-liquid flows along with details on the previously established flow patterns and measuring techniques. Works conducted on the flow around a circular cylinder and different parameters affecting the flow features in the cylinder wake are discussed in the second section. This work is used to guide the design of the bluff body used in this work. Relevant studies on the ligament breakup and formation of droplets are briefly discussed in the last section of this Chapter. Chapter 3 gives detailed description of the experimental setup and the data analysis procedures. Measurement techniques implemented to obtain wave characteristics and flow fields in the wake of the cylinder are given. Systematic error analysis on the measuremenst using PIV is discussed at the end of the Chapter.

There are 4 results Chapters presenting the results of the thesis. In Chapter 4 preliminary results on the actuation of flow pattern transitions and localised interfacial wave characteristics downstream of the cylinder, such as the average interface height, wave amplitude, wave velocity, wavelength and wave frequency, obtained via high speed imaging are presented. In Chapter 5 results obtained using PIV to

study the flow fields immediately downstream of the cylinder are presented and discussed. Details on the vortex structures in the vicinity of the cylinder in single and two-phase flows, and interaction between the interface and the vortex structures in two phase flows are discussed. However, for flow conditions in two phase flow where the generated waves were strongly non-linear, the velocity fields near the interface were not obtainable due to the mismatch of the refractive indices of the fluids. To overcome this issue, investigations using the test fluids with matched refractive indices were conducted and the results obtained via simultaneous Particle Image Velocimetry / Planar Laser Induced Fluorescence is given in Chapter 6 and 7. Interactions between the cylinder and the approaching flows with both smooth and non-smooth interface are discussed. Wave characteristics obtained just downstream the cylinder are compared with the interfacial characteristics further downstream from the test-section inlet. The effect of the cylinder on breaking waves and ligament formation is also briefly discussed. Finally Chapter 8 summarizes the work presented in the thesis and recommendations for future works are given.

CHAPTER 2. LITERATURE REVIEW

2.1 Two-phase pipe flows

In this section relevant experimental and theoretical studies conducted on liquid-liquid horizontal pipe flows are discussed and presented focusing on flow patterns identification and flow pattern transitions focusing in particular on the transition boundary from stratified to non-stratified flow regions.

2.1.1 Flow patterns and flow pattern map

2.1.1.1 Flow patterns

When two immiscible fluids flow together inside a pipe, the fluids can form different flow patterns. For a system with fixed geometry (pipe diameter, material, inclination of the pipe and inlet configuration), the flow pattern is usually determined by the flow parameters (mixture velocity and relative velocities between the two phases) and the physical properties of the fluids (viscosity, density and surface tension).

A large number of investigations have been carried out to identify the different flow patterns. In early years, only three to four patterns were identified (Russel et al., 1959; Malinowsky, 1975) and very soon after up to 14 different patterns were reported by Oglesby (1979). Since the 90s, the instruments and technology allowed researchers to observe patterns more accurately and to analyse them in more detail (Trallero, 1995; Angeli and Hewitt, 1998; Shi and Jepson, 1999). The most commonly appearing flow patterns based on published and acquired data are presented by Trallero (1995) shown in Figure 2.1 and are the following:

- Stratified flow (ST)
- Stratified flow with mixing at the interface (ST&MI)
- Dispersion of oil in water with a simultaneous layer of water (Do/w &w)
- Dispersion of oil in water emulsion (Do/w)
- Dispersion of water in oil and oil in water simultaneously (Dw/o & Do/w)
- Dispersion of water in oil emulsion (Dw/o)

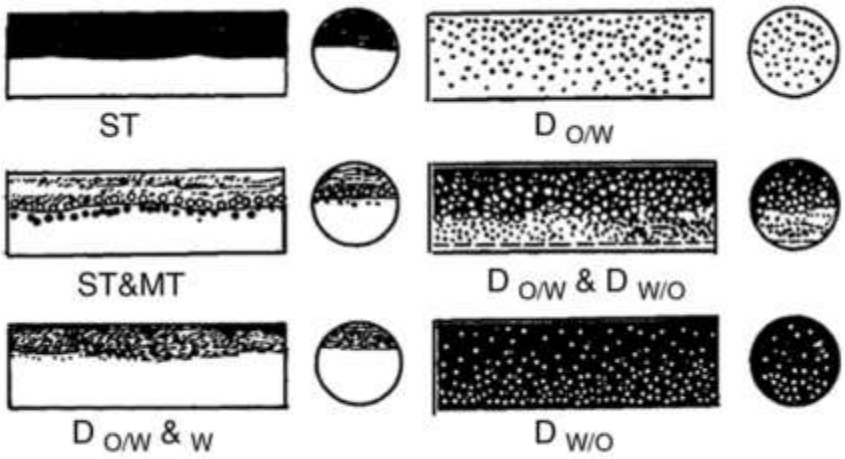

Figure 2.1 Oil-water flow patterns (Trallero, 1995)

2.1.1.2 Flow pattern classification

Over time, improvements have been made in understanding the flow patterns with enhanced measurement techniques. Despite this, some flow patterns are however more difficult to categorise than others as there is no quantitative decision boundary to differentiate between them and the decision can be quite tricky and subjective. Some similar patterns were called differently by different people, for example, stratified with mixing at the interface pattern of Trallero (1995) was called semi-segregated by Oglesby (1979) which again was referred as stratified wavy with droplets / entrainment by Soleimani (1999) and Angeli and Hewitt (2000). Lovick and Angeli (2004) later categorized ST&MT, Do/w&Dw/o and Do/w defined by Trallero (1995) as a single flow pattern and referred as Dual Continuous regime (DC). Even today there are no quantitative guidelines or set boundaries to follow in order to experimentally discriminate the patterns. The decision on which flow pattern a flow will be categorised is still subjective, although it is true that better instruments are available these days to make quantitative comparison between different patterns.

The flow patterns observed by Trallero (1995) were however restricted to low or medium viscosity oils (μ_o/μ_w <100) where μ_o and μw are the viscosity of oil and water respectively. The flow patterns are however different in systems with high viscosity oils (heavy crude oil). From the experiment conducted at China University of Petroleum, Mu (2001) have suggested a new classification of flow patterns for heavy oil-water flows, with oil-to-water viscosity ratio μ_o/μ_w of 310, and the patterns include ST & MI, Comprehensive ST with both oil and water phase are dispersed at the upper part of the pipe while the water phase remains segregated and is free from drops, Water-Core Annular, Slug and Dispersion Flow. Further research on flow patterns using heavy crude-oil was conducted by Yao and Gong (2004) and Yao (2006) with a more viscous oil (μ_o/μ_w = 572). They found 10 kinds of patterns in total and they were divided into 4 categories which were 1) oil dominated; 2) water dominated; 3) intermittent flow region and 4) segregated flow region. Similarly, using heavy crude-oil with μ_o/μ_w = 488, Bannwart et al (2004) identified flow patterns in both vertical and horizontal pipe flows. The observed patterns in

horizontal flows were similar to the patterns observed by Mu (2001) and patterns observed in vertical flows were very similar to gas-liquid flow patterns observed by Taitel et al. (1980). Extensive review in the area of flow pattern determination in early days of study is given by Valle (1998) for mainly low viscosity oils $\mu_o/\mu_w < \sim 30$ and a most recent review is given by Ibarra et al. (2014) for flow patterns in both horizontal and slightly inclined pipes. General review on the dynamics and characteristics of oil-water flows in pipes is well described by Ismail (2015). Summary of experimental studies conducted on horizontal oil-water pipe flows are given in Table 2.1.

Table 2.1 Summary of experimental studies on horizontal oil-water pipe flows

Author	Diameter (cm)	Pipe material	μ_o/μ_w	ρo/ρw	Measurement techniques	Data collected
Russel et al. (1959)	2.03	CAB	20.13	0.84	Visual observation	Flow patterns Hold-up Pressure drop
Guzhov et al. (1973)	3.94	Steel	21.8	0.898	Visual observation	Flow patterns Pressure drop
Oglesby (1979)	4.1	Steel	32, 61, 167	0.895, 0.863, 0.870	Visual observation	Flow patterns
Kurban and Angeli (1995)	2.43, 2.4	Glass, Acrylic	1.6	0.803	Conductivity probe	Flow patterns
Trallero (1995)	5.01	Acrylic	30	0.850	Visual observation	Flow patterns Pressure drop Hold-up
Trallero and Brill (1996)	5.08	Acrylic resin	29.7	0.852	Visual observation	Flow patterns
Nädler and Mewes (1997)	5.9	Perspex	18-35	0.848	Visual observation	Flow patterns
Vedapuri and Jepsen (1997)	10.12	Plexiglass	2			Flow patterns
Valle (1997)	7.62	Steel	1		Impedance probe	Flow patterns
Valle (1998)	3.75	Glass	2.55			Flow patterns
Angeli and Hewitt (1998)	2.43, 2.4	Stainless steel, Acrylic resin	1.6	0.803	Impedance probe	Flow patterns
Angeli and Hewitt (2000)	2.43, 2.4	Steel, Acrylic resin	1.6	0.803	Photography and conductivity probe	Flow patterns
Elseth (2001)	5.63	Stainless steel	1.6	0.790	Visual observation Gamma densitometer	Flow patterns
Mu (2001)	2.54	Steel	310	0.93	Visual observation	Flow patterns
Lovick and Angeli (2004)	3.8	Stainless steel	5.5	0.828	Visual observation Impedance probe	Flow patterns
Yao and Gong (2004)	2.54	Steel	572	0.973	Visual observation	Flow patterns
Ioannou et al. (2005)	6, 3.8	Steel, Acrylic	1.7	0.796	Impedance probe	Pressure drop Phase inversion

Raj et al. (2005)	2.54	Acrylic	1.2	0.787	Visual observation	Flow patterns
Rodriguez and Oliemans (2006)	8.28	Steel	7.5	0.830	Visual observation Gamma densitometry	Flow patterns Hold-up
Yao (2006)	2.54	Steel	572	0.973	Visual observation	Flow pattern
Al-wahaibi (2006)	1.4, 3.8	Acrylic	5.5	0.828	Visual observation Conductance probe	Flow pattern Onset of entrainment
Hu (2007)	3.8	Stainless steel	5	0.828	Impedance probe Hot-film anemometry	Drop size distribution
Ngan et al. (2011)	3.8	Acrylic	5.5	0.828	Conductance probe	Wave characteristics
Rodriguez and Baldani (2012)	2.6	Glass	2.8	0.828	Visual observation	Pressure drop Hold-up
Barral (2014)	3.8	Acrylic	5.5	0.828	Visual observation Conductance probe	Flow patterns Wave characteristics
Park et al. (2017)	3.7	Acrylic	5.5	0.828	Visual observation	Flow patterns Wave characteristics
Chinaud et al. (2017)	2.7	Acrylic	5.5	0.828	Visual observation PIV	Flow patterns Velocity field

2.1.1.3 Flow patterns – measurement technique

A number of measurement techniques have been used to identify the different flow patterns, however even today flow pattern identification relies heavily on visual observation and optical measurements. Other methods include use of conductance and impedance probes and as well as various types of tomography systems.

Visual observation and optical measurements

Visual observations have been the far most widely used methods for flow pattern identification (Russel et al., 1959; Guzhov et al., 1973). Commonly this technique entails observing the flow through a transparent window in the pipe. For flow systems with high flow rate or for rapid phenomena, a high-speed camera is used to record the flow and captured images or videos are analysed to identify the flow pattern. However, use of the high-speed camera is often not sufficient to identify a flow pattern and give clear description. This is because usually the recording is done from outside the pipe, and clear view of the flow near the pipe centre is often obscured, while mismatch of the refractive indices between the test fluids and the pipe material promotes optical distortion especially near the pipe wall close to interfaces. Liu et al. (2006) have used Planar Laser Induced Fluorescence (PLIF) to investigate flow pattern transitions in liquid-liquid flows in vertical pipes and studied the flow patterns at the central plane of the pipe. More recently, Voulgaropoulos and Angeli (2016) implemented simultaneous PLIF and PIV to study the evolution of dispersed flow in horizontal pipe flows.

Conductance probes

Conductance probes, especially double-wired conductance probes, have been used extensively to study gas-liquid flows for measuring film thicknesses and film characteristics in annular flows (Azzopardi 1997; Wang et al., 2004; Kadri et al., 2009). The wave characteristics such as frequency can be calculated from the obtained conductivity signal via power spectrum analysis. Several authors have attempted to predict the flow patterns by analysing the conductivity signals in both liquid-liquid flows (Jin et al., 2003; Du et al., 2012) and in gas-liquid flows (Hernandez et al., 2006; Sun et al., 2011). In many cases for non-stratified flows the signals were non-stationary and rather chaotic hence complex mathematical techniques were implemented for the analysis. Similar to studies conducted in annular flows for gas-liquid flows, several authors also have used the conductance probe to study wave characteristics mainly for heavy crude oil in annular flows (Oliemans, 1986; Bai, 1995; Bannwart, 1998; Rodriguez and Bannwart, 2006) while Chakrabarti et al. (2006) have used double-wired probes to predict phase inversion.

Other techniques

Angeli and Hewitt (2000) have used a camera attached to an endoscope to identify flow patterns and measured drop size distributions at different vertical locations inside the pipe. Electrical resistance tomography (Ngan et al., 2011), gamma densitometry (Soleimani, 1999; Elseth, 2000; Oddie et al., 2003), x-ray (Schümann et al., 2016) and impedance probes (Lovick and Angeli, 2001ab) have all been used to identify flow patterns.

2.1.1.4 Flow pattern map

The observed flow patterns are often presented in terms of a *flow pattern map*, a graphical representation of the patterns observed for a range of flow condition. There are a number of different ways of presenting the map. Superficial velocities of the two phases are commonly used as the x-axis and y-axis respectively (Al-Wahaibi et al., 2007; Figure 2.2). Alternatively, the input flow rate ratio, which is the ratio between the superficial input oil flowrate and the superficial water flowrate given as Uso/Usw , can be used (Barral et al., 2013, Figure 2.3) or the water or the oil cut can be plotted against the mixture velocity (Figure 2.4 and 2.5). In general, each *point* on the graphical representation of the flow pattern map must be distinguishable from the others in order to draw a clear boundary between the patterns although in some cases only the transition boundaries are marked shown using solid lines (Figure 2.3).

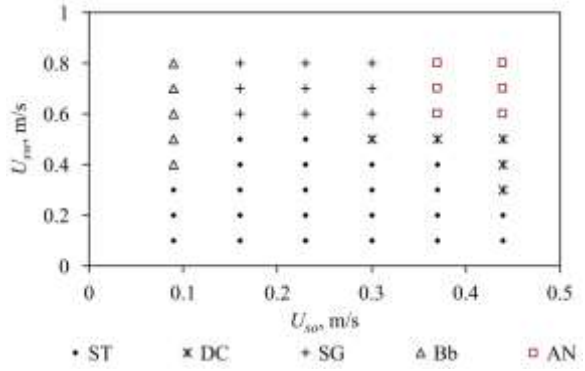

Figure 2.2 Flow pattern map for as a function of superficial oil and water flowrates (Al-wahaibi et al., 2007)

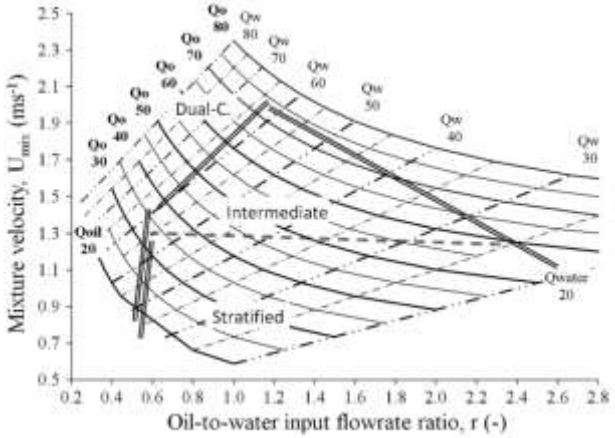

Figure 2.3 Flow pattern map as a function of mixture velocity and oil-to-water input flowrate ratio (Barral and Angeli, 2013)

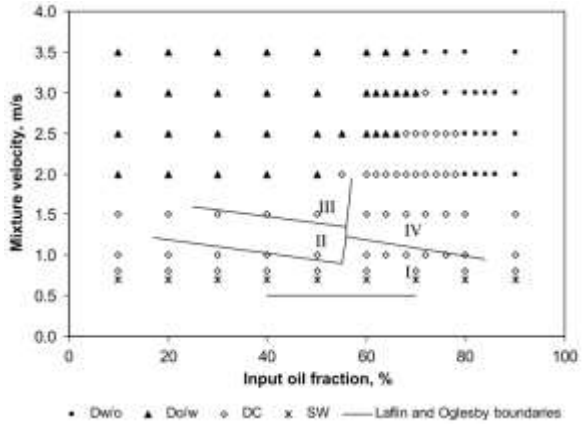

Figure 2.4 Comparison of the experimental flow pattern map with the results from Laflin and Oglesby (1976) (solid lines) (Lovick and Angeli, 2004)

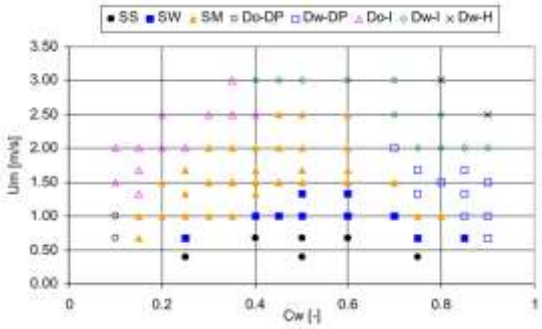

Figure 2.5 Flow patterns as functions of mixture velocity and input water cut (Elseth, 2000)

2.1.2 Interfacial wave characteristics and wave stability

ST flow is often encountered especially in oil industries where oil and water are transported along pipelines (de Castro et al., 2012). The onset of entrainment or the flow pattern transition from ST to non-ST flow is believed to have occurred when the first droplet of either phases appear in the opposite one. When the flowrates are increased, interfacial waves start to develop in stratified flows which eventually become disturbed and break to generate droplet. Characterizing wave structures which develop at the interface is therefore important in understanding the flow transition from stratified to non-stratified patterns and reported studies conducted on wave characteristics in gas-liquid and liquid-liquid flows are discussed below.

2.1.2.1 Wave characteristics

Gas-liquid flows

A number of studies are available on wave characteristics in gas-liquid stratified wavy flows. Fan et al. (1993) investigated slug flow evolution from stratified-wavy flow using a conductance probe and visual observation. They found that waves either break or eventually become too large and touch the upper pipe wall filling the whole cross-section. Li et al. (1997) analysed interfacial wave characteristics such as the film thickness, wave height, wave propagation speed, wavelength and frequency using two-parallel conductance probes. They found that wave characteristics have strong influence on the pressure drop and heat transfer. Andritsos and Hanratty (1987ab) have also studied wave properties in horizontal gas-liquid flows and measured wave amplitudes and propagation speed with conductivity probes.

A large number of studies focused on interfacial wave characteristics in other flow patterns than in stratified and stratified-wavy flows, such as annular or slug flows. Many focused on wave structures of thin films and investigated film thicknesses and film characteristics (Webb, 1970; Chu 1973; Azzopardi 1997; Wang et al., 2004; Kadri et al., 2009). Hewitt and Hall-Taylor (1970) described wave properties in relation to entrainment in annular flows. Wang et al. (2004) studied the effect of interfacial waves and roughness due to the existence of waves on the friction factor under normal and microgravity condition in annular flows.

Liquid-liquid flows

Compared to gas-liquid flows there is still a lack of experimental data on the development of waves and their characteristics in liquid–liquid pipe flows, especially near the transition boundaries from stratified to non-stratified regimes. There are a number of studies available on interfacial waves in annular flows. Ooms (1972) and Ooms and Segal (1984) reported interfacial waves play an important role on the stability of core annular flow. Bai (1995) studied interfacial waves in vertical core annular flows and obtained oil volume fraction and interfacial wavelength. Based on this experimental data, Bannwart (2004) proposed a kinematic wave theory which used interfacial wave speed to indirectly predict volume fraction of the core in core annular flow. The results showed good agreement with the experimental data. Later, Rodriguez and Bannwart (2006) applied this theory to predict the oil volume fraction, and presented new experimental data on wave.

Only recently Al-Wahaibi and Angeli (2011) investigated the interfacial wave characteristics during the transition from stratified to non-stratified flows using a double-wire conductance probe. They reported that interfacial waves must be present for drops to appear and the characteristics of the waves are a function of the mixture velocity and the ratio of the velocities of the two phases. The results were later confirmed by Barral et al. (2015) who used conductance probes and high speed imaging to obtain interfacial wave characteristics. Castro et al. (2012) experimentally acquired wave characteristics such as wave amplitude, wavelength and wave velocity and related these characteristics to a modified Froude number. Castro and Rodriguez (2015) recently published new experimental data on interfacial wave characteristics and correlated them to Reynolds, Froude and Weber numbers (see Section 2.2 and 2.3). They found wave amplitudes increased with the Weber numbers and the wave velocities increased with the Froude number.

Overall, most of these studies on characterising interfacial waves, in both gas-liquid and liquid-liquid systems, focused on characterizing waves without commenting on the stability of waves. Some attempts have been made to relate such characteristics to flow parameters and physical fluids properties, but to date only a few studies are available on flow pattern transitions in relation to wave characteristics.

2.1.2.2 Flow pattern transition from ST to non-ST flows and stability of interfacial waves

The transition from stratified to non-stratified flows has been often described in terms of stability analysis of interfacial waves by applying the Kelvin-Helmholtz (KH) instability theory. KH analysis can be separated into two subcategories: Viscous KH (VKH) which includes shear stresses (Lin and Hanratty, 1986; Andritsos et al.,1989; Barnea, 1991; Barnea and Taitel, 1993) and inviscid KH (IKH) analysis where the shear stress terms are neglected (Taitel and Dukler, 1976; Mishima and Ishii, 1980).

In liquid-liquid flows, Brauner and Maron (1992a,b) first attempted to predict the transition from stratified to non-stratified flows using linear stability analysis. The analysis gave two transition lines: 1) zero neutral stability criterion (ZNS); and 2) zero real characteristic (ZRC) criterion. ZNS criterion represented the transition boundary from stratified to stratified-wavy flow, while the ZRC criterion was

used to predict the transition boundary from stratified-wavy into non-stratified flow. Using a limited amount of experimental data available, a reasonable agreement was found between experimental data and the model, although due to the shortage of experimental data the model was not fully validated. Trallero (1995) extended the works of Barnea and Taitel (1993) and performed VKH and IKH analysis taking into account the sheltering effect due to the trailing edge of the wavy interface for oil-water flows. The model showed excellent result when compared against their experimental results, but under-predicted experimental data by other investigators (Guzhov et al., 1973; Oglesby, 1979; Nädler and Mewes, 1995; and Cox, 1995). More recently Al-Wahaibi (2007) developed a correlation which based on force balance but gave similar results to KH stability analysis for long waves, and determined critical amplitude of a wave at which it becomes unstable in relation to the wavelength. He further experimentally obtained wave characteristics such as the wavelength and amplitude and developed a model to understand mechanism and predict onset of drop entrainment. The model assumes that drops will detach when the drag force acting on the wave is greater than the surface tension force then drops will form.

2.2 Flow around circular cylinder

In this section relevant studies conducted on a flow around a circular cylinder are discussed and presented. The current experiment entails several different engineering aspects to be considered, which include the effect of the pipe wall and the presence of both stationary and non-stationary interface on the flow behind the cylinder. Dimensionless numbers used to describe the flow characteristics in the flow system without the cylinder are also adapted to describe the flow behaviour behind the cylinder.

2.2.1 Definitions

Some dimensionless numbers important for describing the flow past a cylinder are introduced here. The cylinder based Reynolds number, Re is a fundamental dimensionless number in characterizing the flow around the cylinder. For a 2-D flow around a cylinder with diameter *D* fixed in position with a single fluid of uniform velocity, u, approaching it, the cylinder based Reynolds number can be defined as:

$$Re = \frac{\rho u D}{\mu} \qquad \text{Eq. (2.1)}$$

where μ is the fluid viscosity and ρ is the density of the fluid. In the current thesis the term Reynolds number will refer specifically to the cylinder based Reynolds number as given in equation 2.1, unless otherwise stated to minimize confusion between the pipe diameter based Reynolds number and the cylinder based Reynolds number.

As the fluid flows past a fixed cylinder, two force components, drag F_D and lift F_L contribute towards the total force F exerted on the cylinder which is defined as:

$$\vec{F} = \vec{F}_D\hat{x} + \vec{F}_L\hat{y} \qquad \text{Eq. (2.2)}$$

where $\hat{x}$ and $\hat{y}$ are the unit vector in the x and y-direction, respectively. Interpretation of each force term given in equation 2.2 is usually expressed in dimensionless terms of the lift, C_L and drag C_D coefficients. Given that the mean stream velocity is parallel to the x-axis, the drag coefficient can be given as:

$$C_D(t) = \frac{F_D(t)\cdot\hat{x}}{\frac{1}{2}\rho u^2 D} \qquad \text{Eq. (2.3)}$$

and the lift coefficient is given as:

$$C_L(t) = \frac{F_L(t)\cdot\hat{y}}{\frac{1}{2}\rho u^2 D} \qquad \text{Eq. (2.4)}$$

For unsteady flows (i.e Re > 47) the lift is periodic as vortex shedding starts to occur in the wake of the cylinder, and because of the periodic nature of the oscillation the time-mean value is often assumed to be zero. The periodic oscillation, f, is defined as:

$$C_L(t+f) = C_L(t) \qquad \text{Eq. (2.5)}$$

This periodic oscillation is often characterized in terms of the Strouhal number, St which is the ratio of the period of oscillation to a characteristic advective time scale *u/D* and it defined as:

$$St = \frac{f}{u/D} = \frac{fD}{u} = \frac{uD^2}{\mu}\frac{f}{Re} \qquad \text{Eq. (2.6)}$$

2.2.2 Mechanism of vortex shedding behind a cylinder

For flows beyond Re > 47, small disturbances on the incoming flow can trigger vortex shedding downstream the cylinder. A description of the vortex shedding mechanism has been first given by Gerrard (1966) and later by Perry et al. (1982) focused on experimental studies using time-exposure photography. Once a system reaches a steady-state, there will be alternating vortices which detach from the two opposite sides of the cylinder as shown in Figure 2.6. At an instance, there will be a vortex which is bigger and stronger in magnitude (vortex A in this case in Figure 2.6a) and this vortex is strong enough to withdraw the fluid from outside the cylinder wake (marked with B in Figure 2.6a). As the fluid is pulled towards the cylinder it begins to form another vortex but with vorticity of opposite sign to that of vortex A. Once the distance between the two vortices are close enough, vortex B will cut off the further supply of vorticity to vortex A, and as vortex A can no longer sustain itself, it is driven away by the bulk flow (shown in Figure 2.6b). Vortex B now will pull the fluid from the opposite side of the cylinder (marked with C in Figure 2.6b) and this process repeats. This mechanism however has a limitation that there must be an interaction between the two opposite vortices which are similar in magnitude. There will be no shedding or very weak and non-oscillatory shedding will form if the vortex

of one side is pre-dominant - for example when the cylinder is too close to the wall or there are obstacles which block the interaction such as a split plate (Kwon and Choi, 1996).

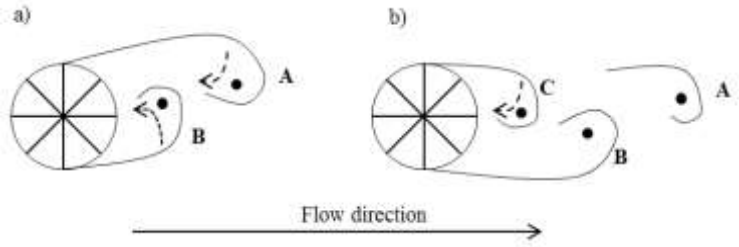

Figure 2.6 Schematic drawing of vortex shedding mechanism described by Gerrard (1966). a) Vortex B being pulled in across the wake before vortex B. b) Vortex A eventually shed off with the bulk flow and vortex C being pulled in across the wake before vortex B (similar to Figure 2.6a).

2.2.3 Isolated cylinder – Flow regimes

For flows around an isolated cylinder, there are currently 15 regimes under 5 differently named wake states classified by Zdravkovich (1997) which are widely used. Visual observation of the flow behind the cylinder started as early as 1936 by Homann (1936) where an oil slick was used as tracer to show vortex street forming behind the cylinder at different Reynolds numbers. Lamilar or turbulent flow conditions were not treated as flow regimes for the flow patterns. The patterns observed at different Reynolds numbers were first categorized by Roshko (1954) based on measurements of velocity fluctuations and frequency obtained behind the cylinder. He found 3 different regimes, namely 'stable' regime with laminar vortex shedding for Re = 40 – 150, a 'transition' regime for Re = 150 – 300 and 'irregular' regime for Re = 300 – 10,000+. Later Bloor (1964) used a hot-wire anemometer and found the ranges at which the three regimes occur are similar to those of Roshko (1954). Since the work of Roshko, there have been many studies on vortex shedding behind a bluff body. There is a number of extensive reviews on the topic which have been made in the past years (Berger and Wille, 1972; Lin and Pao, 1979; Bearman, 1984; Oertel, 1990; Griffin and Hall, 1991; Coutanceau and Defaye, 1991; Williamson, 1996). Based on the available experimental and numerical studies, Zdravkovich (1997) compiled most of all available work conducted on the flow past a cylinder and systematically classified the patterns as given in Table 2.2.

Table 2.2 Cylinder flow regimes collated by Zdravkovich (1997) at different Re

State		Regime	Re
Laminar	L1	No separation	0 to 4 -5
	L2	Closed wake	4 -5 to 30-48
	L3	Periodic wake	30 - 48 to 180 - 200
Transition in wake	TrW1	Far wake	180 - 200 to 220 - 250
	TrW2	Near wake	220 - 250 to 350 - 400
Transition in shear layers	TrSL1	Lower	250 - 400 to 1k - 2k
	TrSL2	Intermediate	1k - 2k to 20k - 40k
	TrSL3	Upper	20k - 40k to 100k - 200k
Transition in boundary layers	TrBL0	Pre-critical	100k - 200k to 300k - 340k
	TrBL1	Single bubble	300k - 340k to 380k - 400k
	TrBL2	Two bubble	380k - 400k to 500k - 1M
	TrBL3	Supercritical	500k - 1M to 3.5M - 6M
	TrBL4	Post-critical	3.5M - (unknown)
Fully turbulent	T1	Invariable	(unknown) to inf (∞)
	T2	Ultimate	

Laminar L1 - No separation regime

This regime is often referred to as the creeping flow regime. It occurs at Re < 5 where the flow is highly viscous and the flow is laminar. At this condition the lift force is 0 as the flow is symmetric (Henderson, 1995).

Laminar L2 - Closed wake regime

This regime is also referred as laminar steady regime (Williamson, 1996). In this regime a pair of fixed recirculation regions forms at the rear of the cylinder. This happens as the viscous drag force is reduced, thus the boundary layer separates from the bluff body to form a parallel shear layer in the wake. Inside the recirculation region, opposite signed eddies are formed which grow with Re. From numerical calculations it has been found that this region could stay stable up to Re = 46 (Williamson, 1995).

Laminar L3 - Periodic wake

A periodic oscillation of vortex shedding is first observed in this regime beyond Re = 46, where the recirculation region develops instabilities and grows strength and amplification with increasing Re as shown in Figure 2.7 b-f. In this regime, the flow and all regions of the wake remain laminar up to Re = 188 (Barkely and Henderson, 1996). The Re at which this transition from stable to unstable flow occurs (Williamson 1995) was only recently found although its existence was known as early as 1927 (Camichel et al., 1927). The oscillating vortex shedding induces a lift force, given by equation 2.5, with a frequency can be denoted in terms of St number (equation 2.6). It would be expected that as the flow

is laminar, the results of St number measurements in both two- and three-dimensions would be similar. However, Tritton (1959) found from experimental work multiple St numbers coexisting for the same Re numbers (Figure 2.8). In the early days, it was suggested (Tritton, 1959; Gaster 1971) that the existence of multiple St numbers could be due to the cylinder vibrations until Williamson (1988) found that the cylinder end effects were responsible for this phenomena. Until Re = 64, parallel vortex shedding occurs (See Figure 2.8a) and St numbers can vary along the spanwise direction of the cylinder (f_U and f_L). Beyond Re > 64 up to 190, a 'chevron' shaped of vortex is produced, namely oblique vortex shedding, which is at a certain angle parallel to the cylinder (Figure 2.8b). Later, several authors confirmed the cylinder ends are responsible for the two different St numbers for flows with between 47 and 64 (Mitta, 1991; Norberg, 1994; Henderson, 1997).

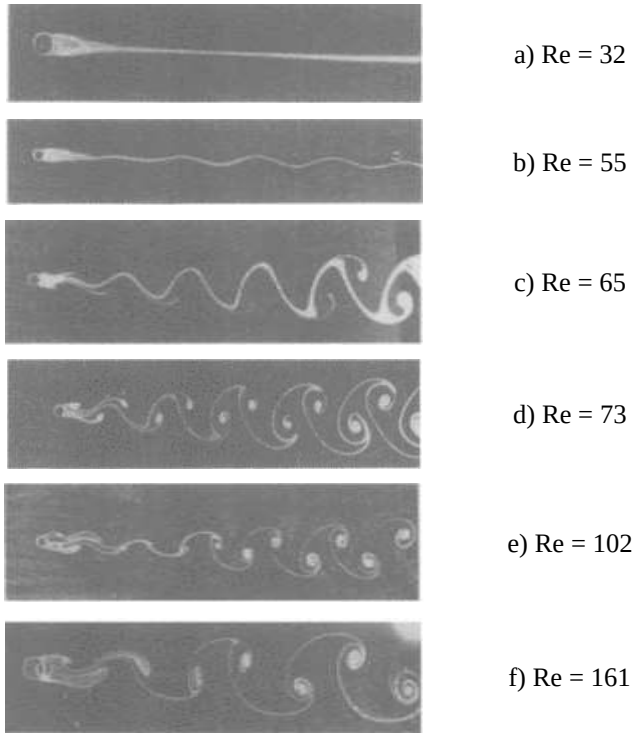

Figure 2.7 Vortex shedding behind a circular cylinder in a stream of oil (Homaan, 1936)

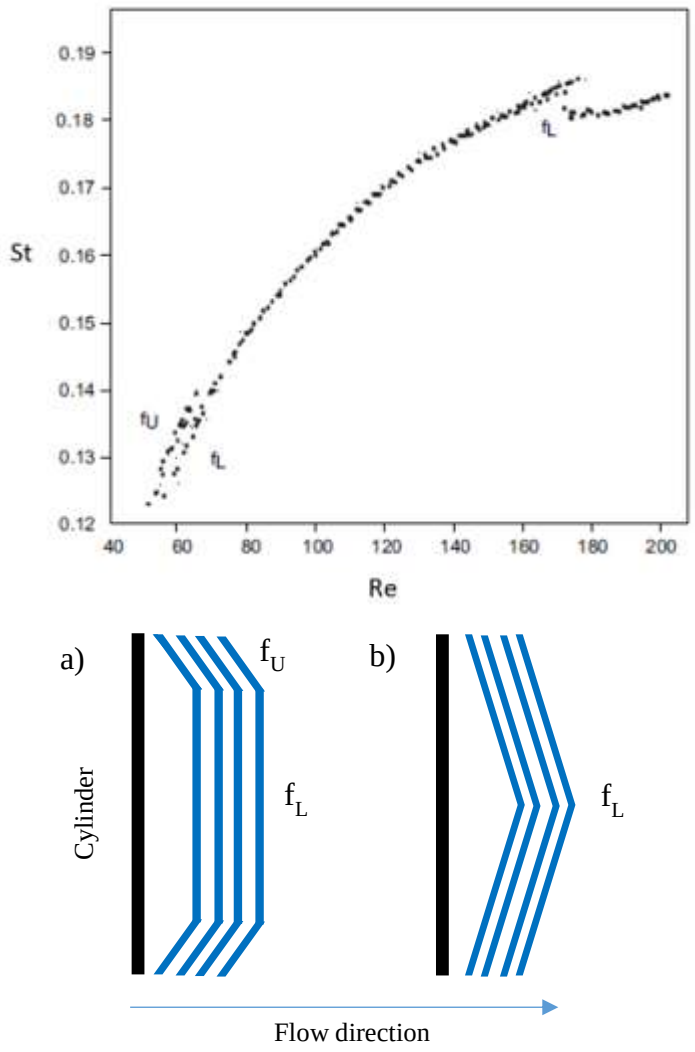

Figure 2.8 a) St -Re plot (reproduced from Willamson, 1995). b) Parallel shedding mode, for Re <64 (left) and oblique shedding mode, for Re = 64~188 (right)

Transition in wake - Far wake

Beyond Re > 190 there is a transition of vortex shedding from two-dimensional to three-dimensional (Roshko, 1954; Williamson, 1998) and this process involves two discontinuous changes. At an early stage of vortex shedding transition, typically between 190 < Re < 260, there is a drop in the St number from the laminar curve (which refers to oblique or parallel shedding, see Figure 2.8). Williamson (1996) suggested that this is due to an inception of streamwise vortex loops, typically with a wavelength between 3 – 4 cylinder diameters which distort the primary vortex shedding rollers, and named this type of vortex shedding as mode A. Increasing the Reynolds numbers beyond 260, the typical wavelength of the streamwise vortex loops is reduced close to the size of the cylinder diameter known as mode B. At the transition from mode A to B occurs there is another discontinuity in the St numbers on the St-Re graph. The wake characteristics of mode B can persist up to Re = 10,000 (Williamson, 1996).

Transition in shear layer and other flows regimes beyond

Between $350 < Re < 2 \times 10^5$, the Strouhal number gradually decreases and the formation length of the recirculation region decreases. These trends are caused by the developing instability of the separating shear layers from the sides of the body. However, the boundary layer over the cylinder still remains near the bluff body during transition in shear layer regime. Beyond $Re > 3 \times 10^5$, transition takes place within boundary layer itself. Between the range $3 \times 10^5 < Re < 3.5 \times 10^5$ the boundary layer becomes turbulent but only on one side (either side) of the body and the Re where this phenomenon occurs is called the critical flow regime (Williamson, 1996) or single bubble regime in transition in boundary layers (Zdravkovich, 1997; see Table 2.2).

Further increase in Re leads to boundary separation on both sides of the cylinder (two-bubble regime; Zdravkovich, 1997) although some parts of the boundary layer still remain attached to the cylinder and the transition is not complete. This is for Re up to 1×10^6. When Re reaches 1.5×10^6 and beyond (supercritical region), then one side of the bluff body is fully turbulent but the other side still remains partially laminar. Finally when $Re > 4.5 \times 10^6$ then the boundary layer over the entire region is turned into turbulent. However, there is no discrete values of Re on determining different flow regimes.

2.2.4 Cylinder with nominally Stationary boundary

In this section relevant studies conducted on the flow around a circular cylinder placed close to a solid wall and deformable (free surface) is discussed.

2.2.4.1 Effect of solid wall

Single wall

A number of experimental and numerical works on the flow around a circular cylinder near a plane solid wall have been conducted. To date these revealed that when a cylinder is positioned close to a solid wall (boundary), i.e at low gap ratios, γ which can be defined as $\gamma = H/D$ where H is the distance between the cylinder and the wall, the flow characteristics in the wake of the cylinder are different from those of an isolated cylinder. Previous studies (see Table 2.3) have shown that the major effect of the wall can be classified into three categories; 1) above $\gamma > 1$, the flow is essentially the same as that of an isolated cylinder; 2) forces (lift and drag) on the cylinder and the shedding frequency (Strouhal number) are slightly modified as the cylinder is positioned closer to the wall ($0.3 \sim 0.5 < \gamma < 1$); 3) essentially vortex shedding is fully suppressed for flows with gap ratios below $\gamma_{crit} < 0.3 \sim 0.4$.

Most studies focused primarily in determining the critical gap ratio at which the shedding is fully suppressed. Three factors seem to affect this, namely the Reynolds numbers, the boundary layer thickness, δ, and the distance between the cylinder and the wall. It is generally accepted that the thickness of the boundary layer has negligible impact on shedding frequency once the vortex shedding takes place but influences the critical gap ratio. Grass et al. (1984) found different values of the critical gap ratio at different boundary layer thicknesses, where the boundary layer thickness to the cylinder diameter ratio δ/D was below 2.5, the γ_{crit} was found to be 0.3 and at $\delta/D >> 3.5$, γ_{crit} was about 0.5.

Taniguchi and Miyakoshi (1990) experimentally found $\gamma_{crit} = 0.3$ for $\delta/D = 0.4$ and $\gamma_{crit} = 0.1$ for $\delta/D = 1$, and a similar trend was also observed by Lei et al (1999) where they also observed the critical gap ratio was dependent on the thickness of the turbulent boundary layer. In addition, Grass et al. (1984) and Taniguchi and Miyakoshi (1990) have suggested the vortex shedding suppression is associated with the cancellation between the negative wall-boundary layer and the positive shear layer from the cylinder.

The studies of the effect of proximity of the cylinder to a solid wall at various flow conditions is done usually via indirect methods in practice, such as obtaining the signals of forces acting on the cylinder or the velocity fluctuations from hot-wire signals, to calculate corresponding frequencies and the St numbers. However, most of the previous experimental studies were conducted at moderately high Reynolds numbers typically in a turbulent regime with $Re > 10^3 \sim 10^5$. These studies generally show that the effect of Reynolds number on the suppression of vortex shedding and the vortex shedding frequency is not so significant but rather strongly depend on the gap ratio. The studies including Bearman and Zdravkovich (1978), Grass et al. (1984) and Taniguchi and Miyakoshi (1990) found the vortex shedding frequency in the wake of the cylinder increased with Re but the Strouhal number remained constant at 0.2, which is the same value as that of the unbounded case with no wall effects for 3-dimensional flows. On the other hand, Grass et al (1984) found an increase in the frequency at constant Re with maximum difference of 10% at $\gamma = 0.5$.

Parallel walls

For a cylinder placed between two solid boundaries the blockage ratio, defined as the ratio between the cylinder diameter D_{cyl} and the distance between the two walls, L, can affect the flow. The effective narrowing of the flow passage can cause the fluids to accelerate and increase the force on the cylinder. Chen et al. (1995) claimed for the case of a centrally positioned cylinder between two parallel walls, that no significant changes in the hydrodynamic patterns behind the cylinder were observed for blockage ratios below 0.5. Zdravkovich (2003) found the flow can be very sensitive for flows in the laminar regime ($Re < 180$) and $D/L > 0.001$ whereas for 3-dimensional flows and $D/L < 0.1$, the blockage effect can be ignored. Zovatto and Pedrizzetti (2001) studied numerically the flow around a cylinder positioned centrally between two parallel walls for $100 < Re < 2000$ and $L/D = 0.2$ with varying gap ratios between 0.25. They found the transition from steady to unsteady flow was delayed as the cylinder approached a wall but the effect of confinement due to the secondary wall had little impact. Similarly for unsteady flows, the patterns were similar to those of unbounded flows, except that the vertical position of the negative and positive vortices were reversed where the positive vortices were found closer to the top wall and the negative vortices nearer the bottom wall. Zovatto and Pedrizzetti (2001) claimed these phenomena are primarily due to three reasons; 1) non-uniform velocity profile in upstream of the cylinder leads to development of asymmetric shear around the cylinder; for example, at very low St numbers the average lift force acting on the cylinder is non-zero; 2) the presence of the wall which acts an irrotational constraint, and in return limits further development of vortices generated in the wake of the cylinder hence resulting to a different vortex formation mechanism; 3) formation of wake-induced boundary layer on the wall.

Table 2.3 Summary of studies on the effect of gap ratio on the flow around a cylinder close to a wall

Author	Study type	Measurement / Simulation Technique [a]	Re	γ
Bearman and Zdravkovich (1978)	Experimental	HWA, Pressure	2.5 - 4.5 x 10^4	0 – 2.5
Grass et al. (1984)	Experimental	FV, HWA	1785, 3570	0 – 2.0
Taniguchi and Miyakoshi (1990)	Experimental	FV, HWA, Pressure, Force	9.4 x 10^4	0.1 – 3.0
Buresti and Lanciotti (1992)	Experimental	Force	0.86 – 2.76 x 10^5	0 – 1.5
Lei et al. (1999)	Experimental	Pressure	1.3 – 1.45 x 10^4	0 – 3.0
Lei et al. (2000)	Simulation	Finite Difference Method (2D)	80 – 1000	0.1 – 3.0
Zovatto and Pedrizzetti (2001)	Simulation	Finite Element Method (2D)	100 – 2000	0.25 – 2.0
Price et al. (2002)	Experimental	FV, HFA, PIV	1.2 – 4.96 x 10^3	0 – 2.0
Dipankar and Sengupta (2005)	Simulation	Stream-function / vorticity formulation (2D)	1200	0.5, 1.5
Wang and Tan (2008)	Experimental	PIV	1.2 x 10^4	0.1 – 1.0

[a] FV- Flow Visualization; HWA – Hot-Wire Anemometry; PIV – Particle Image Velocimetry

2.2.4.2 Effect of free surface

A few studies have investigated the interactions between a free surface and vortices shed by bluff bodies of different shapes. These flows are characterised by the Froude number ($Fr = u/\sqrt{gD}$, where g is the gravitational force and D is the cylinder diameter) and the depth of submergence of the bluff body h* (h* = h/D, where h is the distance between the top of the cylinder and the interface/free surface). Hydrofoils are commonly used in these studies because of their relevance to marine applications. Duncan (1981) used a hydrofoil towed inside a deep water channel to generate breaking waves. Hydraulic jump was observed just downstream the bluff body while the wavelength and the crest-to-trough amplitude were proportional to the hydrofoil speed squared. Lin and Rockwell (1995) studied the free surface shape and breaking waves downstream a hydrofoil and obtained velocity profiles using PIV. They observed a sharp elevation of the interface just downstream the bluff body, or so called a hydraulic jump, which increased with increasing Froude number. Square shaped bluff bodies have also been studied as they are relevant to architectural and engineering applications in the design of buildings and bridges. Malavaski and Guadagnini (2003, 2007) observed free surface distortion when a square cylinder was submerged in a water channel at various distances above the channel wall. They also

suggested proximity of the bluff body to the free surface was responsible for the change in drag and lift coefficients that depended on the Reynolds number.

A limited number of studies have been carried out using cylinders as bluff bodies because of their simplicity. Miyata et al. (1990) conducted both experimental and numerical investigations using a cylinder near a free water surface. Only one flow condition was investigated at various depths of submergence and no surface distortion was observed. However, different wake states were apparent from visual observations made using tracer particles illuminated and then captured with long exposure time (0.5 second). The wake states were interpreted in terms of the corresponding drag and lift forces measured using a cylinder attached to a load cell. Similar wake states were later observed by Sheridan et al. (1997) who used PIV to study the vortices generated downstream a cylinder in a deep water channel located at various distances from the free water surface. The wake states were largely dependent on the Froude number and the depth of submergence. Free surface distortions or waves were also observed and at extreme combinations of Fr and h* (h* = 0.59 and Fr = 0.78, h* = 0.40 and Fr = 0.60), breaking waves were observed. Later Reichl et al. (2005) found their numerical simulation results were in good agreement with the experimental results from Sheridan. Daichin and Lee (2004) investigated experimentally with PIV flows around elliptical bluff bodies and found three typical flow patterns, Coanda flow, where the flow remains attached to the surface of the curved surface around the upper part of the cylinder, a jet-like flow, and attachment of the jet onto the free surface. The authors all studied on the flow structures and flow fields immediately downstream the cylinder, while the investigations on the characteristics of interfacial waves generated downstream the cylinder were not conducted. Tanase et al. (2014) recently carried out both experimental and numerical investigation on the flow around an immersed cylinder near a free surface, in a 2-D water tank. Through high speed imaging and CFD analysis using FLUENT, the shape of the free-surface were produced. Hydraulic jump immediately downstream the cylinder was observed and showed good agreement with the result from the simulations, although the shape of the free surface layer further downstream showed deviation between the experimental and numerical results. However, the authors did not give any physical explanations on the observed phenomena.

2.2.5 Cylinder with non-stationary boundary

In liquid-liquid pipe flows, the interface between the two phases can fluctuate. Depending on the flow conditions, sometimes large interfacial waves may form at a junction where the two fluids meet due to KH-instability (Barral et al., 2015). In such cases, the vertical position of the interface relative to the cylinder position h* will vary in time. In the current work the cylinder is positioned close to the inlet and the interaction between the waves generated initially at the inlet with the cylinder is unavoidable in some flow conditions. Relevant studies conducted on this topic are discussed below. Currently available literature on the wave and structure (with relevance to the current thesis, only cylinder is considered) interaction can be split into two categories: 1) flow around an oscillating cylinder / cylinder in oscillatory flow; 2) flow around a cylinder in orbital motion / cylinder in orbital flow. In these studies, the Keulegan-Carpenter number, KC ($KC = Uf_o/D_{cyl} = 2A\pi/D_{cyl}$, where U and A are wave amplitude

and f_o is the frequency of oscillation), is commonly used as control variable to represent the wave motion.

2.2.5.1 Oscillatory flow / oscillating cylinder

In oscillatory flows, usually the flow is unidirectional in the flow direction and a cylinder is trailed along following the trajectory of a wave represented by the KC number with a given frequency and amplitude. There are several studies conducted on oscillatory flow past a cylinder (Singh, 1979; Bearman et al., 1981; Sarpkaya and Isaacson, 1981; Williamson, 1985, Tatsuno and Bearman, 1990). These authors provided insight into the flow structures and vortex patterns around the cylinder at various ranges of KC. Several authors attempted to further analyse these vortex structures relating to the forces acting on the cylinder. Applying the relationship between vortices and loading on a cylinder first proposed by Sarpkaya (1968, 1969), Maull and Milliner (1978) visually observed the movement of vortices generated in the wake of a cylinder and qualitatively related these to the forces acting on the cylinder. Using a similar approach, Lin and Rockwell (1996) approximated the lift acting on the cylinder at each point of vortex of given circulation though quantitative image analysis. Further analysis on the physics of vortex formation and different instantaneous vorticity patterns were captured via high-image-density particle image velocimetry by Lin and Rockwell (1999). They found the depth of submergence in the generation of vortex in the wake of a cylinder plays a key role.

2.2.5.2 Orbital flow

Rotational flows are similar to oscillatory flows except an additional velocity component, usually vertical component, is added to the system. Similarly, majority of studies conducted in orbital flows primarily focused on measuring forces on the cylinder and studying the wake state (Chaplin, 1981; Sarpkaya, 1984; Grass et al., 1984; Williamson et al., 1998; Oshkai and Rockwell, 1999; Carberry et al.,2004). From the experimental work with high-image-density particle image velocimetry, Oshkai and Rockwell (1999) concluded that irrespective of the particular pattern, which is very much dependent on space and time, the central elements of the vortex formation process appeared to persist. They found a general evolution of the vorticity followed a particular pattern in sequence: i) growth of pronounced region of vorticity on the cylinder surface ii) migration of this vorticity in the same direction of the orbital motion of the wave iii) separation of the vorticity from the cylinder surface.

2.3 Droplet detachment and ligament breaking

The mechanism of entrainment in liquid-liquid flows is not yet fully understood although it is generally accepted that, at least during the transition from stratified to non-stratified flows, the entrainment process involve non-stables interfacial waves and further development of such waves leads to formation of ligaments and wave breakage (Al-Wahaibi and Angeli, 2011). From recent works on numerical simulations conducted on linear and non-linear instability of two-phase liquid-liquid flows (Valluri et al., 2008, 2010; Naraigh et al., 2014), it can be found that various mechanism in predicting the drop formation from interfacial waves and ligament breaking comes from earlier studies of gas-liquid flows

(Marmottant and Villermaux, 2004). In this section relevant studies conducted on ligament formation and breaking in both gas-liquid and liquid-liquid systems are discussed and presented.

2.3.1 Definition

Fluid thread or fluid ligament breakup is the process by which a single mass of fluid breaks into a several smaller fluid masses (Figure 2.9). The process is characterized by the elongation of the fluid mass forming thin, thread-like regions where the thread-like regions continue to thin until they break, forming individual droplets of fluid. This process of first or primary drop formation from a ligament is called primary break up. However, the outcome of the thread breakup process is dependent on the surface tension, viscosity, density, and characteristic diameter of the thread undergoing breakup. Some of these parameters can be represented in terms of dimensionless numbers which are the Reynolds number, the Weber number, and the Ohnesorge number.

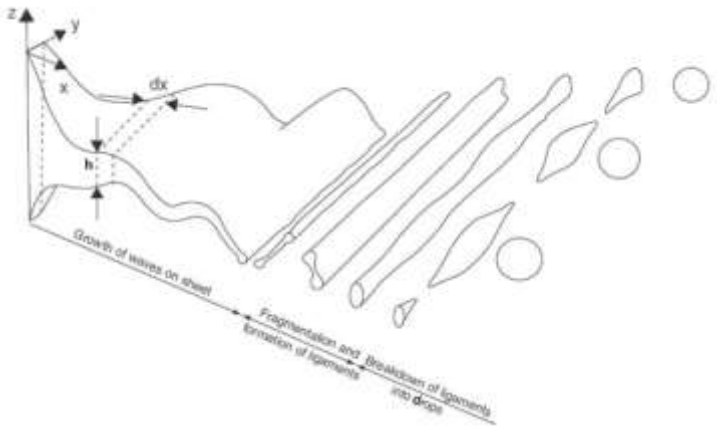

Figure 2.9 Schematic drawing showing different stages of wave instability of a thinning liquid sheet (Zandian et al., 2016)

Weber number

The Weber number, We, is an important parameter comparing the ratio between inertia and surface tension effects especially within a thread or tube. When the Weber number is large, the inertia of the thread is large which resists the tendency of surface tension to flatten curved surfaces. For small Weber numbers surface tension dominates the thread behaviour, e.g it suppresses the formation of wavy interface and breakage from capillary instability. Considering a jet-spray system in stagnant-air where a liquid is pushed through a thin tube, the Weber number can be defined as $We = \rho_l U_l^2 D_l/\sigma$, where U_l, D_l, ρ_l, and σ are liquid bulk velocity, diameter of the liquid-jet nozzle, density of the liquid and liquid surface tension, respectively. Usually the nozzle diameter is considered although there are studies where they used the nozzle radius, r, instead of the diameter, $r = D_l/2$. However, previous studies showed the diameter of ligaments which are 'stripped' from the liquid core can largely vary and much smaller than the nozzle size, hence applying the nozzle diameter to compute the Weber number under certain conditions, especially directly applying to the current work can affect the results.

Ohnesorge number

The Ohnesorge number, Oh, is the ratio between viscous and surface tension forces on the thread. Small Ohnesorge number implies that the effect of liquid viscosity on thread breakup is small. For instance, a larger disturbance (large We number) is required as Oh is increased as viscous force tends to inhibit drop formation (Hsiang and Faeth, 1992, Faeth, 1996; Sallam et al., 2002). For a gas-assisted system, Ohnesorge number for the liquid phase is defined as $\mathrm{Oh} = \frac{\mu_l}{(\rho_l \sigma D_l)^{0.5}}$.

2.3.2 Mechanism of ligament formation and breakup

For the process of droplet detachment from a liquid core or a sheet, there are mainly 3 instabilities that are considered which appear to be most relevant to the current study of ligament generation and breaking in liquid-liquid flow system past a bluff body. The three instabilities considered here are Kelvin-Helmholtz instability, Capillary instability and Rayleigh-Taylor instability.

2.3.2.1 Ligament formation

From previous studies it is evident that ligaments lead to drop formation, and ligaments are generated from the destabilization of the interface due the fast flowing gas phase and slow flowing liquid phase. Discontinuity in the velocity at an interface between two phases and its role in the destabilization first gained attention by Helmholtz (1868) while later detailed analysis was performed by Kelvin (1871). Later, Fraser et al (1962) suggested that atomization of a liquid sheet subject to a KH instability goes through a production of transverse ligaments which eventually disintegrate to give off droplets. Lozano et al (1996) suggested a liquid sheet surrounded by a high-velocity gas may disintegrate under cellular regime, where ligaments that are nominally oriented along in the spanwise direction of the liquid sheet. There are many more studies where they observed ligament formation before observing the appearance of droplets (Clanet and Villermaux, 2002; Marmottant and Villermaux, 2004; Wang et al., 2008). Schematic drawings showing the development of the liquid jet breakup process is given in the works of Varga et al. (2003), as shown in figure 2.10 below.

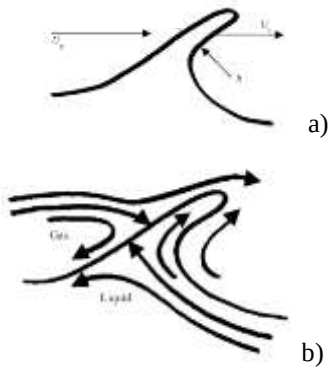

Figure 2.10 Schematic diagram given by Varga et al. (2003). a) Schematic drawing of the liquid jet breakup process and b) streamlines in the ligament process

In Figure 2.10a, initially, waves of length λ_1 are formed at the gas–liquid interface by the primary shear instability. Due the high-speed gas on this wave structure the waves are drawn out into ligaments with

a characteristic thickness, noted as b. In figure 2.10b, the streamlines of the both the gas and the liquids around the ligament are shown. Due to a high acceleration caused by the high speed gas phase, the thickness (or the diameter) of the ligament decreases and this process leads to unbalance in the stagnation point between the gas and the liquid flows as shown in Figure 2.10b. Eventually the ligament loses the support from the liquid core and becomes more vulnerable to the fast flowing gas stream, which could go under further undulation via Rayleigh-Taylor (RT) instability, which is known as an instability which occurs at an interface between two fluids with different densities where the lighter phases pushes the heavier phase, and form corrugations of a characteristic wavelength λ_{RT}. It should be noted that some of these instabilities can happen on different length scales. For example, the RT instability explained in the study of Varga et al (2003) is observed on the ligaments generated on the surface of a liquid core via KH instability, although sometimes this type of RT instability can be observed on a slightly larger scale where the entire liquid jet is destabilized and a mushroom-like tip head is formed (Figure 2.11). Typically this occurs in a stagnant-air system.

The physical explanation of ligament formation in a stagnant-gas system is very similar to that of the gas-assisted system. The numerical study of Shinjo and Umemura (2010) showed that the liquid jet injected into stagnant air rolled up and formed a mushroom shaped tip (Figure 2.11). They observed that ligament formation first occurs at the tip edge, where the shear is greatest due to axisymmetric vortices generated behind the mushroom tip. It was suggested that ligament creation is strongly correlated with the local velocity field. The presence of axisymmetric vortices was evident by the circular low pressure in the region behind the tip. They also found that the direction of ligament is dependent upon the local structure of the vortices generated. In addition, the generated droplets and ligaments sometimes re-coalesced with the liquid core, feeding further disturbance to the surface. Once the ligaments are formed, they are either further elongated and lead to drop detachment from the tip or they could recontract and not produce any drops.

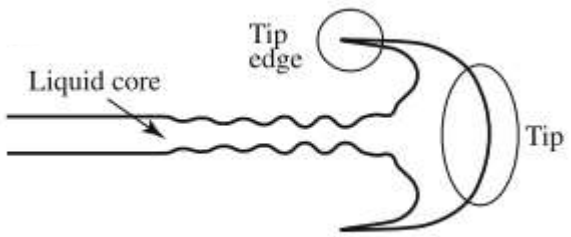

Figure 2.11 Schematic drawing of a jet going under RT instability (Shinjo and Umemura, 2010)

2.3.2.2 Ligament breakage

It is known that the ligament or thread-like breakup occurs due to the capillary instability. There has been many studies in this field and a summary of previous studies on the capillary effect is given by Pomeau and Villermaux (2006). Previous experimental and numerical studies (Umemura and Wakashima, 2002; Umemura, 2007; Shinjo et al., 2009) showed that the key role is played by

propagative capillary waves. They found that two wave modes of pinch-off exists, i.e the short-wave mode and the long-wave (Rayleigh) mode. Similar wave modes appeared in the works of Shinjo and Umemura (2010). They observed that short-wave modes, also termed as 'end-pinching' mode in some other works (Stone, 1994; Wang et al., 2008), mainly appear at the jet tip and the wavelength observed for this particular wave mode was comparable to a steady propagation wave which has a typical wavelength of $3.62a_L$ where a_L is the ligament radius. This wave mode can naturally destabilize and pinch-off occurs, and this mode does not require a n role of a injection nozzle. On the other hand, long-wave mode is driven by short capillary waves reflected off the jet tip where the wavelengths of the reflected waves are longer due to Doppler shift. When the ligament length is large this mode may appear. Such wave modes will depend on the We and Oh numbers, although for an actual ligament in the spray, the short-wave mode is dominant as ligaments will be attached to the liquid bulk not to the nozzle (Shinjo and Umemura, 2010)

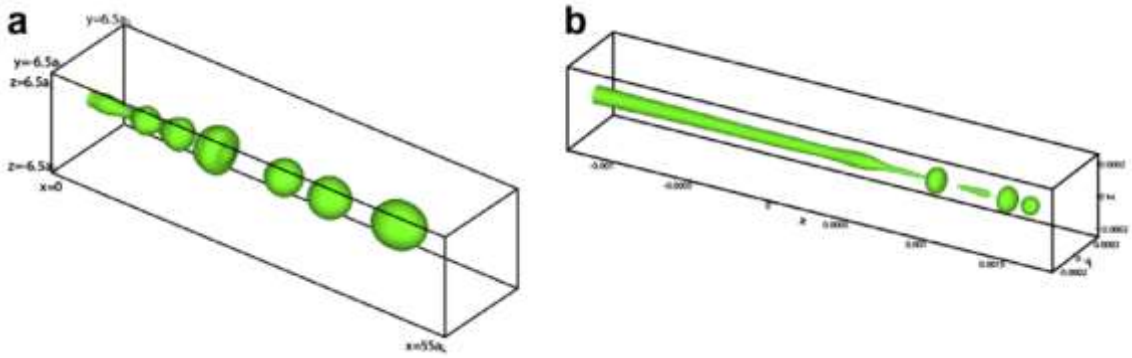

Figure 2.12 Droplet formation on a slow liquid jet. a) short-wave mode with the pinch-off wavelength ~$3.6a_L$; b) the long-wave (Rayleigh) mode with the pinch-off wavelength ~9aL (Shinjo and Umemura, 2010)

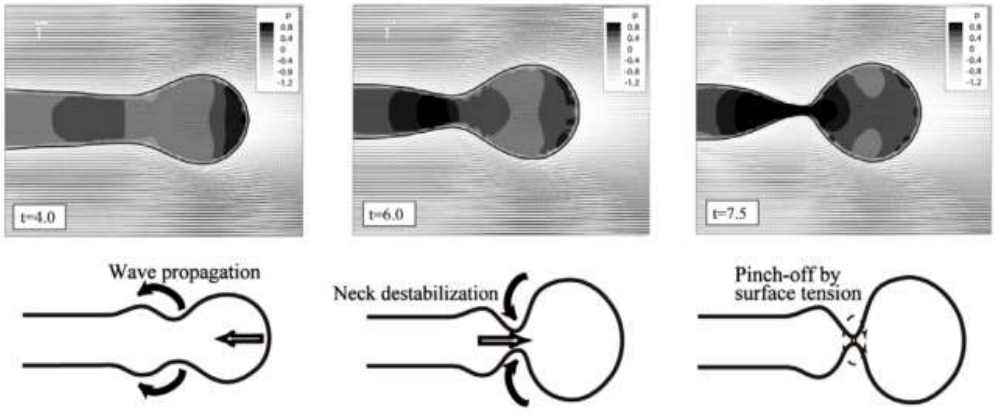

Figure 2.13 Computed pressure and velocity field of a step-by-step stage of short-wave mode destabilization (Shinjo and Umemura, 2010)

Figure 2.12a and b shows the short-wave mode and long-wave mode, respectively, for a case with relatively high Ohnesorge number (We = 1.4, Oh = 0.076). The short-wave mode evolution is slow and

pinch- off occurs sequentially from the tip. The representative stages in the short-wave mode are illustrated in Figure 2.13 that corresponds to Figure 2.12a case.

Due to surface tension the liquid jet tip contracts and this pushes the inner part along the injection axis (Figure 2.13 at t = 4), resulting high pressure in the tip bulb. This motion produces compression waves and the first neck (counted from the jet tip) to form. Along with this, the tip bulb grows as more liquid is pushed into to tip bulb caused by contraction of the neck. As the tip bulb size grows, its inner pressure falls and more liquid enters the tip from the neck, and the neck becomes thinner. Finally, when the neck is thin enough, the circumferential surface tension cuts the neck. The study showed that this short-wave mode pinch-off mechanism also applies to ligament breaking in high-speed sprays. Overall, based on the previous studies the fundamental mechanism of ligament formation appears to be similar to that of ligaments formed in the current system, i.e ligaments are formed due to shear. However, for liquid-liquid systems, it appears some modification in the dimensionless numbers considering interfacial tension and velocities of both phases would be necessary.

2.4 Concluding remarks

The literature reviewed in this Chapter revealed that the study on the liquid-liquid flows past a cylinder requires understanding of knowledge from different fields of studies. Previous literatures conducted on liquid-liquid flows show that mechanism of the flow pattern transition from stratified to non-stratified flows are yet to be fully understood. There have been advancements in technologies to help identify flow patterns and study the transitions, a systematic approach to study the flow pattern transitions is still difficult. Following the traditional approach to study the flow pattern transition seemed to have limitations and there is a gap to investigate the flow pattern transition in a new approach. The aid of a cylinder is used in the current study to make the experiment more systematic. However, it requires further understanding of flows around a circular in a pipe-geometry which are essentially different from the classical flows around a cylinder and requires further investigation as not much is known yet. There are several important parameters, namely the Froude number, gap ratio and the depth of submergence, which must be carefully considered in designing the experiment and during the analysis of the results. Information on the flow around a cylinder in a confined pipe geometry in literature is still very limited. In addition, flow around a cylinder with the presence of a liquid-liquid interface requires further study. There is evidence that breaking waves in both gas-liquid and liquid-liquid systems are closely related to the formation of ligaments. The current study aims to integrate the knowledge from different fields of studies mentioned in the literature and provide more insight and data on flow pattern transitions from stratified to non-stratified flows.

CHAPTER 3. EXPERIMENTAL METHODS

This chapter provides details on the experimental facilities, instrumentation and data treatment methods used. In section 3.1 two experimental flow facilities are described in detail. The design of the bluff body considering various physical parameters is discussed in section 3.2. Measurement techniques, data treatment procedures and analysis are given in the following two sections, section 3.3 and 3.4. Error analysis is discussed in the final section of this Chapter in section 3.5.

3.1 Experimental Flow Facility

A total of two experimental flow facilities were used in the study which are located in the Multiphase Flow Laboratory, Department of Chemical Engineering, UCL. The first flow facility (large-scale) has test fluids with different refractive indices (details given in section 3.2.1) and mainly volume-illuminated high speed imaging, high speed PIV and conductivity measurements were conducted. The second flow facility (small scale) was designed with test fluids that had matched the refractive indices. Details on the rationale of the second flow facility are given in section 3.2.1 and the summary of the two flow facilities is given in Table 3.1.

3.1.1 Large-Scale flow facility (System 1)

There are two flow facilities, namely large-scale (System 1) and small-scale (System 2) flow rigs. The first flow facility is a closed loop system and has an acrylic test pipe with 37 mm ID and 7 m in length. The pipe comes in short sections of 1 or 2 m in length connected with flat flanges with grooves fitted with O-rings made of EPR. The test fluids used for this study are water (density $\rho = 1000$ kg m-^{3} and viscosity $\mu = 0.001$ kg m^{-1}s^{-1}) and Exxsol D140 oil ($\rho = 830$ kg m^{-3} and $\mu = 0.0055$ kg m^{-1}s^{-1}). They are separately pumped from their respective storage tanks by two identical Ingersoll-Dresser centrifugal pumps (power output of 7.5 kW and 60 m head). The flowrate of each fluid is controlled via a recycle line and measured with a flowmeter (ABB Instrumentation Ltd) with accuracy 1% of the full range that varies between 20 L min^{-1} and 250 L min^{-1}. The design of the inlet where the two-fluids join can significantly affect the flow pattern (Barral, 2014). To enhance stratification of the flow at the beginning, a symmetrical Y-shaped inlet is used. The test fluids join at the end of a symmetric Y-shaped junction as shown in Figure 3.1. Alternatively, a splitter plate can be placed to keep the fluids separated for longer distance (Ngan et al., 2011; Al-Wahaibi and Angeli, 2011), but it did not further enhance

stratification of the fluids as previously observed by Barral (2014) hence it was not considered in the setup. The two inlet ducts meet at an inclination of ±10˚ from the horizontal plane which eventually comes together and forms a single duct (Figure 3.2). All ducts have the same pipe ID as the main test section of 37mm. The inlet was designed by the author using a CAD software (Autodesk Inventor) and manufactured in-house from the departmental workshop. The test fluids are introduced according to their densities, where the heavier aqueous phase (water) is injected via the bottom duct and the lighter organic phase (oil) is inject via the top duct. After the test section, the two fluids are led to a separator equipped with a DC 9201/SS/PPL KnitMeshTM coalescer that facilitates the separation of the two phases. The separator has a maximum capacity of 0.8 m^3, a length of about 2 m and diameter of 0.7 m. The inner walls of the separator are made of polypropylene while the coalescer is made of 2 different materials which are weaved into a mesh like shape (Knit Mesh^{TM}). Each material has different affinity to different liquids so it helps coalescence and separation. The mesh is positioned at the center of the separator which may also prevent further development of turbulence within the vessel. The organic and the aqueous phases are then returned from the top and the bottom of the separator respectively into their storage tanks. The storage tanks have a maximum capacity of 800L and are made of fiberglass. The water tank has an additional over-flow attached at the side. It should be noted this system went through a major upgrade with new pumps and pipe-line fittings which was led by the current author. Detailed information on this is given in the Appendix.B.

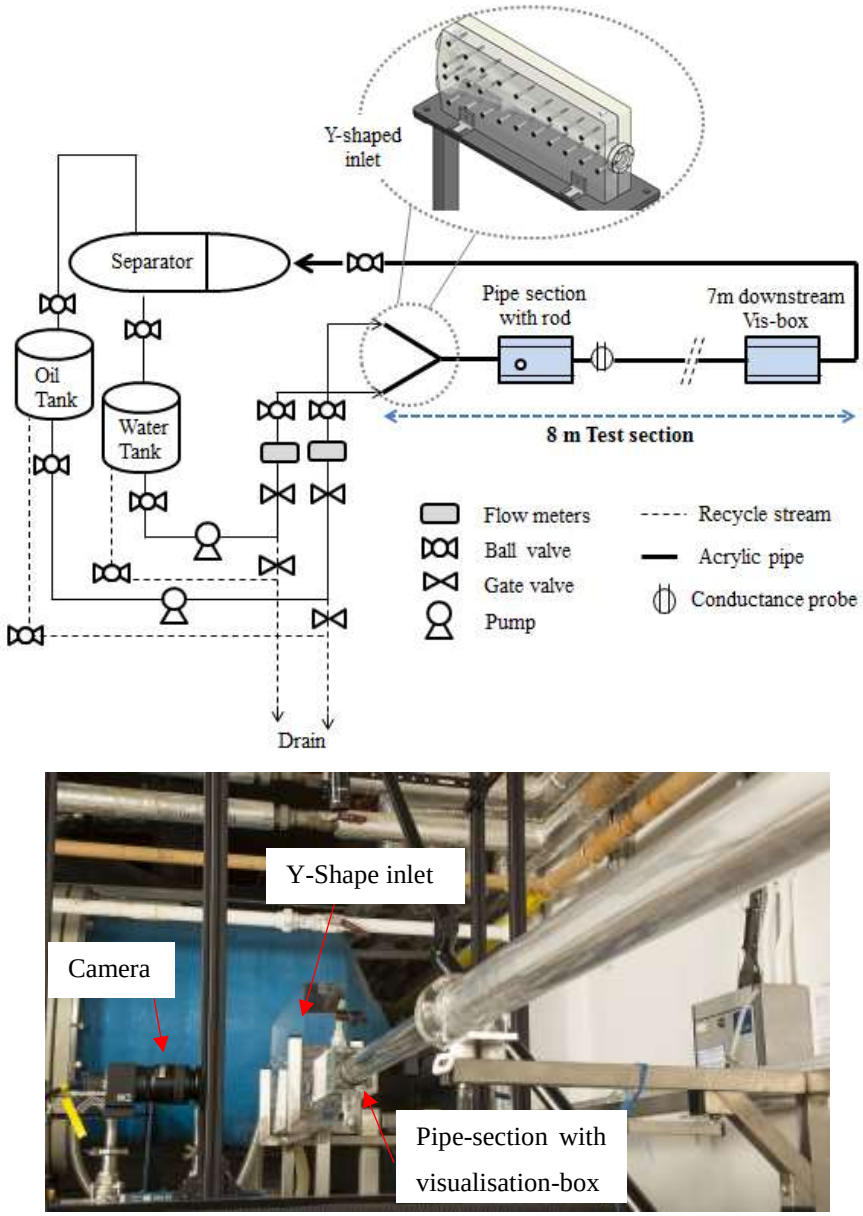

Figure 3.1 Top) Schematic diagram of the large scale (first) flow facility and the symmetric Y-shape inlet. Bottom) Picture of the pipe-section

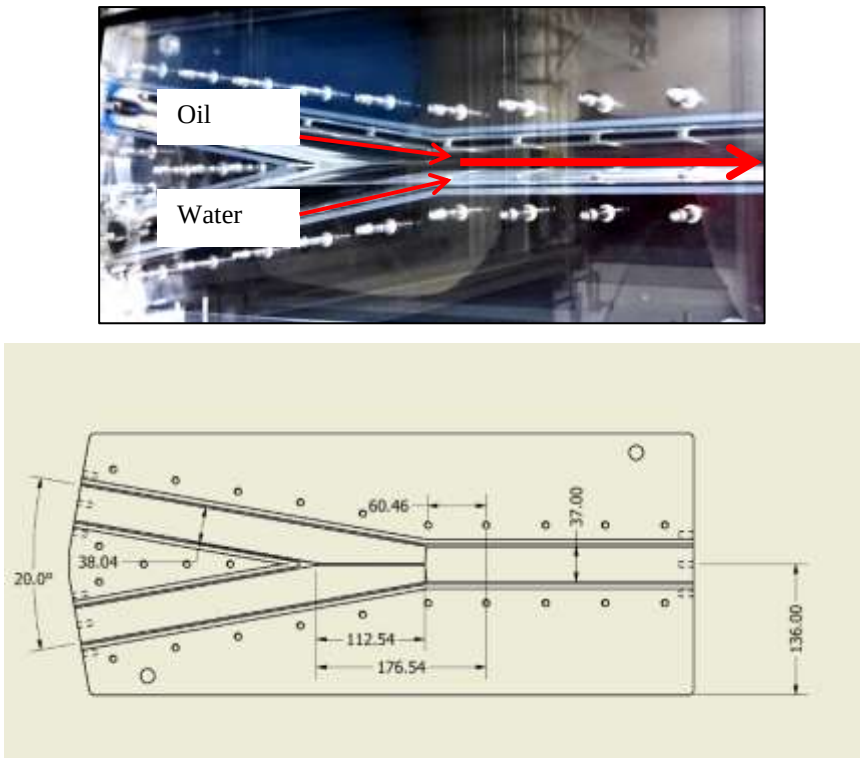

Figure 3.2 Symmetrical Y-shape inlet. Top: picture of the inlet fully installed on the flow rig. Bottom: Schematic CAD drawing of the inlet.

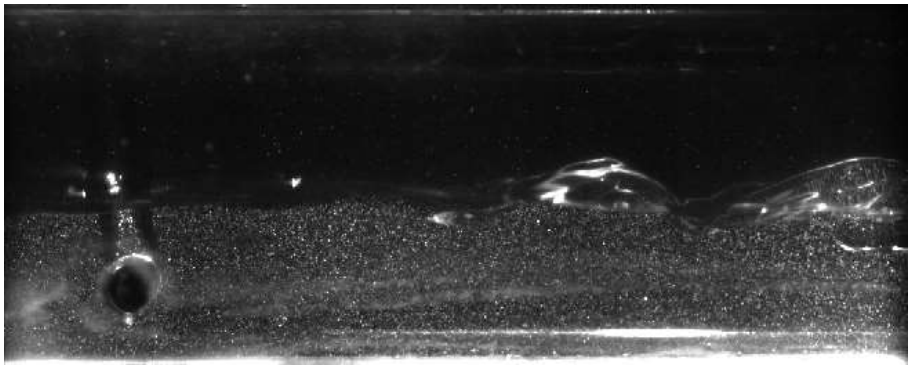

Figure 3.3 Raw PIV image of waves generated behind the cylinder (r = 1.5, Re = 3875). Waves are overexposed to the light due to light scattering near the interface.

3.1.2 Small Scale flow facility (System 2)

In the large scale facility, as the interfacial waves become non-linear, the curvature of the oil-water interfacial waves cause the laser sheet near the interface to be refracted and reflected (See Figure 3.3). From this image it is difficult to extract interfacial wave characteristics such as the amplitude or the wave length as the oil-water interface appears much distorted and also the uncertainty due to the apparent thickness of the interface on the image is large (overexposure near the interface). To avoid this problem, the refractive indices between the two fluids need to be matched. A recent review on the

choices of different solids and liquids are given by Wright et al. (2017). A second flow facility was designed which could run with two immiscible liquid phases that had a matching refractive index.

The overall configuration and the schematic of the second flow system are very similar to the first one (System 1). System 2 has an acrylic test section with 26 mm ID and about 4 m length. The size of the channel is different due to the first system due to the limiting power of the centrifugal pumps already installed on the system. Similarly the pipe comes in short sections of 1 or 0.5 m in length and connected with flanges. The two test fluids are separately pumped from their respective storage tanks by two identical centrifugal pumps. The flowrate of each fluid is controlled via a combination of a recycle loop and control valves, and measured with a variable area flow meter (George Fischer) with accuracy of 1% full range. The fluids join at a symmetric Y-shaped junction that is similar to the inlet section used in the first flow facility. All ducts have the same pipe ID as the main test section of 26mm. Similarly, the test fluids are introduced according to their densities where the heavier aqueous phase (water / glycerol mixture) is introduced via the bottom duct and the lighter organic phase (Silicone oil) is introduced from the top one. The separator is a gravity settler with a capacity of 220 L, from there the organic and the aqueous phases are returned from the top and the bottom of the separator respectively into their storage tanks. The storage tanks for each test fluid have a maximum capacity of 160 L. The test fluids used for this study are water / glycerol mixture (density ρ = 1146 kg m^3 and viscosity μ = 0.0084 kg $m^{-1}s^{-1}$) and Xiameter PMX 5 cSt silicone oil (ρ = 913 kg m^{-3} and μ = 0.0046 kg $m^{-1}s^{-1}$). The aqueous phase (water / glycerol mixture) originally comes as separate solutions, tap water and vegetable cosmetic grade organic glycerin (98 % minimum purity). Water was then added to glycerol until the refractive index n, matched that of the oil, n=1.396. Refractive index of the water / glycerol mixture was measured with Abbe 5 (Bellingham & Stanley) refractometer. The interfacial tension of the liquids was measured with a Krüss® K100C Du Noüy ring instrument while the viscosity of the mixture was measured using an Advanced Rheometric Expansion System (ARES TG-42, TA Instruments®) under constant temperature and for a range of shears. To visualize the oil-water interface, a small amount of Rhodamine 6G Dye was added to the aqueous phase. In addition, for the PIV measurements, Rhodamine B particles were added in the aqueous phases. Addition of the particles and the Rhodamine dye did not have any significant impact on the fluids physical properties such as viscosity or refractive index.

It was found the concentration of the water in the aqueous phase decreased with time as the water evaporated, and this led to a change in the refractive index of the aqueous phase with time. Before each operation, the refractive index was measured and water was added to the aqueous solution until the refractive index fully matched that of the organic phase (Silicone oil, n = 1.396).

3.1.3 Flow conditions

The experimental flow facilities mentioned in sections 3.1.1 and 3.1.2 were used to investigate flow patterns and flow pattern transition from stratified to non-stratified flows with and without the presence of the bluff body. The only control variables that affect the hydrodynamics of the flow are the input

phase flow rates of oil and water. From the flow rates, the superficial velocities can be defined as the volumetric flow rate per unit cross-sectional area of the pipe defined as below:

$$u_{so} = \frac{Qo}{A} \qquad \text{Eq. (3.1)}$$

$$u_{sw} = \frac{Qw}{A} \qquad \text{Eq. (3.2)}$$

Often in the investigation of multiphase flows, instead of using the two parameters above, the mixture velocity and the input flow rate ratio are used, which are defined below:

$$u_{mix} = u_{so} + u_{sw} \qquad \text{Eq. (3.3)}$$

$$r = \frac{u_{so}}{u_{sw}} \qquad \text{Eq. (3.4)}$$

A change in the fluids physical properties from System 1 to System 2 led to changes in the range of flow conditions that could be tested on each flow loop. Flows in System 1 were turbulent while the flows in System 2 were laminar. However, this change in the flow rates were inevitable due the limited choices of the test fluids that had matching refractive indices in System 2, as well as the power of the pre-installed pumps which could not be changed. However, an effort has been made to maintain some of the important design parameters which were discussed in Chapter 2.2, such as the gap ratio and the blockage ratio between the two systems.

3.1.4 Temperature control

Both flow facilities do not have temperature control systems installed. However, the viscosities of the fluids can be affected by the temperature, and experimental runs of short duration (no continuous operation of the rigs for more than 1 hour) were conducted in order to maintain the fluid temperatures at approximately 20℃. It was found that the temperature did not change significantly before and after each experiment with a difference of less than 0.5 ℃. In addition, it was found the difference in the fluids physical properties due to the difference in temperature had negligible impact on the outcome of the two-fluid model. Further discussion on the errors due to the change in the viscosity with varying temperature is discussed in Section 3.5.1.

3.2 Design of the bluff body

Different shapes of bluff bodies have been studied in the past for different purposes, including cylinders, square beams and hydrofoils (Duncan, 1981; Malavasi, 2003; Malavasi and Guadagnini, 2007). However, flows around cylinders have been investigated more extensively compared to other shapes as discussed in Chapter 2. Two pipe sections, one each from each facility, housing the fixed cylindrical

bluff body were designed and two main aspects were considered: 1) The stratified to non-stratified flow pattern boundary in the flow systems without the bluff body; and 2) the geometrical / physical parameters affecting flow characteristics in the wake of the cylinder. Initially the pipe section with the bluff body was designed for System 1. A geometrically similar system was then designed for the small flow facility.

3.2.1 Flow pattern transition boundary

The cylinder needs to be placed in stratified oil-water flows. It was decided to place it in the water phase. Based on visual observations and previous data by Barral (2014), the range of flow rates which produced stratified and stratified-wavy flow patterns was identified. For the large system, time-averaged average mean positions of the interface were identified for high and low oil-to-water input ratios were also considered (see Figure 3.4). To generate spatially localised breaking waves and to avoid direct interaction of the interface with the bluff body, the body needed to be positioned below the mean interface height. The above considerations were taken into account in deciding the geometrical parameters, such as the size and the vertical position of the cylinder.

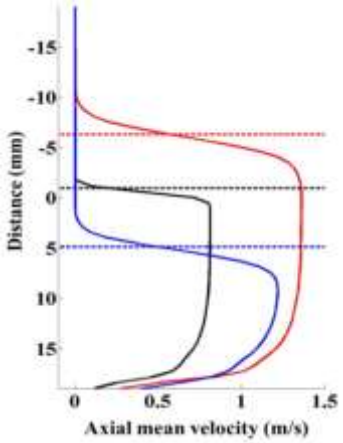

Figure 3.4 Mean axial velocity profile at various input ratios (Re calculated based on the pipe diameter). *Blue: r* = 0.44, *Re* = 13 476; Black: *r* = 1, *Re* = 13 822; Red: *r* = 2.25, *Re* = 29 553

3.2.2 Geometrical parameters

To the author's knowledge there is no previous works on the flows past a cylindrical bluff body in a circular pipe. The cylinder diameter and vertical position were chosen based on available studies similar to the current work considering 3 main dimensionless parameters, γ, h* and the blockage ratio D/D_{pipe} (or L/D for centrally positioned cylinder between parallel walls). Details are given in Table 3.1 for both flow systems. The gap between the rod and the bottom wall, γ, is 1.35 and does not obstruct the formation of von Karman vortices; this value is largely above the critical γ_{crit} of 0.3 - 0.4 as discussed previously in Chapter 2. In addition, the current cylinder position leaves sufficient distance between the cylinder top and the top wall and therefore allows a range of interface heights to be investigated without a direct impact of the interface on the cylinder. The blockage ratio for the current study is 0.13 and was

chosen based on the study by Chen et al. (1995) who found no significant impact on the flow for blockage ratios below 0.5.

3.2.3 Axial location of the bluff body

The distance between the point where the two fluids join at the inlet and the front of the cylinder are 460 mm for System 1 and 650 mm for System 2 respectively. These distances were chosen taking into account two main considerations. Placing the cylinder close to the inlet allows maximum downstream test section length for the studies of waves and drop formation and flow pattern changes. In addition, it was found that Kelvin–Helmholtz waves forming after the inlet are mainly smooth and two dimensional for a short distance but then develop 3D fluctuations further downstream (Barral, 2014). Positioning the rod close to the inlet ensured that only smooth waves would interact with the rod; such waves are more easy to implement as initial conditions in numerical simulations of these flows which will be used to compare in the future against the experimental data.

3.2.4 Final design

Both pipe sections with cylinders installed were manufactured in-house. The bluff body is a cylindrical rod made of acrylic which matches the material of the pipe section. For the two systems respectively, the cylinder has 5 and 3.5 mm OD and is positioned perpendicularly to the flow at 9.25 and 6.5 mm below the pipe center line measured from the pipe bottom wall, which is equivalent to $1/4^{th}$ of the pipe diameter. The gap ratio γ is 1.35 and the blockage ratio is 0.13 as mentioned above. On each section 2 flanges are attached at each end to connect it with the rest of the pipe. In both facilities sections acrylic visualization boxes around the entrance sections (n = 1.49) are filled with glycerol (n = 1.472 @ 20℃) to minimize reflections (Prasad, 2000). Summary of the design parameters used for pipe sections with bluff bodies installed are given in Table 3.1.

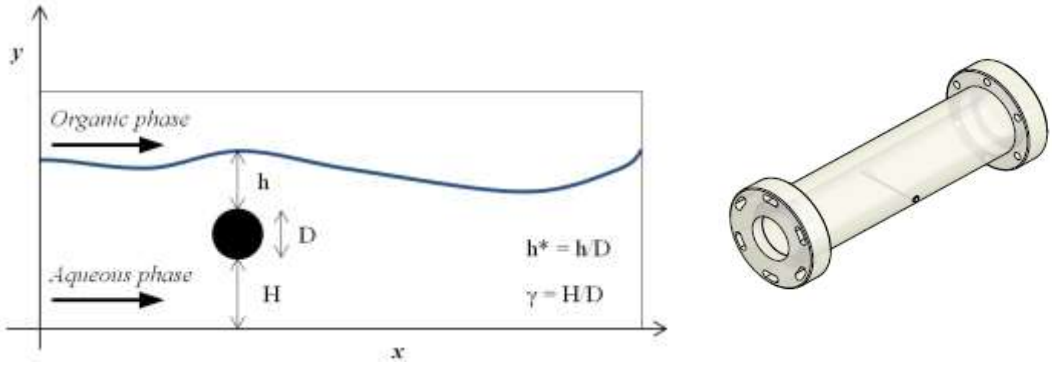

Figure 3.5 Schematic drawing of the pipe section

Table 3.1 Summary of experimental facility specification

	Large-Scale Facility		**Small-Scale Facility**	
Pipe Inner Diameter D, mm	37		26	
Pipe material	Acrylic		Acrylic	
Test section length, m	7		4	
Inlet type	Symmetrical Y-shape inlet		Symmetrical Y-shape inlet	
Measurement location	Approx. 0.46 m and 7 m from inlet		Approx. 0.65 m and 3.5 m from inlet	
Bluff body	Cylindrical rod		Cylindrical rod	
Cylinderical rod size D_{rod}, mm	5		3.5	
Blockage ratio, D/D_{pipe}	0.135		0.135	
Gap ratio, h*	1.35		1.35	
Section length, mm	500		300	
Distance from the wall, H	6.75		4.75	
Test fluids	Water	Exxol D140	Xiameter PMX 200-5 CS Silicone Oil	Water / Glycerol mixture (~50% wt)
Density, kg/m3 @ 20℃	1000	830	913	1146
Viscosity, cP @ 20℃	1	5.5	4.6	8.3
Refractive Index, *n*	1.33	1.459	1.396	1.396
Interfacial tension, mN/m @ 20℃	39.6		31.6	
Seeding particles	Silver coated hollow glass particles		Rhodamine B coated PMMA particles	
Particle size, μm	12		1 ~ 20	
Particle density, kg/m3	1220		1180	

3.3 Measurement techniques

Two main experimental techniques were implemented in the flow facilities; high speed imaging and high speed Particle Image Velocimetry. Setups on each flow facility are described in the following sections.

3.3.1 Volume illuminated high speed imaging

Volume illuminated high speed imaging is by far the most commonly used technique in observing flow patterns (Chapter 2). This technique was implemented on the large-scale facility. Measurements were carried out at two axial locations separately, 0.46 m and 7 m from the inlet, as simultaneous measurements were not possible due to the availability of the camera. Recording at 0.46 m was used to obtain interfacial wave characteristics shortly downstream of the bluff body while at 7 m downstream it was used to identify the corresponding flow patterns. For the measurements the camera is positioned perpendicularly on the side of a visualization box filled with glycerol. A Photron SA-1 High Speed Camera equipped with a 105 mm Nikon lens is used with typical recording speed between 2000 – 4000 fps at maximum resolution of 1024 x 1024 pixels. For illumination, white back light was used with adjustable angle and intensity controlled by the distance from the pipe. A translucent paper was place in front of it to make the light intensity homogeneous across the entire field of view. For each set of conditions the total number of images recorded was 6000 to 8000.

3.3.2 High speed Particle Image Velocimetry (PIV)

High speed PIV can provide information on the velocity field of the seeded phase. This technique was implemented on both flow systems. A schematic of the setup used for system 2 is shown in Figure 3.6. For measurements on System 1, the aqueous phase was seeded with silver coated hollow glass particles with 10 µm diameter (Litron Lasers, Ltd). In order to check whether the particles follow the flow well, the Stokes number, which is a dimensionless number defined as the ratio between the characteristic time of a particle to a characteristic time of a flow, is computed. Stokes number close to 0 means the particle represents the flow very well. The computed Stokes number for this system was in the order of 10^{-4} which is very close to 0.

A double pulsed Nd-YAG Laser (TSI instruments) with 532 nm wavelength was used to illuminate the flow from underneath the pipe. The light sheet was generated using a classical expanded laser beam optical system (Adrian & Westerweel, 2011). Optical lenses were arranged so that the laser sheet was vertical in the middle of the pipe section along the pipe axis. The estimated laser sheet thickness was about 1 mm. The typical curvature of the interface in the transverse direction is estimated to be of the order of 10 mm. Consequently the optical distortion from the curvature of the interface in the transverse direction can be neglected. Further optical distortions at the interface are avoided as the laser plane enters in the water phase. Images were recorded with the high speed camera (Photron SA-1) with maximum resolution (1024×1024 pixels). The camera was located perpendicular to the laser sheet and was equipped with a 105 mm Nikon lens. The acquisition frequency of the camera was set to twice the frequency of the laser pulse emitted by each of the laser cavities. The time separating pairs of images

defines the minimum time separating two consecutives velocity fields. The time δt, separating two consecutive images is equal to the inverse of the camera acquisition frequency. For the same image magnification and spatial resolution, the sampling frequency in the PIV measurements varied depending on the flowrates. The maximum image acquisition frequency corresponding to the minimum δt was 3 kHz (i.e. δt = 0.333 ms). The image acquisition was triggered by the laser pulse using a synchronizer (TSI Instruments). For each set of conditions the total number of images recorded was 6000 to 8000.

3.3.3 Simultaneous high speed Planar Laser Induced Fluorescence and PIV

Planar Laser Induced Fluorescence, PLIF, was used to visualize the flow when the refractive indices between the two phases were matched. Unlike the volume illuminated imaging, the flow only on the plane illuminated by the laser is visible. This technique simultaneously allows PIV to be conducted. The simultaneous PIV / PLIF technique is implemented on the small flow rig system. A small amount of aqueous Rhodamine 6G dye was added to the water/glycerol phase to help distinguish between the two liquids and better track the interface. Rhodamine B coated PMMA particles (1180 kg m^{-3} with a particle size, d_p, ranging from 1 to 20 μm) were used as tracers to acquire the corresponding velocity fields of the aqueous phase. The Stokes number was found to be <<1 for all the range of conditions investigated.

For both the PLIF imaging and PIV (as shown in Figure 3.6), a DPSS green continuous laser system by Laserglow Technologies® with 532 nm wavelength and 3000 mW power is used to excite the Rhodamine dye and the seeded particles. Both the absorbance of the dye and the particles' peak at approximately 530 nm and emit above 590 nm. A Laser sheet was generated from underneath the pipe using a classical expanded laser beam optical system (Adrian & Westerweel, 2011). Optical lenses were arranged so that the laser sheet is vertical in the middle of the pipe section along the pipe axis. The estimated laser sheet thickness was about 1 mm. Images were recorded with the high speed camera (Photron SA-1) with maximum resolution of 1024×1024 pixels. The camera was located perpendicular to the laser sheet and was equipped with a 100 mm Tonika lens fitted with high-pass sharp edge filter (<580 nm) to eliminate any reflections or spurious light from the laser. The optical measurements were performed at two axial locations, 0.65 and 3.5 m from the inlet. Unlike the laser used in the large-scale facility, for the current setup a continuous laser was used which means that the camera and the laser do not require synchronization. The minimum separation time δt between two consecutive image pairs is only limited by the frequency of the camera. A typical acquisition frequency of the camera was 4 kHz. For each set of conditions the total number of images recorded was 6000 to 8000.

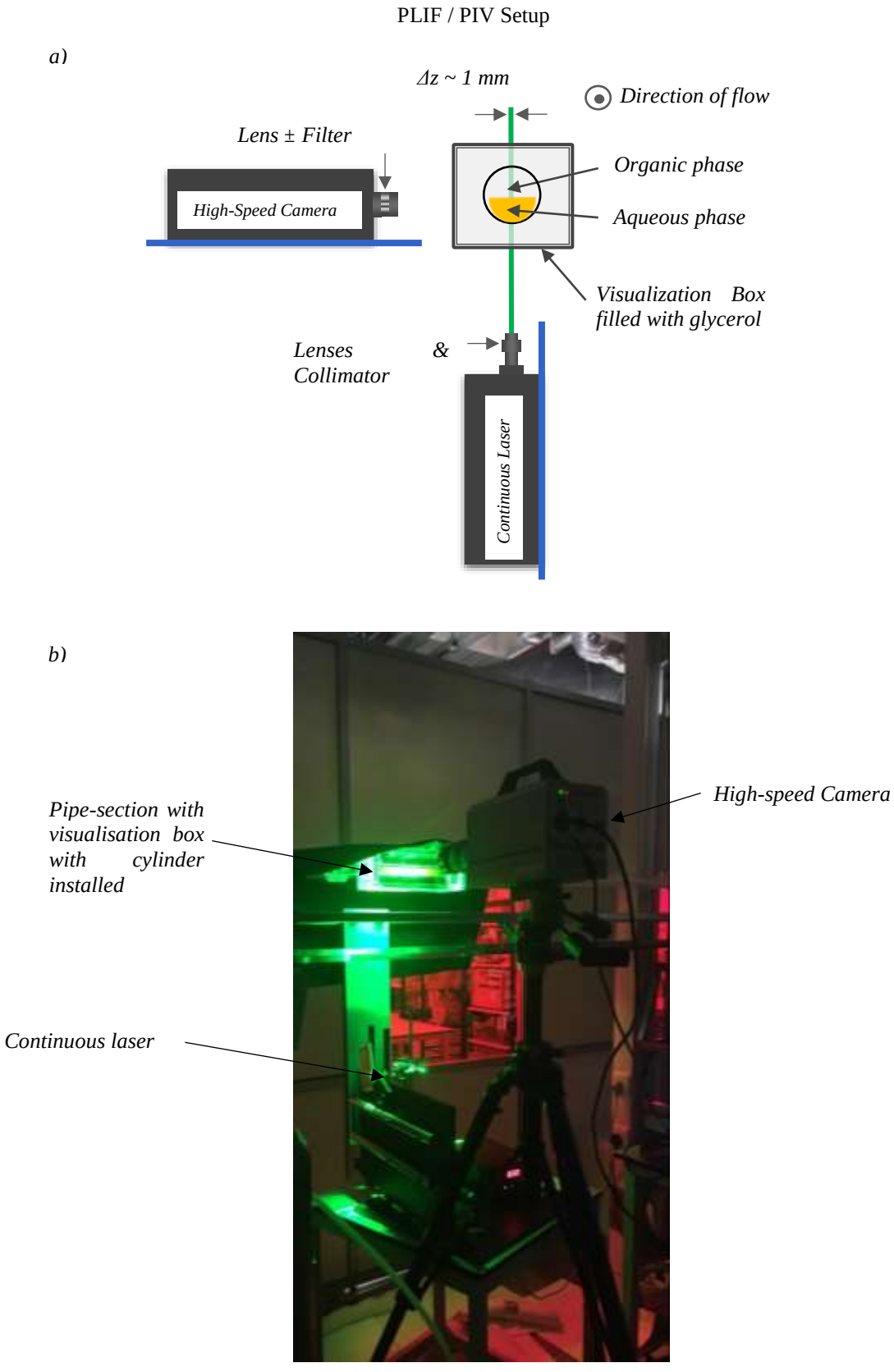

Figure 3.6 a) Schematic diagram of the PIV / PLIF setup. b) Picture of the PIV / PLIF setup

3.3.4 Conductivity probe

A double-wired conductivity probe was used to obtain local average interface height. The probe was made in-house and consists of two stainless steel wires, 0.5 mm in diameter, 5 mm apart, installed perpendicularly to the direction of the flow. The two wires form part of an electrical resistance circuit whose signal depends on the height of the water layer between the two wires in separated oil–water flows. The signal gives the variation of the interface height with time at this particular axial location in the pipe. This type of probe has been used widely in gas–liquid and liquid–liquid flows to investigate interfacial waves. Data was collected at 256 Hz over a period of 4 min. Single phase water measurements were also carried out to account for any variations in the conductivity of the water phase. The data collection and the processing methodology have been described in Barral and Angeli (2013). The probe was located just after the bluff body (19D) to obtain the average interface immediately downstream the cylinder. The probe signal represents the interface height reliably only when there are no or very few drops of one phase into the other which limits the range of flow rates it can be used.

3.4 Data processing and analysis

3.4.1 Wave characteristics

From the high speed imaging in both flow rig systems the following wave characteristics were studied: average interface height, wavelength, wave amplitude, wave velocity and wave frequency. Two different approaches were used to obtain the data from the raw images which are presented below for each technique used.

3.4.2 Volume illuminated imaging in large scale facility

The characteristics of waves were acquired directly from the high speed images. In each image, several measuring locations, x, were chosen at fixed distance from the cylinder and equally spaced apart, as shown in Figure 3.7 The fixed locations were 40, 55.9, 71.8, 87.7 and 103.6 mm away from the rod. During the above calculations, the main source of uncertainty arises during the data extraction process from the high speed images. The uncertainty is estimated to a maximum of 5 pixels (0.16 mm/pixel) or 0.8 mm, which is equivalent to the apparent thickness of the interface on the images.

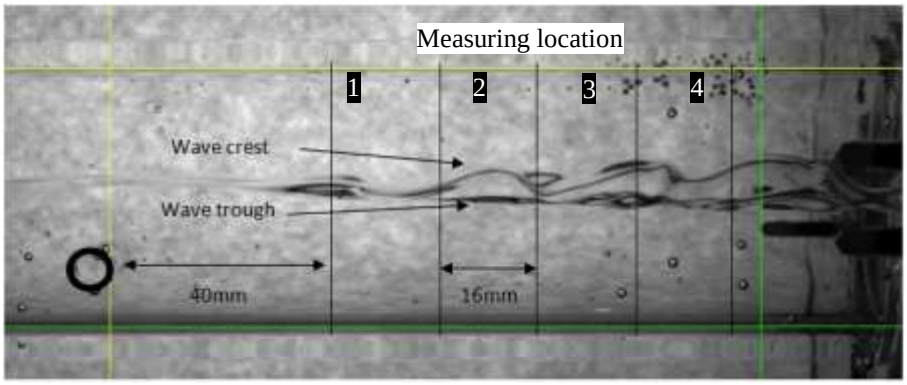

Figure 3.7 Image of waves generated behind the bluff body (Umix=0.62 m/s, r=1). The locations used in the wave analysis are shown

Average interface height

To calculate the *local average interface height* at each measuring location the height of the interface is recorded in pixels every 10 ms for 1.5 seconds. For each measuring location *m* where m = 1,…,5, the data acquired are averaged to obtain the local interface height. The local time-average interface height $\overline{h}$ at measuring location *m* can be defined as:

$$\overline{h}_{x_m} = \frac{1}{N} \sum_{i=1}^{N} h_{x_m,i} \;\; where\; i = 1 \ldots N \qquad \text{Eq. (3.5)}$$

where h is the interface height measured at location x_m and i varies from 1 to N, where N is the size of the sample size.

Wave amplitude

Given the local average interface height, the *local average wave amplitudes* are calculated by subtracting the local average interface height from individual wave crest positions, which are then averaged for each measuring location. Waves are linear and follow sinusoidal motion where clear peak and trough can be clearly identified visually. The local average wave amplitude $\overline{A}$ is defined as:

$$\overline{A}_{x_m} = \frac{1}{M} \sum_{j=1}^{M} [A_{x_m,j} - \overline{h}_{x_m}] \;\; where\; j = 1 \ldots M \qquad \text{Eq. (3.6)}$$

where *A* is the y-position of an incident wave crest *A* at location x_m and j varies from 1 to M, where M is the size of the sample size.

Wave velocity

To calculate the *local average wave velocity* individual wave crests were tracked in the direction of flow and the time taken for each crest to travel past each measuring location was recorded. The wave velocities were then averaged to obtain local average wave velocity per measuring location. The time difference between two successive crests or troughs passing through a measuring location was also recorded. Given that the distance between two adjacent measuring locations, m and n where *n = m+1* and m = 1,…,5, a total of 4 local average wave velocities $\overline{v}$ can be obtained and it is defined as:

$$\overline{v}_{x_{mn}} = \frac{x_{mn}}{\mathrm{M}} \sum_{k=1}^{\mathrm{M}} [\tau_{x_m,k} - \tau_{x_n,k}] \;\; where\; k = 1 \ldots P \quad \text{Eq. (3.7)}$$

τ is the instantaneous time at which the crest *k* flows past a measuring location x_m and k varies from 1 to P which is the sample size. The average wave velocity *V* for each flow condition travelling in the direction of the flow from the first to the last measuring location is also computed by averaging the 4 local average wave velocities.

Wavelength

Knowing the average wave velocity *V*, the *local average wavelength* could be computed from the time a pair of crests or troughs needed to travel past each measuring point. Local average wavelength λ at each measuring location *x* is given by:

$$\lambda_{x_m} = \frac{V}{\mathrm{M}} \sum_{k=1}^{\mathrm{M}} [\tau_{x_m,k} - \tau_{x_m,k+1}] \quad where\ k = 1 \dots P \qquad \text{Eq. (3.8)}$$

Wave frequency

Wave frequencies were also computed from the number of wave crests and troughs travelled past the measuring locations. The wave frequency is also an inverse of the average time between consecutive pairs of wave crests travelling past a measuring location which can be written as:

$$f_{x_m} = \frac{V}{\lambda_{x_m}} \qquad \text{Eq. (3.9)}$$

3.4.3 Planer Laser Induced Fluorescence

Obtaining wave characteristics via PLIF images takes on the same basic calculation procedures mentioned in section 3.4.1, except the images require pre-treatment for more accurate results. The image pre-treatment procedure is first described below followed by interfacial wave analysis procedures.

Image pretreatment

The original images obtained from the high speed camera are in grey-scale. To identify the exact position of the oil-water interface, a global threshold level was first computed using the method by Otsu (1979) and the raw images were binarised into black and white images accordingly for each flow condition. Due to the difference in the intensity between the particles and the aqueous phase, artefacts (holes) may be generated after the first stage of the binarisation process. As a second step these holes were filled via a closing process. This process includes a dilation step followed by an erosion step, where the boundaries of the foreground region are enlarged (bright region in the binarised image) and the background (black) regions are shrank filling the holes. The uncertainty in the position of the interface is estimated to a maximum of 2 pixels (0.432 mm/pixel for the high and 0.0942 mm/pixel for the low magnification cases), which is equivalent to the size of the structuring element (i.e a grid with a chosen size) to fill the holes in the images. This error is mainly caused by the slight mismatch of the refractive indices of the fluids which can blur the interface. This image pretreatment process is illustrated in Figure 3.8. The data processing was carried out in MATLAB.

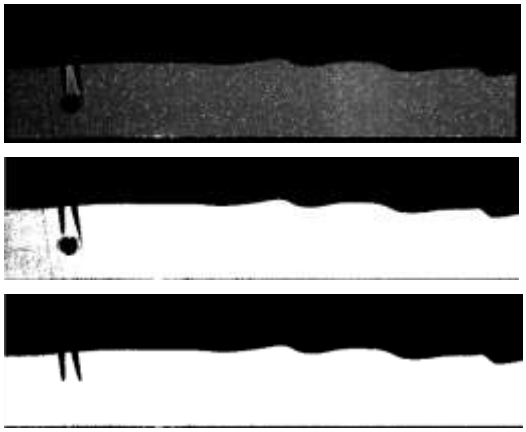

Step 1) Raw image before any treatment

Step 2) After binarisation

Step 3) After filling holes using structuring element

Figure 3.8 3 stages of image pretreatment

Average interface height

For the computation of the average interface height Equation 3.5 is used. The number of axial measuring location *m* is refined by the resolution of the image in this case where m = 1024, as the images were recorded at a full resolution of the camera of 1024 x 1024. The actual position of the interface was identified by detecting the vertical location at which the binary value of the pixel changed from 0 to 1, counting from the top pipe wall to the bottom one. This process was done using MATLAB. The final data obtained is stored in a 2-D matrix format where columns represent axial measuring locations (or distance from the cylinder) and rows represent time. Each column in the matrix obtained above, $h_m(t)$, represents fluctuation of the interface over time at one chosen measuring location which can be treated similar to that of a times-series data. The average interface height is obtained by averaging the rows at each measuring location.

Wave frequency

The average wave frequency at each measuring location is obtained through the use of Fast Fourier Transform (FFT) of the input signal $h_m(t)$. Following the procedure proposed by Barral and Angeli (2014), the power spectrum of the frequencies is computed to obtain the most dominant frequency of the input signal. A typical power spectrum of the frequencies obtained is given in Figure 3.9.

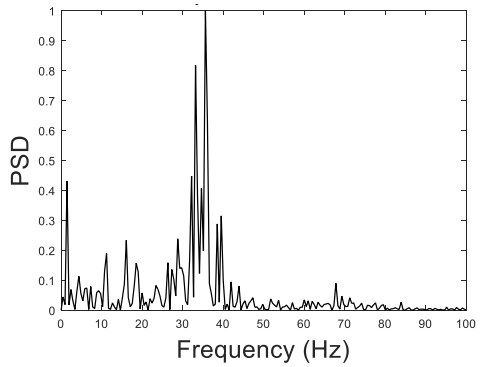

Figure 3.9 Normalized Power Spectrum Density (PSD) of the interface signal
Fr = 2.23 h* = 0.69

Wave amplitude

The local average wave amplitude is calculated using Equation 3.6 except the positions of the individual wave crests are automatically detected via the peak detection algorithm in MATLAB. The peaks are detected when a data point is larger than its two neighbouring samples, i.e $h_m(t_i) > h_m(t_{i+1}), h_m(t_{i-1})$, where the i = 1,…,N and N is the total number of data samples (equivalent to the total number of images recorded). The obtained peaks are then filtered by applying a minimum threshold level to detect peaks that are above the average interface height. Lastly, minimum separation distances between the peaks, which are determined based on the frequency of the interfacial waves obtained previously, are applied in MATLAB.

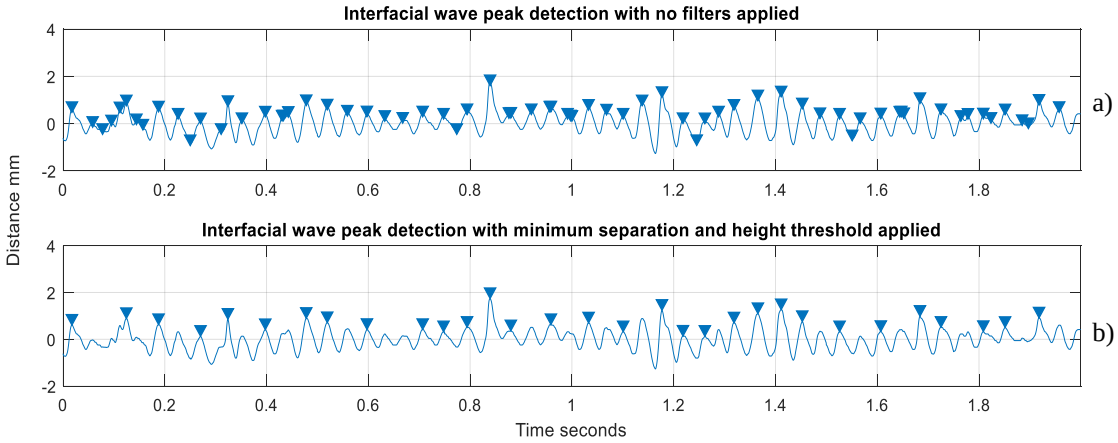

Figure 3.10 Comparison of peak detection with (a) no filters, and (b) minimum separation and minimum height threshold applied. Fr = 1.86 h* = 1.15

Wave velocity

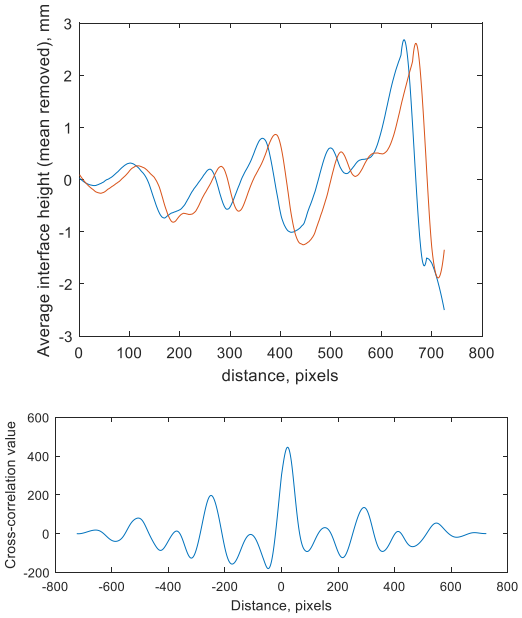

Figure 3.11 a) Two instantaneous signals representing the interfacial shape measured from the end of the cylinder (0 on x-axis) separated by δt. b) Cross-correlation of the two signals given in a) and the peak represents the spatial shift of the signal measured in pixels

The average wave velocity in the axial direction is computed from the cross-correlation between two spatial signals, representing an instantaneous profile of the interface shape, separated by time, δt (*h(t)* and *h(t + δt)*). Pairs of spatial signals are cross-correlated to give an average lag of the signal which represents a distance (given in number of pixels) which the signal has shifted over the chosen period of time *δt*. An example of the raw signals used to compute the wave velocity is given in Figure 3.11.

3.4.4 Computation of the velocity fields

The 2D velocity fields were computed using two different software programs, namely Insight4G (TSI instruments) and JPIV. Depending on the spatial resolution of the obtained images, different sizes of the correlation boxes were chosen. Typically for the images recorded on the large flow system (System 1), the data was first logged in a computer and the 2D velocity fields were calculated with Insight4G (TSI, instruments). The pixel size was 0.094 mm and velocity fields were computed using a 32×32 pixel correlation box with 50% spatial overlapping which gives a spatial resolution for the velocity vectors of 1.5 mm. The range of velocities that can be measured depends on the inverse of the frequency of the camera. For each flow condition we fixed the maximum velocity magnitude to correspond to the half part of the correlation box. Consequently, the range of velocity magnitudes (which depends on δt) was from 1 pixel/ δt to 16 pixels/ δt. For the second flow system the velocity fields were obtained using JPIV. The pixel sizes varied between 0.0942 and 0.0432 mm between different magnifications, and velocity fields were computed either using a 16 x 16 correlation box at both magnifications. Similarly, 50% spatial overlapping was used in both cases. Typically the spatial resolution for velocity vectors varied from 0.0942 mm to 0.75 mm for images captured with low magnification (pixel size of 0.0942).

3.5 Error analysis

In this section an error analysis is carried out on possible sources of error affecting the PIV measurements. Systematic errors inherent in the setup of the PIV system are discussed in section 3.5.1 and statistical error due to the sample size is given in section 3.5.2. Relevant errors from data other than the PIV are mentioned within the text in results section.

3.5.1 Systematic errors inherent in PIV measurements

There are two possible errors that may arise during the preparation of the experiment which are: 1) errors during the alignment of the laser in the central plane of the pipe; and 2) errors during the positioning of the high speed camera perpendicular to the visualization box.

The alignment of the vertical laser plane was made using two reference holes with a diameter of 4 mm, which are found on each side of the visualization box. The holes are in line with the central plane of the pipe as shown in Figure 3.12. The possible maximum alignment error ε_L corresponds to the extreme condition where the laser is tangent to two opposite sides of the reference holes. An estimate of the possible maximum angle is defined as:

$$\emptyset_{Lmax} = \arctan\left(\frac{d_{hole}}{X_{hole}}\right) \qquad \text{Eq. (3.10)}$$

where d_{hole} and X_{hole} are the diameter of the reference hole and the distance between the reference holes. From this the maximum alignment error can be calculated from Equation 3.11.

$$\varepsilon_L = \frac{\emptyset_{Lmax}}{180} \qquad \text{Eq. (3.11)}$$

For a perfectly aligned the $\emptyset_{Lmax}$ would be equal to zero. It was found that $\emptyset_{Lmax}$ for System 1 and System 2 are 1.15° and 0.459°, respectively. The corresponding maximum alignment error for the two systems were 0.64 % and 0.26 % respectively. The test section is rigidly fixed on to the supporting frame made of steel and the alignment of the laser was carried out only at the beginning of each experimental run.

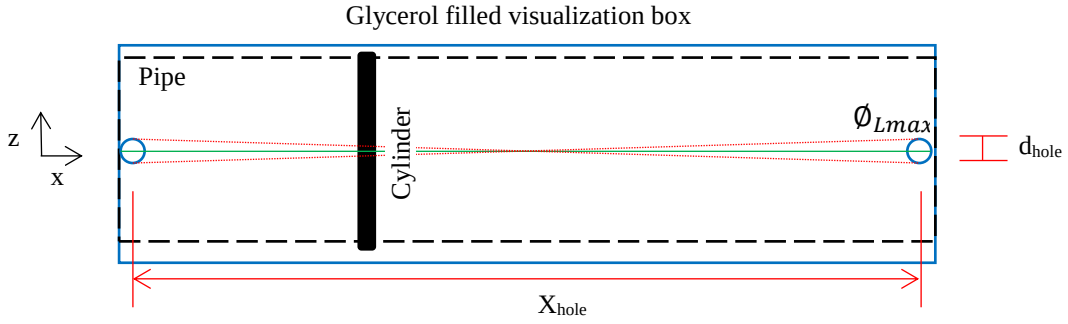

Figure 3.12 Schematic diagram representing the maximum error during laser alignment with reference holes shown

The second source of error is associated with a calibration factor and this error may arise during the alignment of the camera in perpendicular position to the visualization box to minimize optical distortion. Two methods were implemented to minimize this error. In the first method, the size of the inner pipe diameter. By detecting the positions of the upper and lower pipe walls on each end of the pipe, the angle of skewness perpendicular to the surface of the visualization box in the x-direction can be identified. In an ideal condition, the position of the pipe walls, both upper and lower, would appear horizontal along the x-axis in the image. The maximum error was equivalent to 4 pixels, which is equivalent to the apparent thickness of the pipe wall on the image for the large flow system. For the small flow system, a statistical approach was implemented where the pipe walls were detected using the binarised images following the procedure mentioned in Section 3.4.1.2, and the error is equivalent to 1 pixel in this case. The second method consists of checking if the seeding particles are in focus over the entire field of view (interrogation area) of the camera. This is done after the laser has been fully aligned. This method helps to detect the skewness angle relative to the z-axis. This process was repeated until the camera was

fully aligned. The maximum error found during the camera alignment ε_C for the large and small flow systems is 2.22 % and 0.73 % respectively.

The overall experimental error in the PIV measurement can be estimated using Equation 3.13 in agreement with Moffat (1988). It is defined as:

$$\varepsilon_T = \sqrt{\varepsilon_L^2 + \varepsilon_C^2} \qquad \text{Eq. (3.13)}$$

The total error in the measured velocity gives an estimate ε_T of 2.31 % and 0.78 % for Systems 1 and 2 respectively.

It was mentioned earlier in section 3.1.4 the difference in the temperature of the test fluid can vary and this also affects the physical properties of the test fluids. It was found that the temperature change before and after the experiment was in the range of ±0.5 ℃. The fluids viscosities at different temperatures are given in Table 3.2 below. Based on the predictions of the two-fluid model (Appendix. A), this change in the physical properties of the test fluids due to the temperature is found not sufficient to have a big impact on the flow. The magnitude of the change in the position of the average interface height was in the order of 0.1 mm.

Table 3.2 Fluid viscosity at various temperatures

Test fluids	Viscosity (cP) at different temperatures		
	(19.5 ℃)	(20.0 ℃)	(20.5 ℃)
Water	1.027	1.002	0.978
Glycerol/Water mixture	8.54	8.3	8.14

3.5.2 Statistical error

Justification on whether the size of the samples acquired is enough to minimize statistical errors is given below. Statistical errors considering two main parameters, position of the interface and the velocity components. A typical image of the flow immediately downstream the cylinder is given in Figure 3.13 with points denoted as A, B, C and D, identifying the locations where the variation of the cumulative mean of interface height h_{cum} or the cumulative mean of the velocity components $|U_{cum}+V_{cum}|$ are considered against the sample size Ns. Equations used to compute the corresponding values of h_{cum} and $|U_{cum}+V_{cum}|$ are given below.

$$h_{cum} = \sqrt{\frac{\sum_{i=1}^{N_s}(h_{x_m,i}^2)}{N_s}} \qquad \text{Eq. (3.14)}$$

$$|U_{cum} + V_{cum}| = \sqrt{\frac{\sum_{i=1}^{N_s}(h_{x_m,i}^2)}{N_s}} \qquad \text{Eq. (3.15)}$$

It can be seen that beyond Ns > 1000 in all figures the magnitude of the cumulative average values tend to converge to almost a constant value. Fluctuations of the interface height at Ns > 2000 are less than 0.1 mm while fluctuations of the U + V velocity components are less than 0.1 pixels. To minimize the statistical errors a maximum sample size of 8000 were selected in this work.

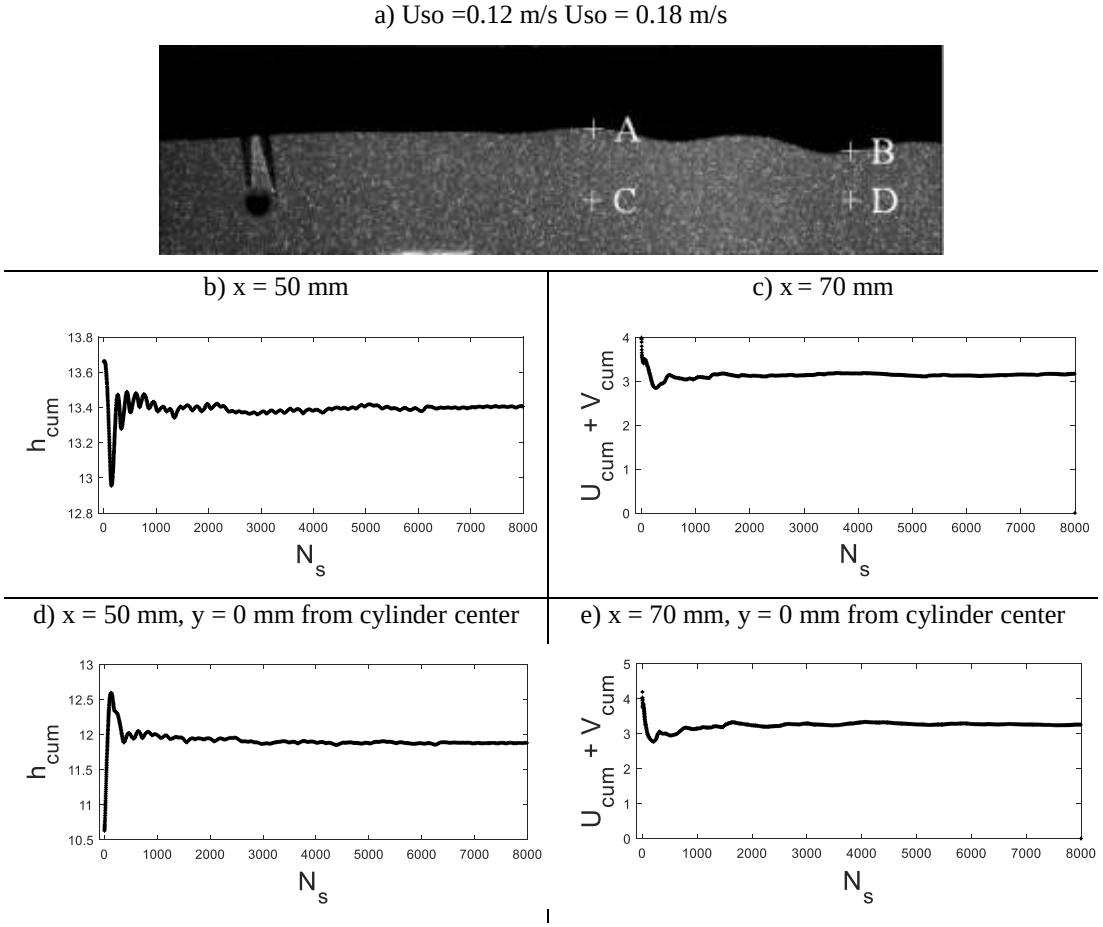

Figure 3.13 a) Instantaneous capture of the flow immediately downstream the cylinder at Uso =0.12 m/s Uso = 0.18 m/s, with point of measurements denoted. Variation of cumulative average against the number of images at A (b); B(c); C(d); D(e)

CHAPTER 4. FLOW PATTERNS AND WAVE CHARACTERISTICS

In this Chapter, the results obtained on the first system (System 1) via high speed imaging are presented using water and Exxsol D140 (density 830 kgm^{-3} and viscosity 5.5 cP) as test fluids. Section 4.1 describes the observed flow patterns at 7 m downstream the inlet with and without the cylinder while section 4.2 describes the wave characteristics extracted from the images taken immediately downstream from the cylinder. A brief summary of the Chapter is given in section 4.3.

4.1 Flow patterns at 7 m downstream the inlet

Flow patterns were observed in both cases without and with the bluff body with the high speed camera at 7 m downstream the inlet (189D). Experiments were carried out for mixture velocities between 0.62 - 2.17 m/s and input oil-to-water flow rate ratios between 0.29- 3.5. The flow patterns identified in both cases are plotted in Figs.4 and 5 in terms of mixture velocity, Umix, against oil to water input flowrate ratio, r. Three different flow patterns were observed in both systems with and without the bluff body installed. The patterns when no bluff body (Figure 4.1a) was present showed good agreement with patterns identified in previous studies in the same system (Barral and Angeli, 2013). The intermediate, INT, pattern was only observed in the system without the rod, (r range between 0.5 - 2.5 and Umix range between 0.62 - 1.55) while stratified, ST, and dual continuous, DC, flows appeared in both systems. In the system with the bluff body, a new pattern was seen, dual continuous flow with oil drops in water only, DC & Oil drops in water.

The transition from stratified to non-stratified flows occurs with increasing mixture velocity in both cases. The transition was considered to have taken place when a droplet of either oil or water first appears. This transition is delayed to higher mixture velocities at flow rate ratios around 1, where the relative velocities between the two phases are low, in agreement with previous work (Barral and Angeli, 2013). The presence of the bluff body reduces the region of stratified flow significantly (see Figure 4.1b). The transition boundary with the bluff body is found at a much narrower range of r between 0.4-1.5 and Umix between 0.62-1.09 m/s compared to the transition boundary without the rod (dotted line shown in Figure 4.1b). This suggests that the rod actuates the transition between the patterns.

a)

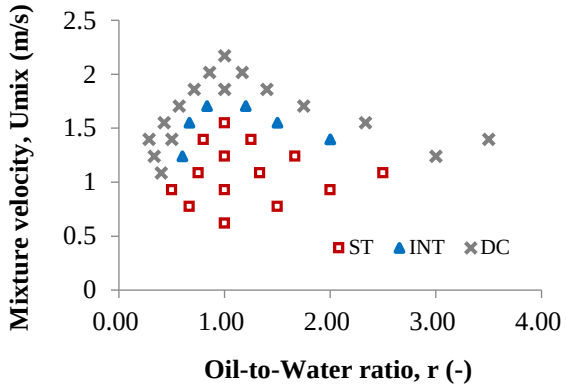

b)

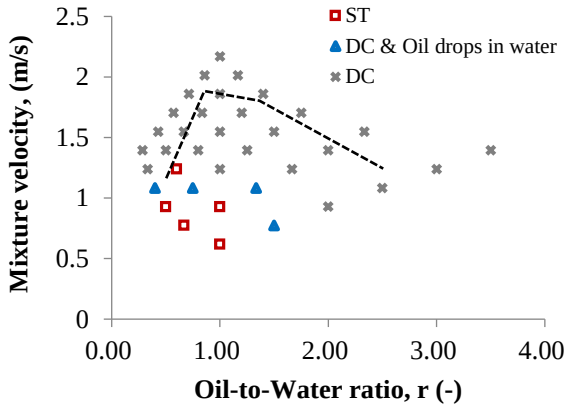

Figure 4.1 Flow pattern map at 7m downstream the inlet a) when there is no bluff body installed b) with the bluff body installed. Dashed corresponds to the boundary between stratified wavy (SW) and dual continuous (DC) patterns without the cylinder as shown in a).

4.1.1 Stratified flows (ST)

Stratified flow with smooth interface was only observed when there was no cylinder at the lowest mixture velocity studied, Umix = 0.62 m/s, and equal phase flowrates (see Figure 4.2). For the same flow condition small fluctuations of the interface were observed at 7 m from the inlet with the addition of the bluff body. In general, at low velocities waves formed after the inlet decayed downstream. Barral et al. (2015) in flows without a bluff body also found that waves gradually fade with distance. With increasing mixture velocity in both cases with and without bluff body, the waves persist in the downstream location. Figure 4.2b shows stratified (ST) flows for the two systems at higher mixture velocities (Umix = 0.78 m/s, r = 0.67). As can be seen, the interfacial waves are more prominent when the bluff body is present.

4.1.2 Dual continuous flow (DC)

In this pattern both oil and water retain their continuity at the top and the bottom of the pipe respectively while drops of one phase appear into the other. The degree of dispersion depends on the mixture velocity and the phase flowrate ratio. This regime appeared in both systems at high mixture velocities. As the

velocities increased the drop size decreased. When the rod was present, for the same flow conditions, more drops appeared in the phases as can be seen in Figure 4.2c. For similar mixture velocities, drops are larger and of similar size in the case of small input ratios ($r \leq 1$), while they are generally smaller with variable sizes at large input ratios ($r \geq 2$). Barral et al. (2015) also observed qualitative difference in the average droplet size in the dual continuous regime between low and high input flowrate ratios.

A particular case of the dual continuous pattern is the *Dual continuous flow with oil drops in water (DC & Oil drops in water),* where only oil drops appeared in the water phase. This flow regime was only observed in the system with the bluff body in place for a narrow range of Umix (1.09 - 0.78 m/s) and input ratios (1.5 - 0.4) (Figure 4.2d). The oil drops are large compared to the other DC cases. The overall shape of the interface appeared wavy but the wave surfaces were rather smooth which suggests that the drops found at these flow conditions must have been formed upstream (i.e. behind the bluff body). For the same flow conditions in the system without the bluff body the flows were stratified wavy.

4.1.3 Intermediate flow

This regime was only observed in the system without the bluff body, between stratified and dual continuous flows. It is characterized by continuous phases of oil and water with fluctuating interface and the appearance of small sporadic drops in the two phases. The size of the droplets is smaller than in the DC regime. Mixture velocity and input flowrate ratio did not affect significantly the appearance of the interface. With the addition of the rod, under the same conditions, the flow was dual continuous (Figure 4.2e).

4.2 Flow immediately downstream the bluff body

The visual observation of the flow patterns revealed that the rod had a significant effect on the flow which persisted 7 m downstream the inlet. This effect on the flow and the waves generated were studied immediately after the rod for mixture velocities ranging between 0.62 - 1.24 m/s and input flowrate ratio, r, varying between 0.67 - 1.5 (a total of 7 conditions). The flow conditions were chosen for two main reasons. Within this range, the interface did not directly impinge on the rod. In addition, for flow conditions outside this range, due to Kelvin-Helmholz instability, waves with large amplitudes and 3D fluctuations form. For the limited conditions investigated, Kelvin-Helmholtz waves form after the inlet but they are mainly smooth over the short distance between the inlet and the rod. This allows only smooth waves to interact with the rod which would make modelling easier (Chaplin, 1984). In addition, waves observed outside these flow conditions after the cylinder were strongly non-linear and difficult to analyze from the images. A total of 80 waves were extracted from the high speed images for each flow condition.

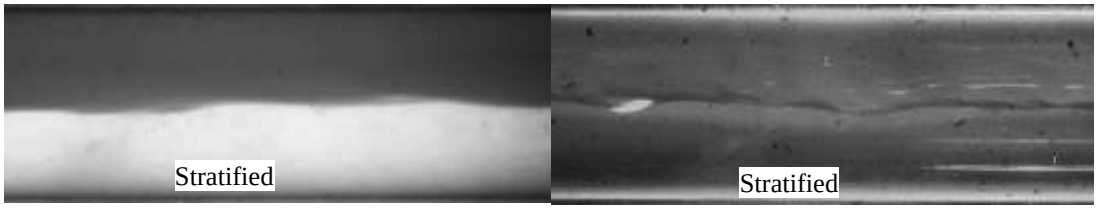

a) Umix = 0.62 m/s, r = 1

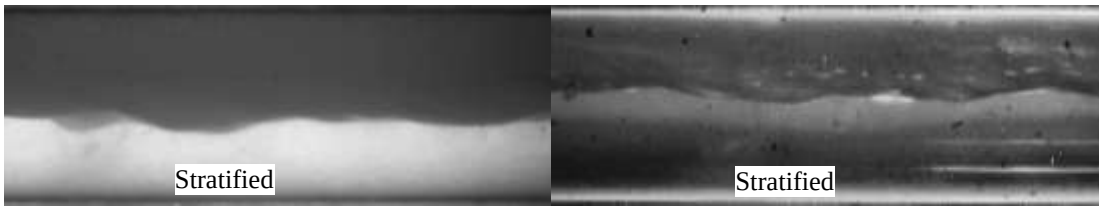

b) Umix = 0.78 m/s, r = 0.67

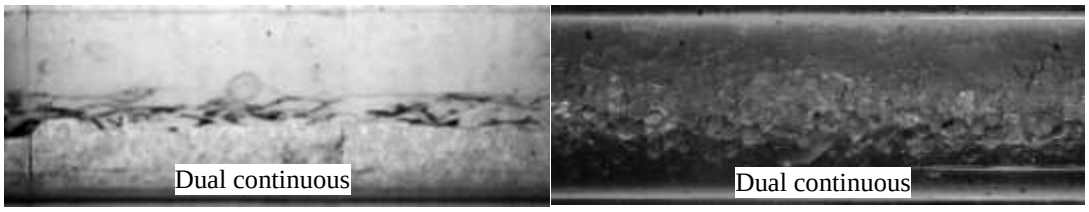

c) Umix = 1.86 m/s, r = 1

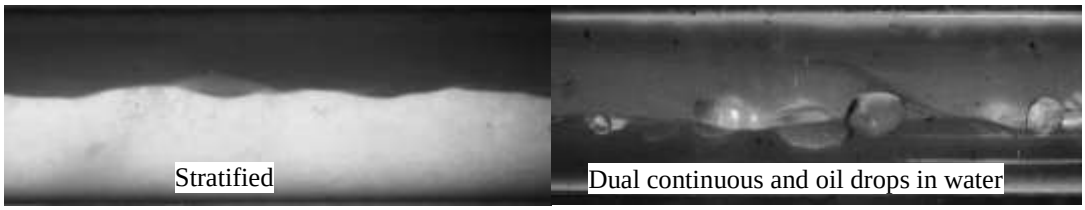

d) Umix = 0.78 m/s, r = 1.50

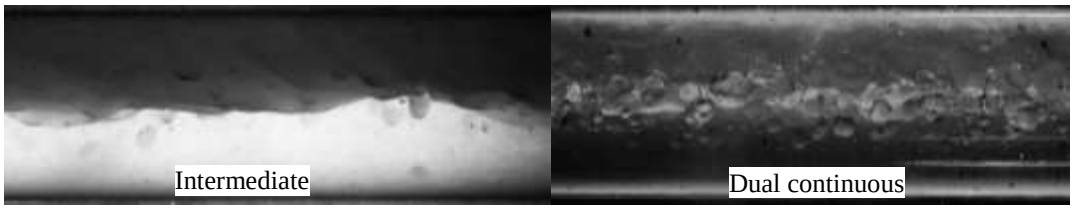

e) Umix = 1.71 m/s, r = 0.83

Figure 4.2 Flow patterns at 7m downstream the inlet without (left) and with (right) rod present

4.2.1 Average interface height

The average position of the interface, calculated from the images as discussed before, is plotted in Figure 4.3 for all flow conditions studied. As can be seen, the mean interface position gradually increased with distance away from the bluff body. This increase is almost linear and, on average, the change is approximately 3 mm at the furthest distance of 104 mm from the rod.

Specifically, the effect of mixture velocity on the average position of the interface is shown in Figure 4.4 for the same flowrate ratio. Interestingly, higher mixture velocities resulted in larger interface heights. In addition, the height increased with distance from the rod at a rate which increases with

mixture velocity. At 40 mm away from the rod, all three conditions have similar average interface height, (20.7, 21.1 and 22.1 mm) while at 104 mm away from the rod the average interface position has increased to 21.8, 23.8 and 25.5 mm respectively. The experimentally found interface heights at 40 mm downstream the rod were by an average of 1.3 mm higher than the interface heights found at a similar position when the rod was not present. For constant mixture velocity, the oil-to-water flowrate ratio affected the average interface height but did not affect significantly its rate of increase with distance from the rod (Figures 4.5a and b).

The increase in interface height agrees with previous studies by Duncan (1981) and Lin and Rockwell (1995) where a sharp elevation of the interface was observed behind a hydrofoil submerged in water. The elevation was found to increase with increasing Froude number in agreement with the effect of mixture velocity on interface height in the current study.

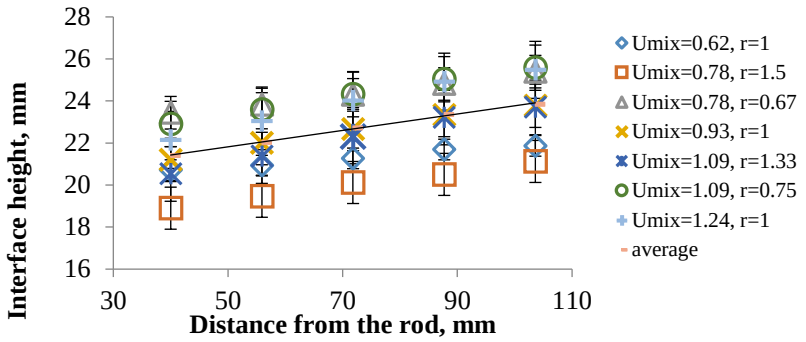

Figure 4.3 Average interface height at different distances behind the bluff body for all flow conditions investigated

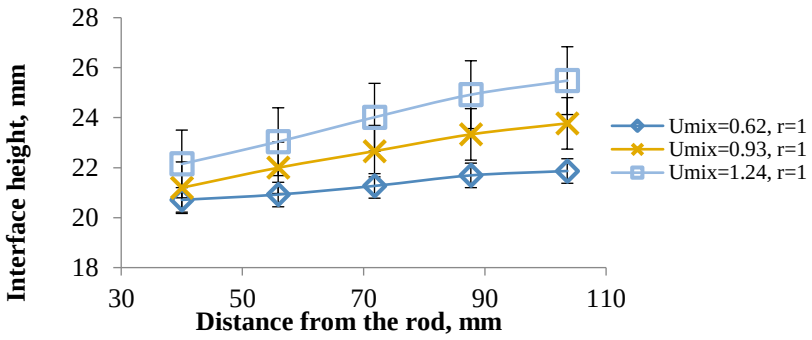

Figure 4.4 Effect of mixture velocity on interface height at different distances from the bluff body for r = 1

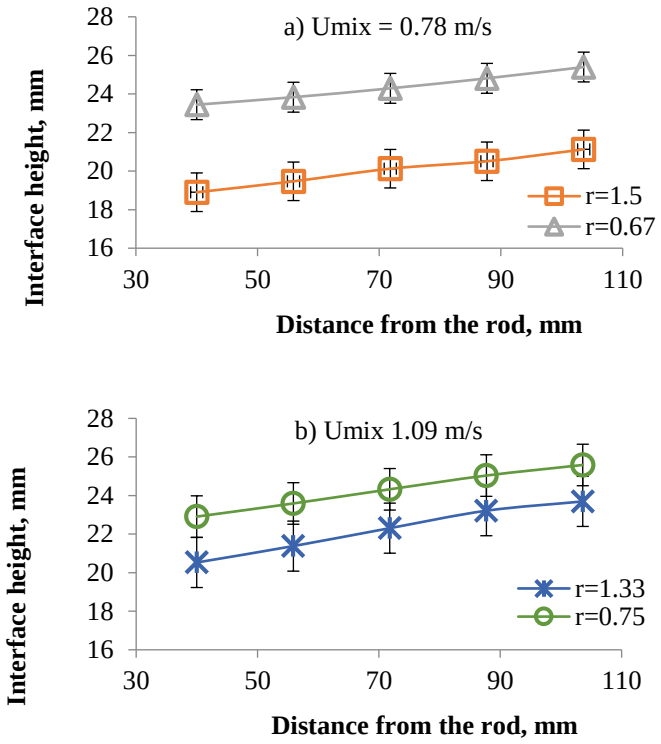

Figure 4.5 Effect of input flow rate ratio on interface height at different distances from the bluff body a) Umix = 0.78 m/s b) Umix 1.09 m/s

4.2.2 Average wave amplitude and wave length

Wave amplitudes downstream the bluff body increased initially until they reached a plateau at approximately 72 mm while they slightly decreased in some cases at 104 mm (Figure 4.6). Barral et al. (2015) observed the opposite trend where the wave amplitudes decreased with distance, but the waves in that work were generated by KH instabilities only. The oil to water flowrate ratio was found to affect the wave amplitudes and their development, as can be seen in Figures 4.7a and b. Larger wave amplitudes were obtained with the higher ratios. This is because at high r the interface height is low and close to the rod and can be more easily affected by the von Karman vortices shed by the bluff body within the water phase. Free surface distortions were also seen in previous studies (Sheridan et al., 1997; Reichl et al., 2005) at specific Froude number-depth of submergence ratios (Fr = 0.35 - 0.60 and h* = 0.40, Fr = 0.72 and h* = 2.0, 1.18). The current studies have depth of submergence ratios h* = 1.04 - 2.21 and high Froude numbers Fr = 2.57 - 5.12 which will further affect the interface (Dimas, 1998).

An increase in mixture velocity increased the wave amplitude at constant flowrate ratio (Figure 4.8). On average, for an increase in mixture velocity from 0.62 to 0.93 m/s, the wave amplitude increased by about 50% (between 1 mm and 1.5 mm) at all distances away from the rod. For an increase in mixture velocity from 0.93 to 1.24 m/s, the difference between the average wave amplitudes increased with distance from the rod, with almost no difference between 40 mm and 56 mm and a difference of 0.6 mm at 104 mm away from the rod. At high mixture velocities the interface height is slightly increased (Figure 4.4) and the interactions between the rod and the interface should be decreased. However, the increase in mixture velocity is accompanied by increased water phase velocity past the rod. This would

increase the magnitude of the von Karman vortices generated by the rod which affect the amplitude of the interfacial waves (Sheridan et al., 1997). Dimas (1998) also observed the change in the wave amplitude as Froude number increased and found that the shape of the free surface changed from sinusoidal to non-sinusoidal.

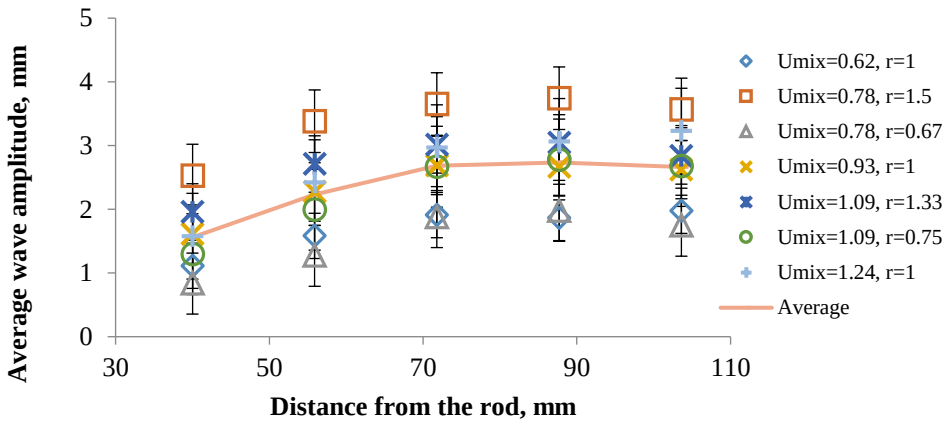

Figure 4.6 Average wave amplitudes at different distances from the bluff body for all flow conditions investigated

The average wavelengths did not vary significantly over distance until 72 mm away from the rod and then increased slightly further downstream by 0.5 mm on average (Figure 4.9). The change in wavelength over distance was less than 1 mm and the standard deviation was less than 3% for all flow conditions, apart from Umix = 0.78 m/s, r = 0.67, where the standard deviation was 6.5 % on average. In previous studies without a bluff body an increase in wavelength was accompanied by a decrease in wave amplitude (Trallero, 1995; Al-Wahaibi, 2006; Al-Wahaibi and Angeli, 2011; de Castro et al, 2012; Barral et al., 2015). In the current study, however, the wavelengths remained almost constant while the wave amplitudes increased with distance.

The results indicate a complex system. In case of unbounded flows, this system involves two main different types of instabilities. At the inlet, a single shear layer between the fluids leads to a convective instability (KH instability) while a double shear layer leads to an absolute instability (vortex shedding behind the wake of the cylinder; Huerre and Monkewitz, 1990). It is believed that the wave amplitude is increased as a result of the synergy between the two types of instabilities. However, the coupling of these instabilities is not well understood, particularly for wall bounded flows (Chaumaz, 2005 and Gondret et al., 1999) and would require further work.

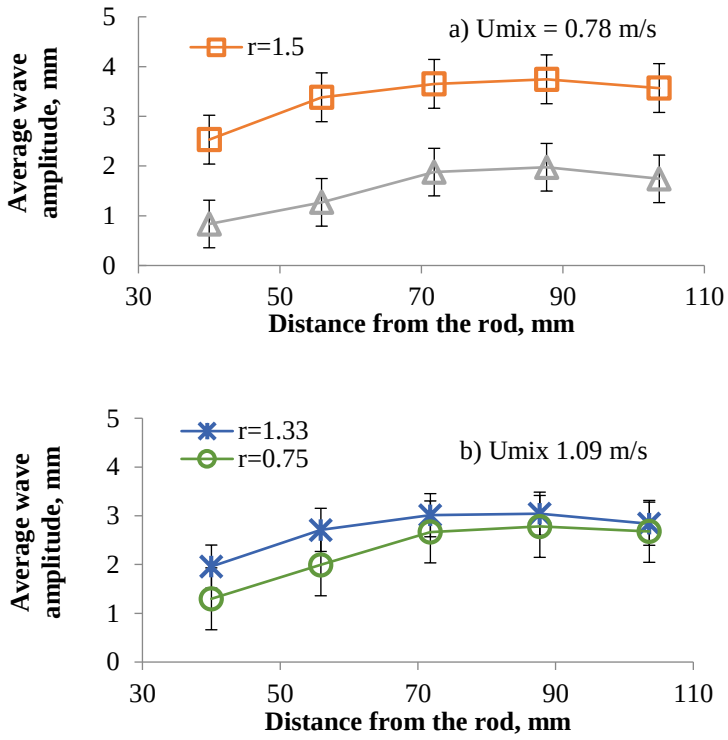

Figure 4.7 Effect of input flow rate ratio on average wave amplitudes at different distances from the bluff body. a) Umix = 0.78 m/s b) Umix 1.09 m/s

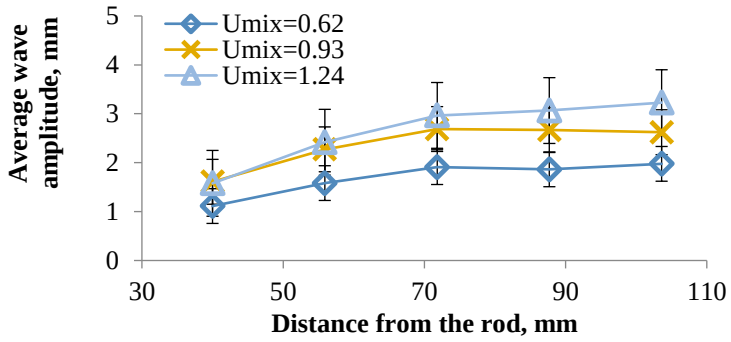

Figure 4.8 Effect of mixture velocity on average wave amplitudes at different distances from the bluff body for r=1

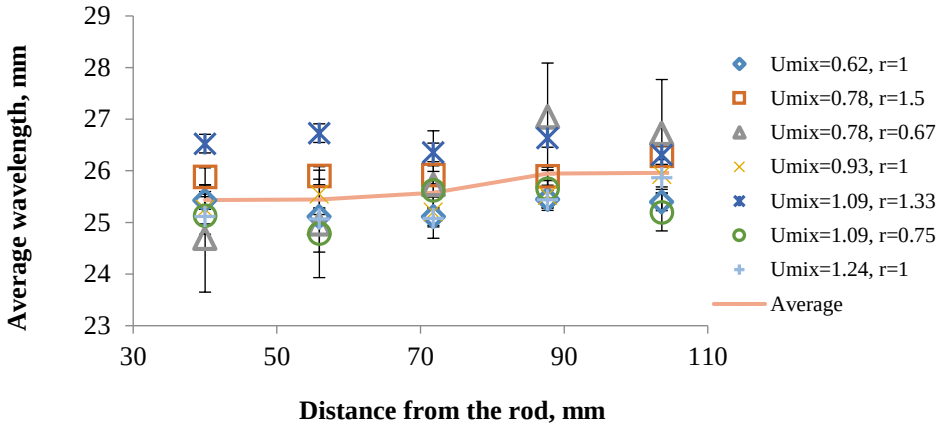

Figure 4.9 Average wavelength at different distances behind the bluff body for all flow conditions investigated

4.2.3 Average wave frequency

The average frequency of the waves generated behind the bluff body at different distances away from the rod is given in Figure 4.10. For all 7 conditions investigated, the wave frequencies did not vary significantly with distance. The small fluctuations in the values at the higher mixture velocities were less than 4%. The wave frequencies increased with increasing mixture velocity. The input ratio, however, did not have any significant effect as can be seen from the two cases of Umix = 0.78 and 1.09 m/s, where different input ratios were studied. The wave frequencies were also studied with the double-wired conductance probe for the few conditions where there were no drops present. There is good agreement with the results from the high speed imaging with frequency peaks at 26 Hz and 33 Hz for mixture velocities of 0.62 m/s and 0.78 m/s respectively.

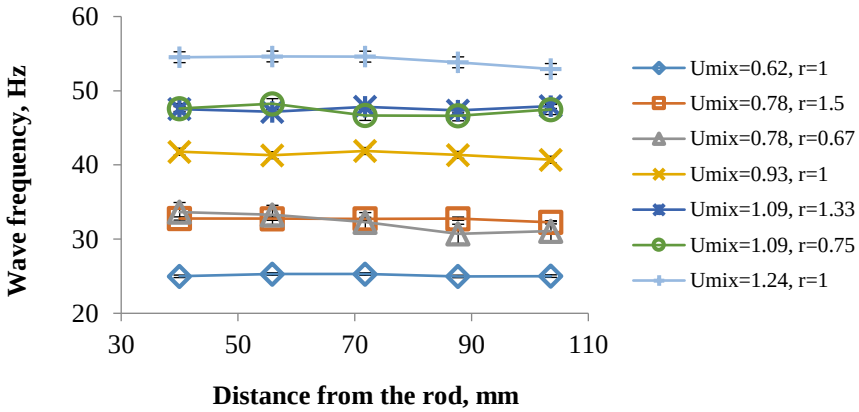

Figure 4.10 Average wave frequency at different distances behind the bluff body for all flow conditions investigated

From the measured wave frequencies the Strouhal number was calculated using the actual water velocity computed based on the average interface height. The mean value for the 7 flow conditions investigated was 0.24 with 9% standard deviation. This number is in good agreement with the literature

value of 0.2 for vortex shedding behind a cylinder in single phase unbounded flows. The agreement suggests that the interfacial waves are caused by the von Karman vortices generated by the rod. The agreement was good even for the cases where small KH waves formed at the inlet for r different than 1. It seems that, at least for the flow conditions studied, vortices generated by the rod dominated over the KH waves. In addition, the pipe wall does not affect the vortex frequencies. The distance between the rod and the pipe wall varies from 0 to 6.75 mm measured along the cylinder from the bottom of the pipe. It has been shown that vortices can be suppressed when the ratio of the distance between the wall and the cylinder over the size of the cylinder is smaller than 0.3 (Wang and Tan, 2008). For the current system only 9.8% of the length of the rod falls below this critical ratio. However, further investigations of the velocity fields would be required to fully understand the flow behind the bluff body in this configuration and its interactions with the interface.

4.2.4 Average wave velocity

Average wave velocities for the different conditions investigated are shown in Figure 4.11. The wave velocities increase with mixture velocity and do not vary significantly with distance from the rod especially at the lower mixture velocities. At the higher mixture velocities, there are more fluctuations with maximum deviation of about 4% from the mean value. In the current work, for all conditions investigated the wave velocities were 9.6% faster than the mixture velocity on average regardless of the input flowrates. Other studies (Barral et al., 2015; de Castro et al., 2012; de Castro and Rodriguez, 2015) also reported that the wave velocity was different from the mixture velocity. It is possible that these differences are due to the different mechanism of the generation of the waves; waves observed in previous studies resulted from a KH instability that depends on the velocity difference between the two phases at the inlet, whereas in the current study the waves seem to result predominantly from the vorticies shed by the bluff body. In addition, the blockage caused by the bluff body leads to a local acceleration of the fluid below and above the cylinder and it is possible that this affects the wave velocity.

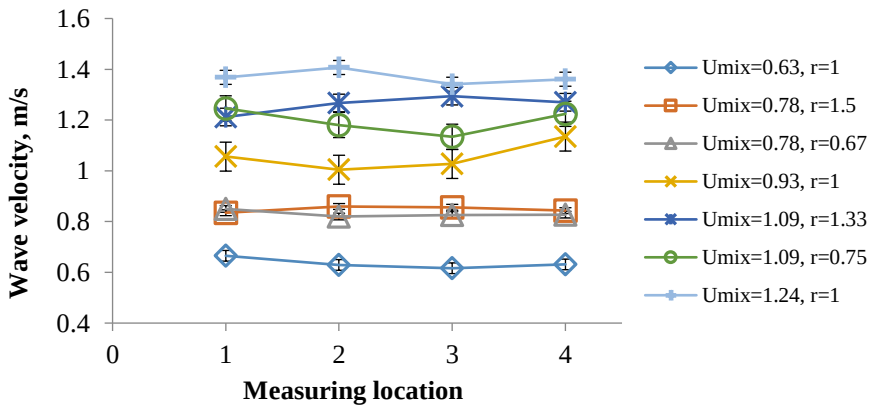

Figure 4.11 Average wave velocity at different distances behind the bluff body for all flow conditions investigated

4.3 Conclusions

In this chapter the effect of a cylindrical bluff body placed inside a pipe to the flow patterns and interface characteristics of a two-phase liquid-liquid system were studied experimentally, using high speed imaging and a conductance probe. The aim was to passively actuate waves in the interface and the transition from stratified to non-stratified flows. It was found that the rod reduced the transition to lower mixture velocities while the change in flow patterns persisted at 7 m downstream the rod. In stratified flows the bluff body generated interfacial waves attributed to the interactions of the von Karman vortices in the wake of the rod with the oil-water interface. An increase in interface height was seen after the rod that was affected by both the mixture velocity and the input ratio of the phase flowrates. The average wave amplitude increased with distance from the rod, while the average wavelength and frequency remained almost constant. The Strouhal number agreed with the literature value of 0.2 for vortex shedding behind a cylinder in single phase flows with no wall present. The wave velocities were found to be about 10% higher than the mixture velocity. Further investigations of the velocity fields in the water phase are conducted using the same flow system and the results are presented in the following Chapter of the Thesis revealing the interactions between the vortices shed by the rod and the liquid-liquid interface.

CHAPTER 5. FLOW STRUCTURES BEHIND THE CYLINDER

In this Chapter results from further investigations conducted on the first flow rig system using PIV is presented. In section 5.1 flow structures immediately downstream the cylinder in single phase flows are shown with discussions on the effect of the presence of the pipe wall. In section 5.2 the interaction between the vortices shed by the cylinder with the oil-water interface is presented and analysed. Conclusions are given in section 5.3. A summary of flow conditions investigated in this Chapter is given in Table 5.1 below.

Table 5.1 Summary of experimental conditions

	Flow rate (L/min) water	Flow rate (L/min) oil	Re_{pipe}	Re
Single phase experiments	20		11 471	1550
	25		14 338	1938
	30		17 206	2325
	35		20 074	2713
	40		22 941	3100
	45		25 809	3488
Two phase experiments	20	20	22 941	3100
	20	25	25808	3487
	20	30	28676	3875
	25	20	25808	3487
	25	25	28676	3875
	25	30	31544	4262

5.1 Single phase flow

Experiments were carried out initially to characterise the single phase flow features. Six different water velocities were considered, starting from the lowest velocity up to the mixture studied in the two phase

flows, corresponding to Reynolds numbers from 1555 to 3448. The Reynolds number has been computed based on the transverse cylinder diameter and corresponding velocity. The blockage ratio has been fixed at 0.13 which is below the critical value of 0.5 as previously discussed in Chapter 3. The gap ratio, γ however varies along the transverse direction and will decrease closer to the pipe wall along the transverse axis. The gap ratio becomes equal to 0.3 at z = ±13.8 mm. The curvature of the pipe along the transverse direction will still affect the flow behind the cylinder but it can be assumed that the gap will only become significant close to the pipe wall and would have a small effect on vortex shedding frequency in the observation plane in the middle of the pipe. In the PIV measurements it was possible to correlate successive images which suggests that the z-axis velocity component is weak enough so that the particle tracers remain in the observation plane (i.e. laser sheet) during the time of measurement.

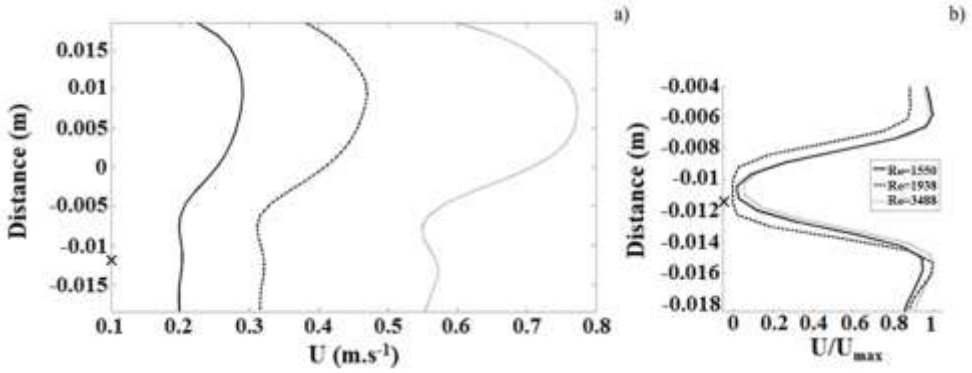

Figure 5.1 Time averaged axial velocity profiles in single phase flow. The velocity profiles have been averaged over axial distance a) from 3d to 14d and b) from 0 to 2d. The x indicates the position of the bottom of the rod

The introduction of the bluff body in single phase flow generates a shear zone in the wake of the cylinder. This is demonstrated in Figure 5.1 where the average velocity profiles in a vertical pipe diameter are shown. The shear zones shown in the different profiles generate the shedding of counter rotating vortices; this is in agreement with literature as the Reynolds numbers investigated are above the critical value (Re = 100) for vortex shedding (Zovatto and Pedrizzetti, 2001). The profiles however, exhibit different behaviour depending on the distance downstream the cylinder. Figure 5.1a shows the velocity profiles averaged over time and over the distance from 3d to 14d (i.e. 20 mm to 40 mm after the cylinder). The velocity is high at the upper part of the pipe and decreases as the cylinder is approached, before increasing again below the cylinder. The highest shear zones are located on the wall boundaries and on the top and the bottom part of the cylinder. The stratification in the velocity profile along the radial distance increases with the Reynolds number as expected.

The same velocity profiles normalised by the maximum velocity value, have also been plotted in the vicinity of the cylinder (0 to 2D or from 0 to 10 mm after the cylinder) in Figure 5.1b but for the lower part of the pipe. The velocity profile shapes are comparable to those reported by Wang and Tan (2008) for gap ratios above 0.4, even though these were obtained in a rectangular tank at different gap ratios and Reynolds numbers. In both cases the normalized velocity profiles are symmetric with maximum

values above and below the cylinder and a minimum value at location of the centre of the cylinder. Wang and Tang (2008) reported an asymmetry in the velocity profile in the vicinity of the cylinder for low gap ratios, which however, decreased with increasing ratio. The shapes of the velocity profiles, shown in Figure 5.1b, are independent of the Reynolds number and clearly show that they are similar in the two regions above and below the cylinder. It appears that the pipe geometry and the chosen gap ratio do not disturb the vortex generation mechanisms in the wake immediately downstream the cylinder.

For a better visualization of the spatial stratification of the velocity in the central plane of the pipe, time averaged axial velocity fields normalized by the corresponding U_{mix} are shown in Figure 5.2 for two different Reynolds numbers. The flow features do not change within the range of Reynolds numbers investigated while the velocity stratification is more pronounced at the high Reynolds number. Three different regions in the wake of the cylinder can be defined. The first one, located between axial distances 0 and 2D (from 0 to 10 mm after the cylinder) corresponds to the velocity profiles shown in Figure 5.1b. This region exhibits two high magnitude time averaged velocity lobes located on the top and the bottom of the cylinder. These lobes show a high degree of symmetry along the radial direction but not along the axial one. Indeed, the high magnitude velocity lobe located on the bottom of the cylinder seems to be more elongated along the direction of the flow. In this region, the shear flow exhibits the initial mechanism of counter vortex generation. The extended bottom velocity lobe indicates that the vortex street will be slightly shifted to the top of the pipe. At axial distances between 2D to 6D (from 10 to 30 mm after the cylinder), the second transitional region occurs. The time averaged axial velocity lobe located on the bottom of the cylinder tends to decrease along the direction of the flow. The third region appears at axial distances greater than 6D. In this region, the flow is divided in two parts, a low velocity magnitude one at the lower part of the pipe and a high velocity magnitude one at the upper part of the pipe, above the cylinder. In this region, far from the cylinder, the large scale vortices are advected along the flow direction. The lower mean velocity magnitude area corresponds to the zone in which the vortices are travelling; indeed the recirculation of the vortices decreases the time averaged velocity magnitude. As can be seen, in the third region the isocontours of the time averaged axial velocity field are not parallel to the flow but slightly inclined to the upper part of the cylinder indicating that the vortex street is shifted to the top of the pipe.

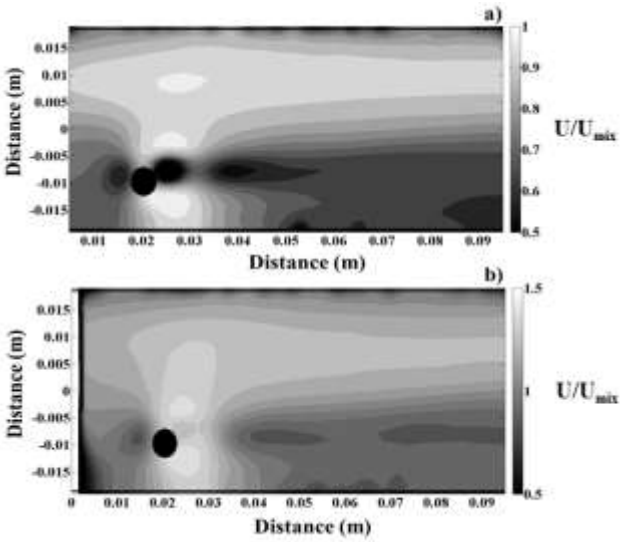

Figure 5.2 Time averaged axial velocity map for single phase flow and Reynolds numbers a) 1550 and b) 3488. The axial velocity has been normalized by the corresponding Umix

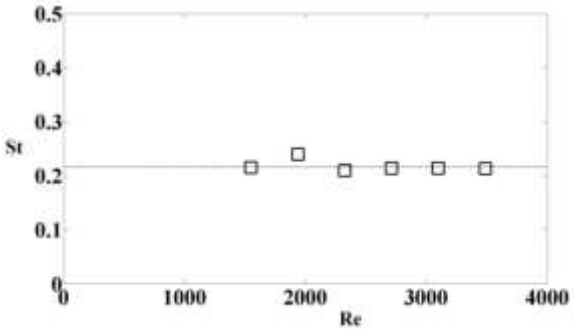

Figure 5.3 Strouhal number plotted against Reynolds number in single phase flow. The linear fit shows a constant value St=0.216 ± 0.010)

The vortex shedding frequency, f, is generally studied by computing the non-dimensional Strouhal number (Eq. 2.6). The variation of the Strouhal number with Reynolds number is shown in Figure 5.3. The different frequencies have been computed by plotting the FFT of the radial velocity component fluctuations at a distance 8d downstream the cylinder and at the same height as the centre of the transverse cylinder. The Strouhal number does not vary significantly in the range of the investigated Reynolds numbers and is approximately equal to 0.21 which is similar to values reported in the literature for unbounded flows. The presence of the pipe wall underneath the cylinder clearly does not affect the vortex shedding frequency for the gap ratios investigated. This is in agreement with studies in rectangular channels (Wan and Tan, 2008) for similar Reynolds numbers.

To evaluate the effect of the wall on the vortical structures behind the cylinder the spanwise vorticity component was calculated as follows:

$$\omega_z = \frac{\partial V}{\partial x} - \frac{\partial U}{\partial y} \qquad \text{Eq. (5.1)}$$

where U and V represent respectively the horizontal and the vertical velocity components. Figure 5.4 shows the time averaged spanwise vorticity component for two different Reynolds numbers. The main vorticity structures appear, as expected, on the top and the bottom of the cylinder. Increasing the Reynolds number tends to decrease the size of the two vorticity lobes, while a reattachment on the cylinder base of these two lobes is also seen. The corresponding Reynolds stresses are also plotted in Figure 5.5. The Reynolds stresses are computed from the product u'v'. The velocity fluctuations are found from $u' = U - U_m$ and $v' = V - V_m$ where U_m and V_m are respectively the time averaged horizontal and vertical velocity components. The Reynolds stresses are localised on the wake of the cylinder and concentrate in two opposite regions. The positive region is at the low part of the flow while the negative region is at the top. The results are qualitatively comparable to those obtained in rectangular channels. The pattern is almost symmetric at the low Re. In addition, at this Re two small clusters of Reynolds stresses appear upstream the main clusters with opposite signs to them (Figure 5.5a). The pattern becomes less symmetric as Re increases (Figure 5.5b). The positive Reynolds stress region becomes more predominant and tends to shift the low Reynolds stress region to the top of the pipe. The shear layer at the bottom wall interacts with the positive lobe of the Reynolds stresses and pushes the clusters of u'v' to the upper part of the pipe. These results, consistent with the time averaged velocity field maps displayed in Figure 3, indicate that the vortex street is shifted to the top of the pipe with increasing Reynolds number. In previous studies the loss of symmetry in Reynolds stresses occurred with decreasing gap ratio (Wang and Tan, 2008). It should be mentioned that the results shown in Figures 5.4 and 5.5 were obtained by increasing the spatial resolution of the high speed PIV images. To capture the vortical flow structures very near the cylinder, the spatial resolution needs to be high. This is possible since the velocity magnitude in the direct wake of the cylinder is lower than in the rest of the pipe, e.g. the velocity in the upper part of the pipe can be two times higher than in the wake of the cylinder (see Figure 5.1).

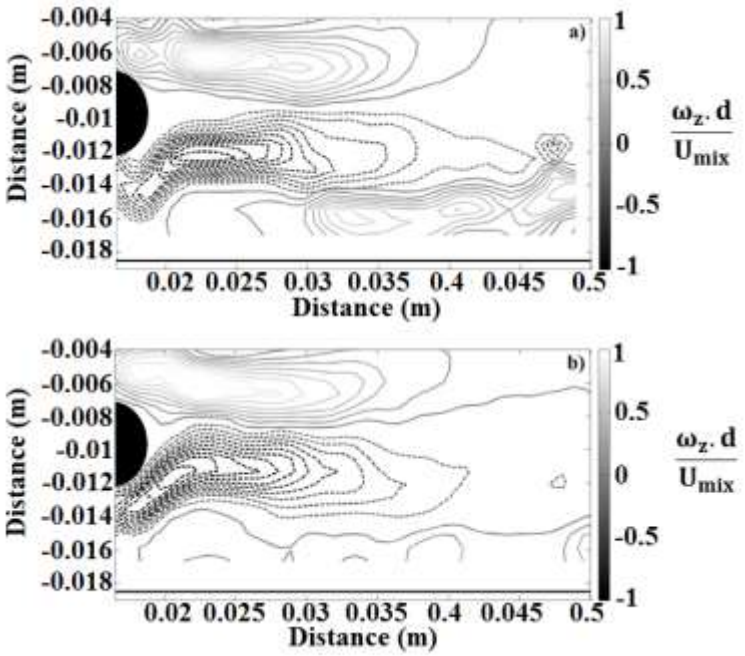

Figure 5.4 Time averaged spanwise vorticity over distance from cylinder for a) Re= 1550 and b) Re= 3488. The solid lines correspond to positive regions while the dashed lines correspond to negative regions

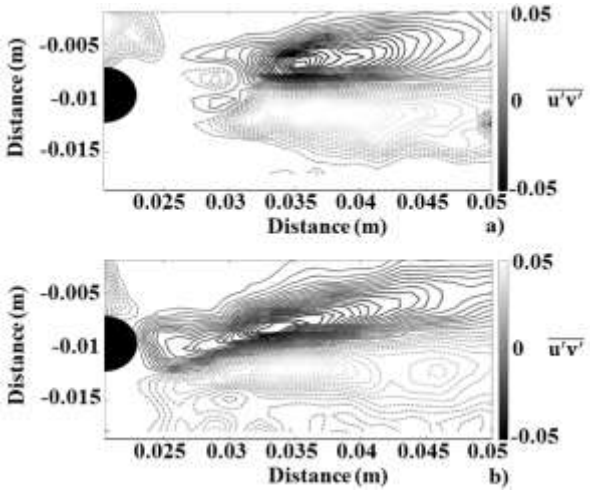

Figure 5.5 Time averaged Reynolds stresses over distance from cylinder for a) Re=1550 and b) Re=3488. The solid lines correspond to the negative region while the dashed lines correspond to the positive region

The vorticity calculated from equation 5 contains the effects of both shear action and swirling (Zovatto and Pedrizetti, 2001). The shear layers corresponding to the bottom part of the pipe and the wake of the cylinder represent the main vorticity regions but do not necessarily generate vortices. Indeed, vorticity due to shear stresses can fail to track vortex structures. Vortex tracking has been discussed previously by Jeong and Hussain (1995) who proposed the parameter λ_2 (Eq. 5.2) to discriminate the shearing and the swirling regions of vorticity.

$$\lambda_2 = \left(\frac{\partial U}{\partial x} + \frac{\partial V}{\partial y}\right)^2 - 4\left(\frac{\partial U}{\partial x}\frac{\partial V}{\partial y} - \frac{\partial U}{\partial y}\frac{\partial V}{\partial x}\right) \qquad \text{(Eq. 5.2)}$$

For vorticity generated by shearing action, λ_2 is positive, while for vorticity generated by swirling, λ_2 is negative. Figure 5.6 shows the time sequence of λ_2 for the two Reynolds numbers shown in the previous figures with the corresponding velocity fields superimposed. The time delay between each image is 20 ms for Re=1550 (Figure 5.6a) and 10 ms for Re=3488 (Figure 5.6b). As can be seen at these conditions the value of λ_2 above the pipe centre line is zero while the flow field downstream of the cylinder at horizontal level to that of the cylinder is mainly positive with small areas of negative regions. The negative regions represent the vortices generated by the cylinder and these are advected downstream with the bulk flow. In both cases, it appears the lower pipe wall shifts the vorticity regions to the top. This is more pronounced for the high Re (Figure 5.6b) where at distance 14D (i.e. 70 mm) downstream the cylinder, the negative regions can reach upto the centre of the pipe, while at low Re they do not reach the pipe centre. Further analysis on the identification of the vortices using the λ_2 and quantitative measure of the vortices are given in the next Chapter (Chapter 6). The single phase flow studies indicate that the 3D pipe geometry does not affect significantly the flow features behind the cylinder in the central plane of the pipe, compared to the previous experimental studies in rectangular channels. In addition, the bottom pipe wall clearly interacts with the flow in the wake of the cylinder.

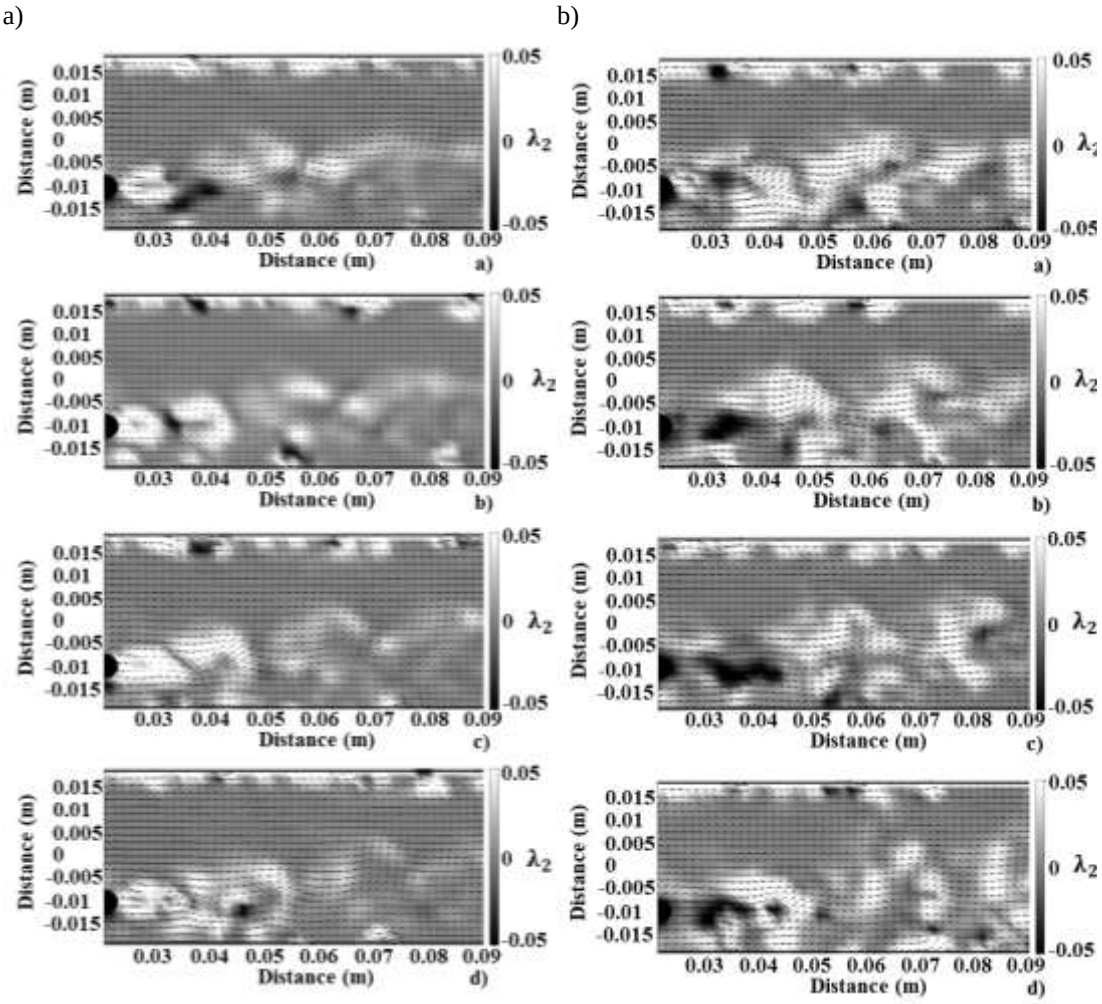

Figure 5.6 Change of parameter λ_2 over time with velocity fields superimposed. a) Re=1550 and the time delay between each image is 20 ms. b) Re=3488 and the time delay between each image is 10 ms

5.2 Two phase flow

In the two-phase flow cases it is important to capture the interface shape. Previously, for cases when the refractive index between the two liquid phases was matched, a very small quantity of fluorescent particles was injected close to the interface, which made the interface to appear as a bright line (Mohamed-Kassim and Longmire, 2004). In another approach, used in gas-liquid flows, a second camera, slightly inclined to the horizontal direction of the flow and simultaneously triggered with the PIV camera, was used to capture the shape of the waves (Birvalski et al., 2014). In the present study, the interface was detected from the signal of the seed particles in the water phase. The signal of the particles was increased and blurred and the contour of the seeded phase was then obtained by binarising the image obtained. To remove any optical artefacts near the interface due to reflections or the presence of any droplets, the binary image was eroded by following a 9-pixel connectivity criterion (Chinaud et al., 2015).

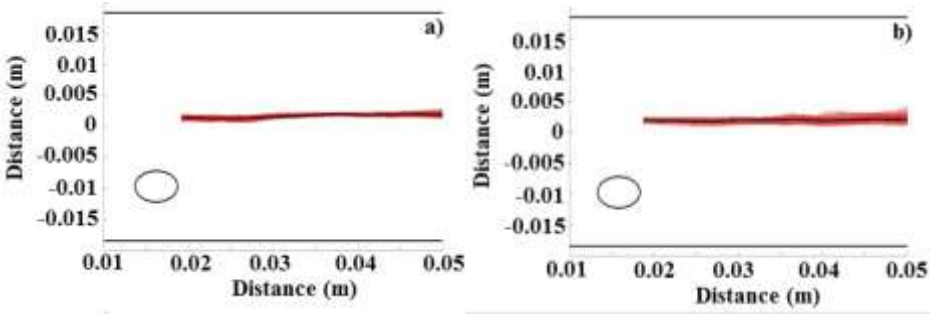

Figure 5.7 Interface shape for r = 1. a) Fr = 1.4, b) Fr = 1.8. The time averaged interface shape (solid thick line) has been superimposed to 200 interface shapes obtained over time (solid thin lines)

The two-phase flow PIV measurements were carried out in stratified and stratified wavy flows characterised by linear waves. Both the effect of Froude number and cylinder submergence (which depends on the ratio of the flowrates) were investigated. The Froude number varied from 1.4 to 1.8 (based on mixture velocity), which correspond to oil/water flow rates from 20 to 30 L min^{-1}. The effect of the Froude number on wave motion can be seen in Figure 5.7 for equal phase flow rates (r = 1) for two cases, Fr = 1.4 and 1.8. The time averaged interface shape has been superimposed as a dark line on the 200 interface shapes obtained over time. In both cases, the time averaged interface shape is almost flat. The interface height for these flow conditions is expected to be in the middle of the pipe when no cylinder is present (Barral and Angeli, 2013). The difference in the interface height from the middle position is attributed to the hydraulic jump induced by the cylinder. As can be seen, the interface fluctuations increase with the Froude number. From the interface shapes over time the velocities of the waves can be obtained with cross correlation. It was found that the wave velocities were lower than the mixture velocity, U_{mix}. For the cases shown in Figure 5.7 the wave velocities are around 0.42 m/s for Fr = 1.4 and 0.69 m/s for Fr = 1.8 while the U_{mix} are 0.62 m/s and 0.77 m/s respectively. The frequencies of the waves, obtained with FFT computation, were found to be around 18 Hz (for Fr = 1.4) and 35 Hz (for Fr = 1.8) which give a Strouhal number of about 0.2, the values expected for vortices shed by unbounded cylinders in single phase flows. It should be noted that the FFT resolution is not very high because the high sampling frequency of the camera (between 750 and 1500 Hz) allows measurements for a short time when, depending on the frequency, from 200 to 1000 images can be collected.

The effect on wave motion of the depth of the cylinder submergence below the interface can be seen in Figure 5.8 for two symmetric cases, Q_o = 30 L min^{-1} and Q_w = 20 L min^{-1} (r = 1.5, Figure 5.8a) and Q_o = 20 L min^{-1} and Q_w = 30 L min^{-1} (r = 0.66, Figure 10b) and Froude numbers equal to 1.8. For oil-to-water flowrate ratio r = 1.5 (Figure 10a), the time averaged interface shape is centred just below the middle plane of the pipe. The wave amplitudes grow significantly downstream the bluff body. At a distance corresponding to 8D (40 mm from the cylinder) the amplitude has reached the highest value observed in this study, equal to ± 5 mm. For flow rate ratio above one (Figure 5.8b), the mean position of the time averaged interface shape is above the middle of the pipe and the amplitude of the waves is less. The presence of the bluff body tends to increase the mean interface height compared to flows

without the cylinder. Wave velocities and frequencies are similar however, in both cases. The computed velocities are 0.8 m/s for r = 1.5 and 0.77 m/s for r = 0.66, while in both cases the main FFT peak is at 29 Hz, which gives a Strouhal number equal to 0.2. In the range of flowrates investigated, the effect of bluff body submergence on wave generation is more pronounced than that of Froude number.

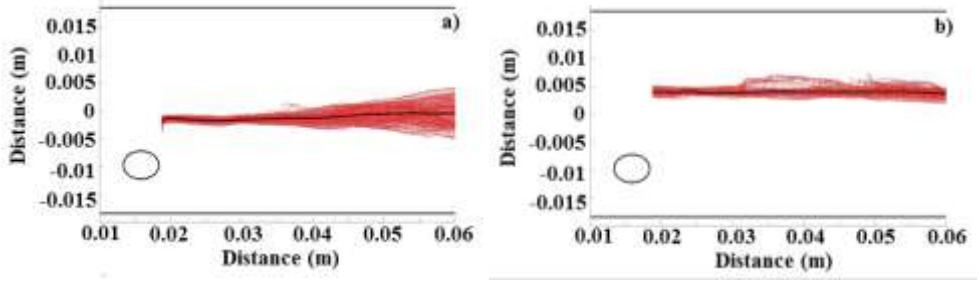

Figure 5.8 Interface shape for Fr = 1.8. a) r = 1.5 and b) r = 0.66. The time averaged interface shape (solid thick line) has been superimposed to 200 interface shapes obtained over time (solid thin lines)

The wave frequencies were compared with the frequencies of von Karman vortices downstream the cylinder, which were calculated from the FFT of the fluctuations of the vertical velocity component. The results showed that these frequencies matched and the von Karman vortices appear to "print their frequency on the interface. Velocity fields are presented below for indicative cases to further how the vortices interact with the interface.

The evolution of the velocity fields over time is shown in Figures 11 and 12 for the flowrate combinations Q_o=30 L min^{-1}, Q_w=20 L min^{-1} (r = 1.5, Fr = 1.8) and Q_o=20 L min^{-1}, Q_w= 20 L min^{-1} (r = 1, Fr = 1.4) respectively. These two cases correspond to the most pronounced wave actuation and to an almost flat interface. For both figures the time difference between images is 6.7 ms. To observe the recirculation patterns in the water phase the velocity of the wave has been subtracted from the water phase axial velocity component. As can be seen in Figure 5.9, the vortices generated on the top of the cylinder are directly in contact with the interface and actuate it by increasing the amplitude of the waves. The shear layer generated at the bottom boundary of the pipe, as shown in single phase flow (see previous section), seems to advect the vorticity structures to the top of the pipe. The recirculation cores generated at the top and the bottom of the cylinder are both advected in the pipe along the flow direction. The top recirculation core is attached to the interface as soon as it is generated, while the bottom one is quickly advected upwards before reaching the height of the transverse cylinder. The top recirculation core corresponds to the crest of the generated wave, while the bottom one corresponds to the wave trough. In this particular case, the velocity of advection of the vortical structures is the same as the wave velocity.

a) Qo=30 L.min^{-1} and Qw=20 L.min^{-1} (r=1.5, Fr=1.8)

b) Qo=20 L.min^{-1} and Qw=20 L.min^{-1} (r=1, Fr=1.4).

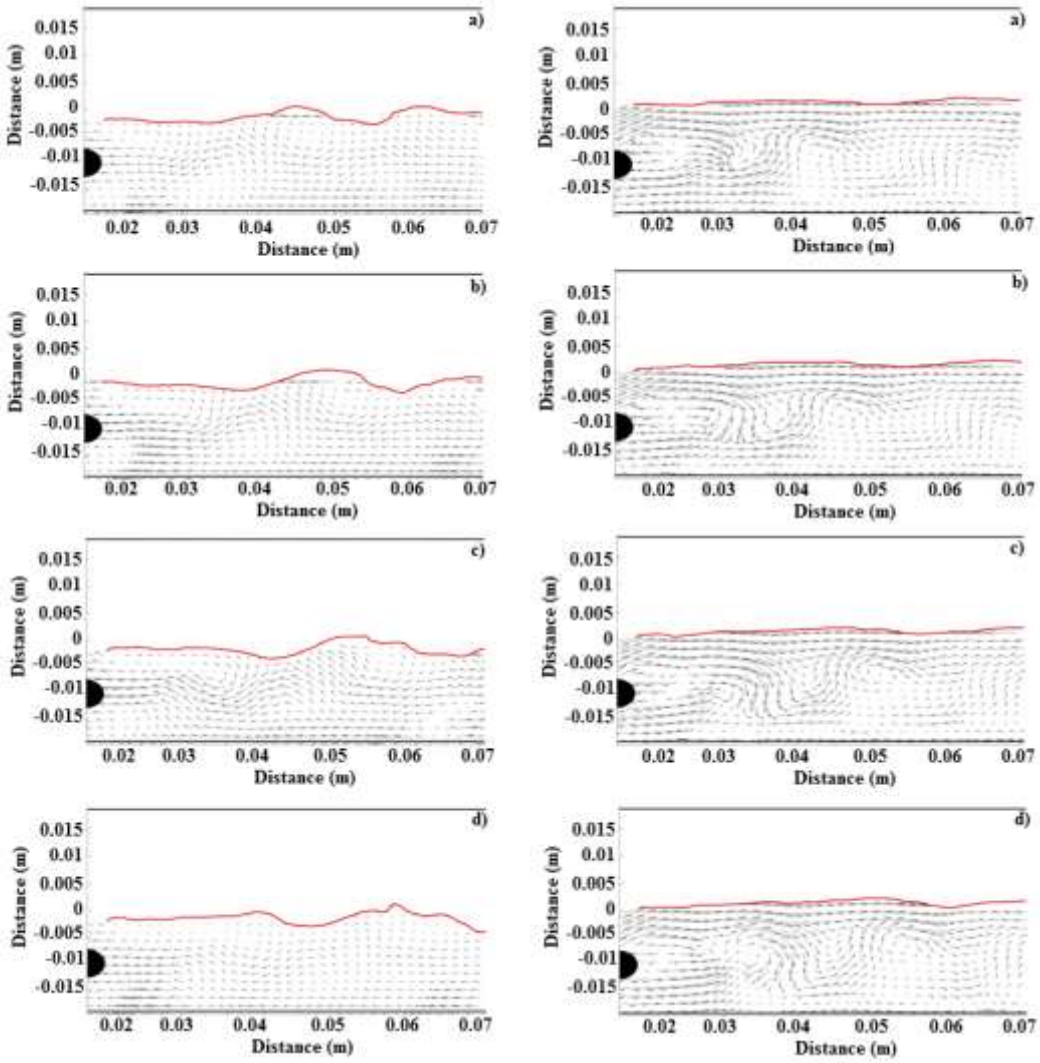

Figure 5.9 Time sequence of the velocity field after the cylinder a) with the mean wave velocity (0.8 m/s) subtracted. The time delay between images is 6.7 ms. b) with the mean wave velocity (0.4 m/s) subtracted. The time delay between images is 6.7 ms

In the case of r = 1 (Figure 5.9b) recirculation cores still appear in the water phase downstream the cylinder but the interface remains almost flat. In this case, the recirculation cores tend to stay at the same horizontal level as the cylinder and are not advected towards the interface, while a jet like flow appears on top of the cylinder. The velocity computed from the cross correlation of the interface is equal to 0.42 m/s. The magnitude of velocities above and below the cylinder is higher than the wave velocity. In addition, the area occupied by the recirculation zone in the wake of the cylinder is larger than in the case shown in Figure 5.9a. Similar results were found for the other flow rate combinations studied where r = 1.

In the cases considered here, the transitional regime defined by Sheridan et al. (1997), which is characterized by an oscillation of the jet like flow adjacent to the base of the cylinder, was not observed.

The Froude numbers used here, however, as well as the depths of submergence are different, while the flow is bound by the pipe wall. The vorticity field, calculated from Equation 5.1, for the case Qo=30 L min^{-1} and Qw=20 L min^{-1} (r = 1.5, Fr = 1.8) is shown in Figure 5.10, where the black regions represent negative vorticity and the white regions positive vorticity. The positive vorticity cluster is localised above the cylinder and the negative one below the cylinder. These two vorticity clusters correspond to the counter rotating vortices in the wake of the cylinder. A negative vorticity cluster appears directly attached to the interface (circled in Figure 5.10) and seems to be in phase with the negative vorticity at the wake emitted from the bottom of the cylinder. This negative vorticity cluster attached to the interface is then advected along the pipe underneath the crest of the generated wave. From the flow field measurements, it appears clearly that interfacial waves are actuated by the von Karman vortices while two cases can be distinguished. For low mean interface height (high flow rate ratio), the vortices attached directly to the interface and wave amplitude is increased. For high mean interface height, a jet like flow appeared on the top of the cylinder while the amplitude of the actuated waves were small.

As previously discussed in section 5.2, the PIV experiments were carried out for the cases where the waves were linear and the interface was not very distorted. To further evaluate the effect of the cylinder on the actuation of drop formation, the two-phase flow patterns were observed with high speed imaging with and without the transverse cylinder. These studies were carried out both in the vicinity of the cylinder and at 7 m downstream. Droplet detachment was also observed as can be seen in Figure 5.11. However, 3D effects may still be present but cannot be quantified from these measurements.

Two mechanisms of drop generation were seen. In the first mechanism, interfacial waves are actuated by the von Karman structures shed by the cylinder and drops detach from these non-linear waves (Figure 5.11a). The shear in the vorticity structures close to the waves elongates the wave crests to ligaments from where the drops detach. This mechanism of droplet generation occurs when the Froude number is high or the submergence depth is low. Drops are also generated when the interface directly hits the cylinder (Figure 5.11b) at low depths of submergence. In this case, the interface follows the large scale structures after the cylinder and remains encapsulated at the von Karman vortex street. The small vorticity structures distort locally the interface and generate the droplets. Detailed mechanism of drop detachments from ligaments is further discussed in Chapter 7.

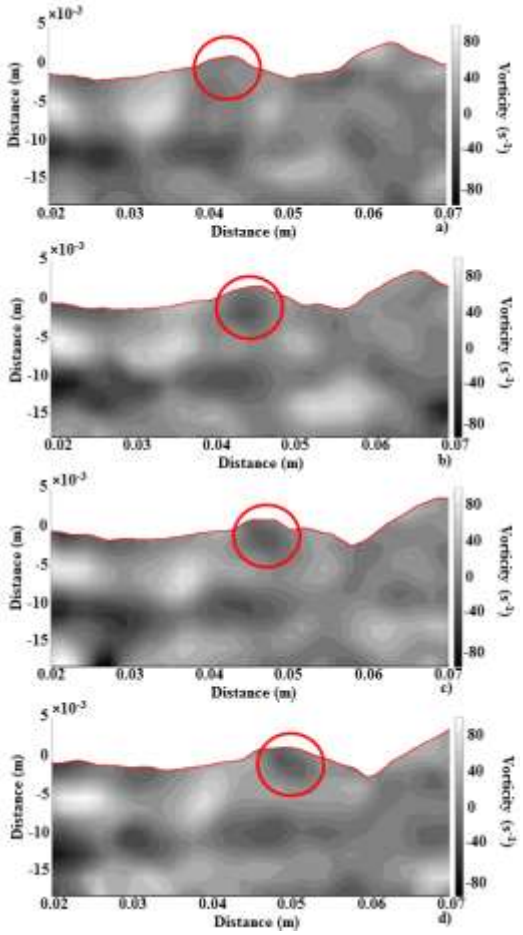

Figure 5.10 Time sequence of the vorticity field after the cylinder for Qo=30 L.min^{-1} and Qw=20 L.min^{-1} (r=1.5, Fr=1.8). The time delay between images is 6.7 ms. The circles show the negative vorticity cluster attached to the interface

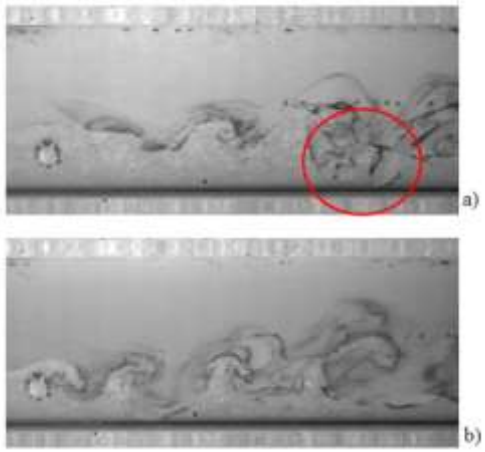

Figure 5.11 Droplet generation. a) Umix=0.93 m/s and r=2 and b) Umix=1.09 m/s and r=2.5. The circle in a) indicates the position of the ligament which will lead to droplet detachment

The flow pattern map recorded at 7 m downstream the test section inlet previously shown in Chapter 4 is shown in Figure 5.12, where the symbols represent the patterns with the cylinder present and the dashed line indicates the pattern transitions without the cylinder. The decrease in the depth of

submergence corresponds to a move to the right hand side of the map while an increase in the Froude number corresponds to a move towards the top of the flow pattern map. The shift of the right hand boundary between SW and DC flow is therefore attributed to the effect of the von Karman structures on the interface and corresponds to the regime observed in Figure 5.11a. The three cases with r > 2.5 represent droplet generation by direct impact of the interface on the cylinder. The PIV measurements were carried out for the cases in the stratified flow region (square points on Figure 5.12). The left hand side boundary is shifted with the cylinder to low mixture velocities, which indicates that the mixture velocity (or Froude number) also plays a role on drop generation.

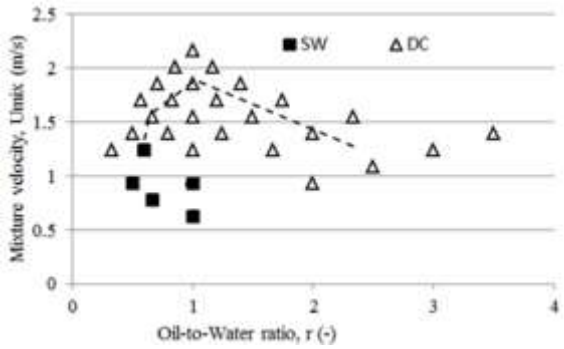

Figure 5.12 Flow pattern map (symbols) with the cylinder, 7 m downstream the inlet. The dashed line corresponds to the boundary between stratified wavy (SW) and dual continuous (DC) patterns without the cylinder

At r = 1, droplets are generated at low mixture velocities (low Froude numbers) in contrast to what is shown in Figure 5.9a. In this particular case, a jet-like flow appeared between the upper part of the cylinder and the interface, while there were no vortices attached to the interface. It was shown by Sheridan et al. (1997) that this type of flow behind the cylinder can also generate waves at the interface. It can be assumed that as the mixture velocity increases for constant flow rate ratio, the interface becomes progressively more disturbed and drops finally detach.

The cylinder can be considered as a hydrodynamic oscillator. For the range of investigated Reynolds numbers the global hydrodynamic instability generated at the wake of the cylinder prints the vortex shedding frequency to the interface. For the conditions studied this mechanism prevails over the frequencies generated at the interface at the inlet by the convective hydrodynamic instability between two fluids with different flow rates. In the current work where the cylinder diameter is constant, the actuation frequency was varied by changing the mixture velocity and the flow rate ratio. However, the results indicate a complex system. At least, in case of unbounded flows, this system involves two main different types of instabilities. At the inlet, a single shear layer between the fluids leads to a convective instability (KH instability) while a double shear layer leads to an absolute instability (vortex shedding behind the wake of the cylinder). It is believed that the wave amplitude is increased as a result of the synergy between the two types of instabilities. However, the coupling of these instabilities is not well understood, particularly for wall bounded flows and would require further work.

5.3 Conclusions

In this chapter, the main objective was to investigate the interactions of the wakes generated by a transverse cylinder submerged in water, with the interface in a stratified oil-water pipe flow and to actuate the transition to dispersed patterns. Velocity fields were obtained with high speed PIV in the vicinity of the cylinder. The results in single phase flow showed that the flow fields were comparable to those obtained in rectangular channels under 2D flow conditions. In two-phase flows the presence of the cylinder generated waves in the oil-water interface for high Froude numbers and low depths of cylinder submergence. The results revealed that for low depths of submergence, vorticity clusters attach to the interface and generate interfacial waves. By increasing the Froude number (i.e. the mixture velocity) these waves become increasingly non-linear. However, in two-phase flows only a limited number of flow conditions were investigated due to the mismatch of the refractive indices between the two test fluids. Further investigations on the interaction between the cylinder on both single and two phase flows are carried out in the following two chapters.

CHAPTER 6. ANALYSIS VIA SIMULTANEOUS PIV / PLIF

In this Chapter results obtained from the application of the simultaneous PIV and PLIF techniques on the second flow facility (System 2) with test fluids that have matched refractive indices are presented and discussed. In section 6.1 the effect of the confined geometry on the vortex shedding characteristics and the general flow behaviour immediately downstream of the cylinder is investigated in single phase water flows. For two phase flows, in comparison to the results presented in the previous Chapter, a more detailed and in-depth analysis is performed on the interaction between the cylinder and the oil-water interface. Description of the flow patterns observed and the flow pattern map for the system with and without the bluff body is given in section 6.2. In addition, results on the analysis of the flow immediately downstream of the cylinder is discussed especially focusing on the effect of the two key parameters, h* and Fr, on the flow structures such as the strength and trajectories of the vortices, as well as the wave characteristics such as the frequency and amplitude. Lastly conclusions are given in section 6.4.

6.1 Single phase flow

Studies were initially carried out in single phase water flows for a range of flowrates to determine the effects of the confined geometries on the vortex shedding characteristics of the bluff body. For this purpose a total of 5 flow conditions were studied in the presence of the bluff body. The corresponding Reynolds numbers varied between 58 and 203. Velocity profiles and vortex shedding frequencies were obtained via PIV. In the PIV measurements it was possible to correlate the movement of the particles which suggests that the z-axis velocity component is weak and the particles stay within the laser sheet (with thickness < 1 mm). The smallest Reynolds number investigated is above the critical Reynolds number, Re_{crit} = 47, for vortex shedding behind a cylinder in an unconfined flow (Williamson 1995). However, in the current study it was found that the critical Reynolds number for vortex shedding was delayed beyond Re = 73 and periodic shedding was observed at Re = 118 which indicates that the transition from steady to unsteady flow occurs for Re between 73 and 118. Similar increased critical Re have been reported by Zovatto and Pedrizzetti (2001) and Sahin and Owens (2004) for cylinders bounded between two parallel walls. Zovatto and Pedrizzetti (2001) suggested that this shift in the critical Re to higher values compared to the unconfined case is possibly due to the local acceleration of the fluid between the cylinder and the wall.

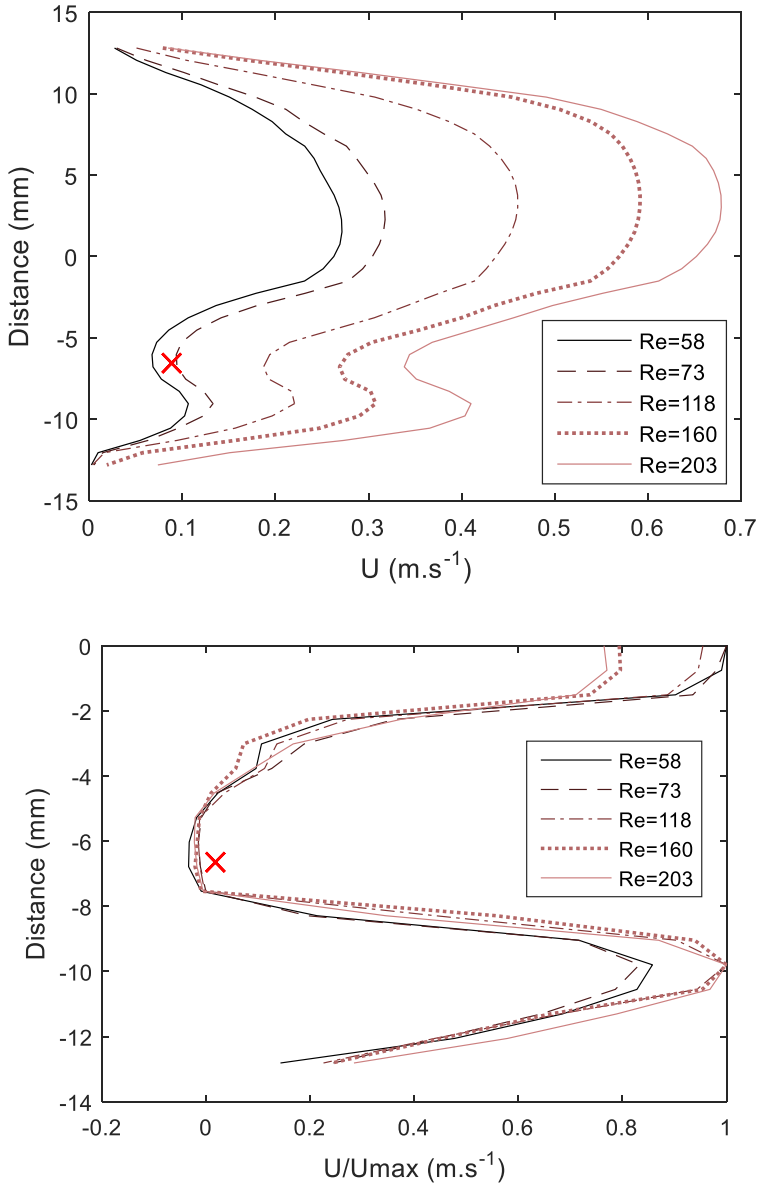

Figure 6.1 a) Time averaged axial velocity profiles for single phase water flow in the pipe after the cylinder for different Reynolds numbers. The profiles have been spatially averaged over axial distances between 2D-14D. The central position of the cylinder is indicated using the red-cross. Flow is in steady-state for Re = 58 and 73. b) Time averaged axial velocity profiles for single phase water flow at 0.5D downstream the cylinder. The central position of the cylinder is indicated using the cross. Flow is in steady-state for Re = 58 and 73.

The velocity profiles averaged over time and over an axial distance from 2D to 14D (i.e. 7 to 49 mm from the cylinder) are shown in Figure 6.1a for all 5 flow conditions studied. The velocity is at its maximum at the upper part of the cylinder, approximately half way between the top pipe wall and the top of the cylinder. The velocity then gradually decreases as the cylinder is approached before increasing again below the cylinder. Close to the bottom pipe wall it reduces to 0. The overall shapes of the profiles look similar to that given previously in Chapter 5 (see Figure 5.1) with high shear zones

near the walls of the pipe and in the vicinity of the cylinder for both steady (no vortex shedding) and unsteady (with vortex shedding) flows.

In Figure 6.1b the velocity profiles normalized by the maximum velocity within the field of view are plotted at a location immediately downstream of the bluff body (0.5D or 1.8 mm). The velocity profiles shown are almost symmetric; the velocity in the upper part of the cylinder changes more gradually towards the centre of the pipe compared to the velocity at the lower part of the cylinder which changes more sharply towards the wall. Symmetric velocity profiles above and below the cylinder were also found in the previous Chapter and by Wang and Tan (2008) at distances larger than 1.5 to 2D downstream of the cylinder. As can be seen in Figure 6.1b, for the steady-state flows at Re = 58 and 73, the local velocity is slightly greater above the cylinder than below it. This is the opposite at higher Reynolds numbers (unsteady flows). However, this slight asymmetry in the profiles above and below the cylinder does not seem to affect the vortex shedding mechanism at high Reynolds numbers. This again agrees with the previous findings given previously in Chapter 5 where the pipe geometry and the chosen gap ratio for the current study ($\gamma = 1.35$) did not disturb the vortex formation mechanism at least for the flows in the central plane of the pipe investigated. The vorticity in the region downstream of the bluff body was calculated using the same equation used in Chapter 5 as before:

$$\omega_z = \frac{\partial V}{\partial x} - \frac{\partial U}{\partial y} \qquad \text{Eq. (5.1)}$$

where U and V represent respectively the horizontal and the vertical velocity components. Time averaged vorticities for three different flow conditions are shown in Figure 6.2. It should be noted that the region directly above the cylinder is not illuminated because the laser light is blocked.

It can be seen in Figure 6.2a, which corresponds to Re = 73 (steady-state flow), that the negative vorticity region above the cylinder is elongated in the axial direction whereas the positive vorticity region below the cylinder is partially supressed and relatively short. This is in good agreement with the pattern observed by Zovatto and Pedrizzetti (2001) at Re = 58 with varying γ between 0.1 ~ 2. They found that the vorticity on the wall side was significantly reduced in length as γ was reduced for steady-state flows where in their case the Re_{crit} was delayed up to 68. As the Reynolds number increased this asymmetry disappeared and both the positive and the negative vorticity regions acquired similar sizes as can be seen in Figures 6.2b and c, due to regular vortex shedding from the top and bottom parts of the cylinder. It can also be seen in Figure 6.2, that the negative vorticity of the boundary layer at the bottom of the pipe is lifted away from the wall at about 10 mm away from the cylinder. This is caused by the interaction of the positive vorticity shed from the bottom part of the cylinder with the negative wall vorticity, as also shown by Zovatto and Pedrizzetti (2001).

To investigate the effect of the wall or the 3D pipe geometry on the vortices generated by the cylinder, the shedding frequencies were calculated using the FFT of the V-velocity component at approximately 6D downstream of the cylinder at the same height as the centre of the cylinder, where the fluctuating

velocity peaks were relatively strong compared to further downstream from the cylinder. The Strouhal numbers evaluated from the frequencies and the average velocity are plotted in Figure 6.3 against the theoretical ones computed from the correlation suggested by Williamson and Brown (1998). It can be seen that the experimental St numbers do not vary significantly from the theoretical values, although the experimental results are either close to or higher than the theoretical ones, with an average standard deviation of less than 3.4%.

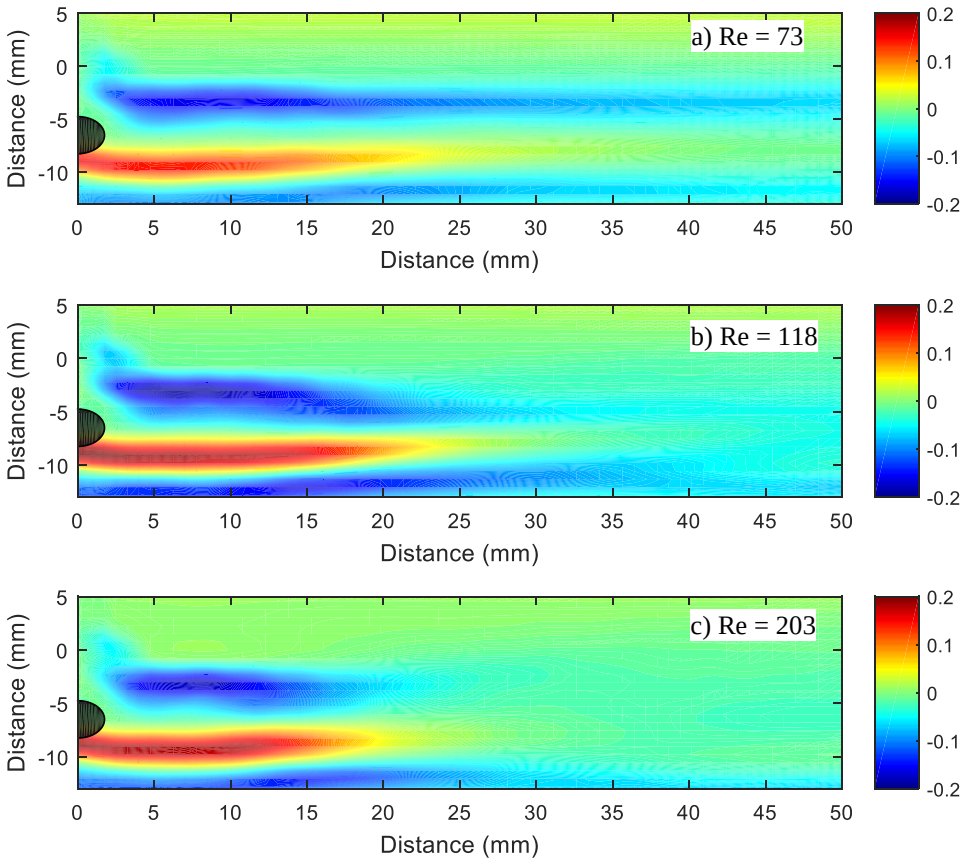

Figure 6.2 Time averaged vorticity downstream the cylinder for different Re. a) Re=73 b) Re=118 c) Re=203

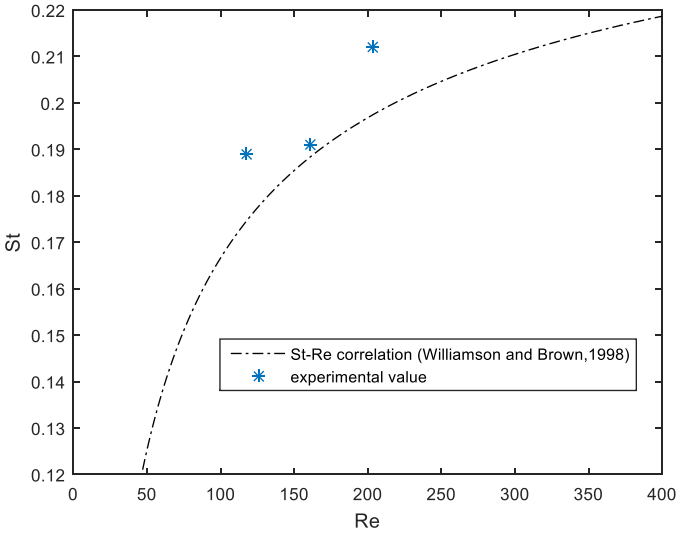

Figure 6.3 Strouhal number against Reynolds number for single phase flows past the cylinder

From the instantaneous velocity fields, information of the vortical structures and the effect of the pipe wall downstream the cylinder can be obtained. According to the definition of Robinson (1991), a vortex exists when instantaneous streamlines mapped onto a plane normal to the vortex core exhibit a roughly circular or spiral pattern, when viewed from a reference frame moving with the centre of the vortex core. However, from this method alone the results may not be clear as the vortical structures may travel at different velocities due to several shear layers (formed at the top and the bottom of the cylinder and the wall shear layer, as shown in Figure 6.2 and justification of the reference frame can be difficult without an a priori method for identifying vortex cores. The computation of vorticity from Equation 5.1 cannot discriminate the shearing and swirling regions of the flow. As previously mentioned in Chapter 5, to help discriminate the shearing from the swirling regions of vorticity, the λ_2 parameter can be used calculated as follows for a 2D velocity field (Jeong and Hussain, 1995):

$$\lambda_2 = \left(\frac{\partial U}{\partial x} + \frac{\partial V}{\partial y}\right)^2 - 4\left(\frac{\partial U}{\partial x}\frac{\partial V}{\partial y} - \frac{\partial U}{\partial y}\frac{\partial V}{\partial x}\right) \quad \text{Eq. (5.2)}$$

For vorticity generated by shearing action, λ_2 is positive, while for vorticity generated by swirling, λ_2 is negative (Vollmers, 2001). Figure 6.4 shows the calculated instantaneous λ_2 with the corresponding relative velocity fields superimposed. Galilean decomposition is applied to the velocity vectors to better visualize the circulation patterns by subtracting the U-velocity component from the average velocity Uw = 0.425 m/s.

It can be seen that the regions of swirling (blue coloured region, $\lambda_2 < 0$) match the circular velocity patterns in all 3 images shown in Figure 6.4 This suggests that the advection velocity of the vortices matches the average flow velocity (in agreement with the results from Chapter 5). The vortices, however, travel faster than previously reported values; Cantwell and Coles (1983) reported U_{ref} = 0.83Usw in the

range x/D < 3 and U_{ref} = 0.55Usw in the range x/D > 4 for a stand-alone cylinder while Wang and Tan (2007) reported U_{ref} = 0.5Uw in the range x/D < 3 in the presence of a wall. Wang and Tan (2007) attributed the difference in the advection velocity compared to that of Cantwell and Coles (1983) to the presence of the wall. The higher advection velocity of the vortices in the current work is likely due to the local acceleration of the fluid between the cylinder and the pipe wall. The advection velocities for other flow conditions (Re = 118 and 203) were also equal to the corresponding average water velocities.

The presence of the walls does not seem to affect significantly the vortex shedding frequencies, although the anti-clockwise rotating vortex at the bottom of the cylinder clearly disturbs the wall boundary layer and generates a secondary clockwise rotating vortex near the pipe bottom wall (see Figure. 6.4 marked as A). The two vortices, first anti-clockwise rotating vortex found at x= 15 mm and the second clockwise rotating vortex at x = 18 mm (marked as B in Figure 6.4) from the wall-side appear to interact and cancel each other. These vortices are dissipated as they are advected further downstream with the bulk flow. Similar interactions between the two opposing vorticities from the cylinder bottom and the wall were previously reported by Grass et al. (1984) and Miyakoshi (1990) but only for very low gap ratios. Further downstream from the cylinder, only the clockwise rotating vortices generated in the upper part of the cylinder remain.

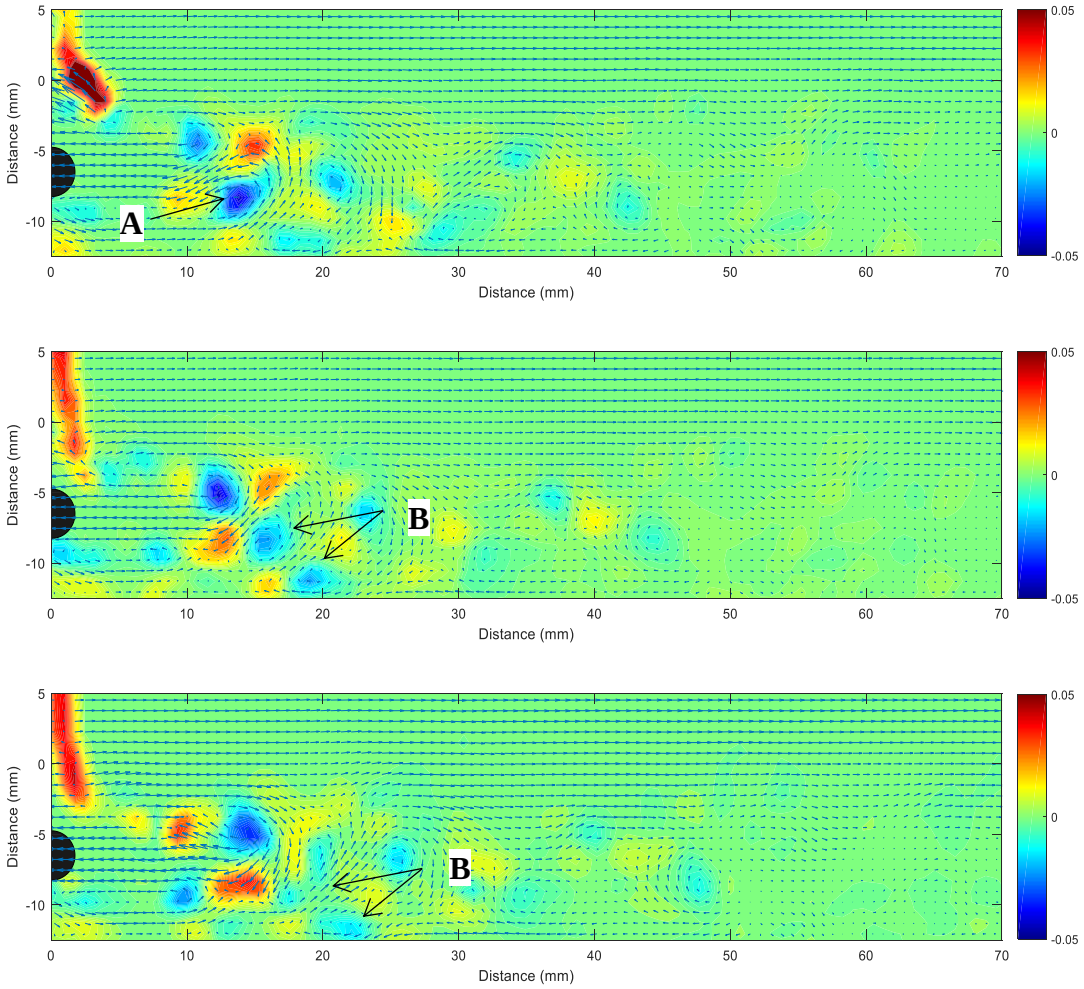

Figure 6.4 Instantaneous λ_2 and superimposed velocity fields for Re = 203 (with reference to U_w = 0.425 m/s). Mark A) negative lambda2 cluster representing the presence of a vortex. mark B) counter rotating vortices shed from the pipe bottom wall. Time delay between each figure is 4 ms. The black semi-circle represents the cylinder.

6.2 Two phase flow

6.2.1 Flow patterns and flow pattern map

The oil-water flow patterns were recorded at 4 m downstream of the inlet to identify the boundaries between stratified and non-stratified flows without and with the bluff body. From a total of 120, cases each with and without the cylinder, the map shown in Figure 6.5 was developed and representative images of the patterns are shown in Figure 6.6. Stratified (ST) flow was observed at low oil and water superficial velocities. At higher velocities (see Figure 6.6) there is a transition first to intermediate (INT) and then to dual continuous (DC) flows. At very low oil-to-water flow rate ratios, the pattern is dispersed oil-in-water flow; at these ratios as the oil superficial velocity is increased, the pattern changes to annular and to dual continuous flow, where an annular-like liquid core positioned at the upper part of the pipe with the presence of oil droplets in the continuous aqueous phase below it (see Figure 6.6e). The transition boundary for the system without bluff body is also shown in Figure 6.5 as dashed line. As can be seen with the bluff body the boundary between stratified and non-stratified flows is largely

shifted towards much lower mixture velocities, in agreement with previous findings. However, the boundaries between the dispersed oil-in-water flow and annular/DC flows were not significantly affected by the presence of the bluff body. This is because at these flow conditions, the dispersion formed immediately after the inlet upstream of the bluff body.

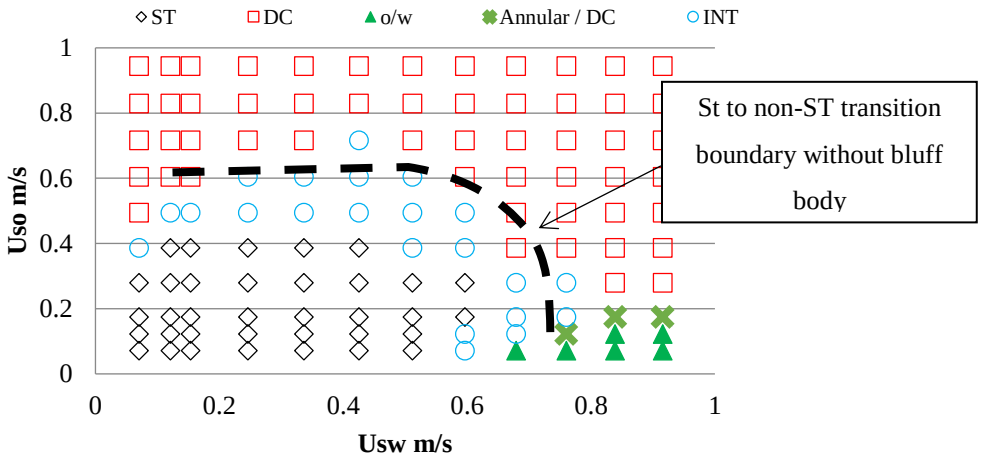

Figure 6.5 Flow pattern map at 4m downstream from the inlet with the bluff body installed

A) Stratified (ST)

Usw = 0.07 m/s, Uso = 0.17 m/s

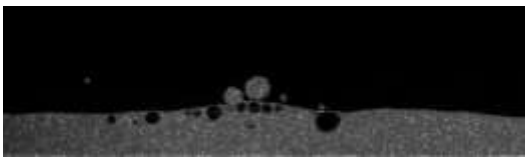

B) Intermediate (INT)

Usw = 0.12 m/s, Uso = 0.49 m/s

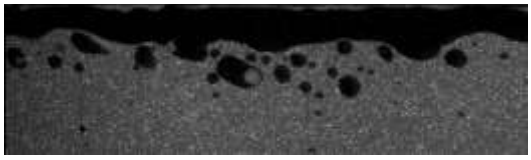

C) Annular / Dual Continuous (Annular / DC)

Usw = 0.92 m/s, Uso = 0.17 m/s

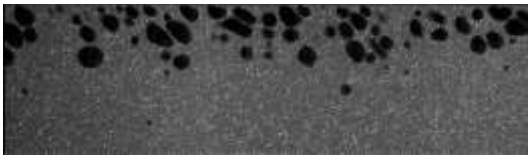

D) Oil dispersed in Water1(o/w)

Usw = 0.68 m/s, Uso = 0.07 m/s

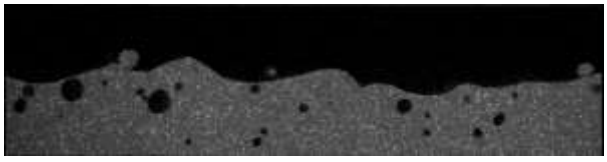

E) Dual Continuous (DC)

Usw = 0.68 m/s, Uso = 0.72 m/s

Figure 6.6 Flow patterns at 4m downstream the cylinder

6.2.2 Flow characteristics downstream of the cylinder

Results on the two phase flows from the previous Chapter (Chapter 5) revealed that the presence of the bluff body was responsible for the generation of interfacial waves immediately downstream of the cylinder and the waves had the same frequencies to the vortices generated by the cylinder. In addition, the presence of the vortices was confirmed and their attachment to the wave crests. Yet the results on the interaction between the cylinder and the oil-water interface remained rather qualitative, and only a limited number of flow conditions were studied due to the mismatch of the refractive indices of the test fluids (see Chapter 2 for detail). In the following section a more quantitative analysis on the effect of the two key flow parameters, h* and Fr, on the flow characteristics and interfacial waves (such as frequency and amplitude) is conducted.

Wave frequencies downstream of the cylinder

First in order to study the generation of vortices by the bluff body and their effect on the oil-water interfacial waves, the frequencies of the waves and of the vortices are compared. Flow conditions within the stratified and stratified-wavy regions of the map with the bluff body were selected for this purpose. These are summarised in Table 6.1. The chosen conditions were split into two groups depending on whether the interface approaching the cylinder was smooth (cases 1-11) or wavy (cases A and B, see section 6.3). The frequencies of the vortices were obtained from the FFT of the V-velocity component at approximately 30 mm away from the cylinder (9D) at the same horizontal level as the centre of the cylinder, while the frequencies of the waves were obtained at 50 mm downstream (interfacial fluctuations were too weak for some conditions at 30mm than 50mm) and of the cylinder from the FFT of the interface signal from the PLIF images.

For flow conditions with a smooth interface approaching the cylinder the effect of the Froude number and the depth of submergence can be more clearly analysed compared to flow conditions with a wavy approaching interface. This is because fluctuations in the oil-water interface approaching the cylinder can give rise to the formation of instantaneous flow structures in the wake of the cylinder (Williamson 1997) different to those observed with a nominally stationary interface.

Table 6.1 Summary of two-phase flow conditions studied

Case No.	Usw (m/s)	Uso (m/s)	Re	Fr	h*	Frequency	
						Vortices	Waves
1	0.07	0.12	82.9	0.93	0.82	13.5	13.5
2	0.07	0.18	88.9	0.99	0.66	20.5	20.5
3	0.12	0.07	100.1	1.12	1.84	13.5	13.5
4	0.12	0.12	116.0	1.30	1.37	18	18.5
5	0.12	0.18	131.4	1.47	1.02	23	23
6	0.16	0.07	126.4	1.41	2.01	15	15
7	0.16	0.12	153.0	1.71	1.38	24	24
8	0.16	0.18	166.4	1.86	1.15	26	26
9*	0.35	0.07	233.5	2.61	2.70	30	**2.5
10*	0.35	0.12	251.7	2.81	2.38	30	**3
11*	0.35	0.18	274.2	3.06	2.04	35	**3

* Flow conditions with frequencies not matched

** Frequency of the strongest IMF

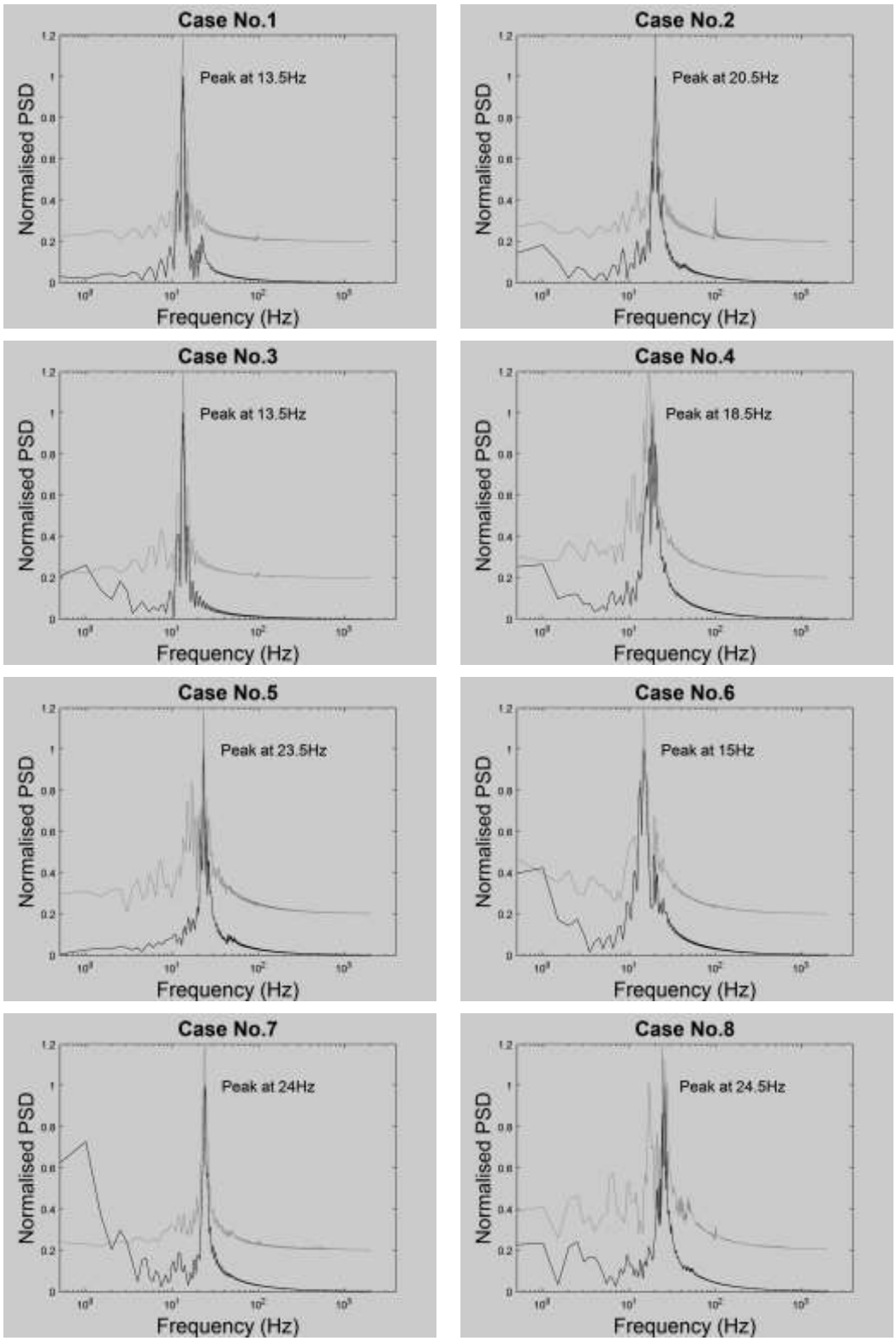

Figure 6.7 Power spectrum of the V-velocity component and interfacial wave signals for different flow conditions. Interfacial wave frequencies are shown in black and V-velocity fluctuation frequencies are shown in grey lines

The flows with an approaching smooth interface (cases 1-11) are first discussed. Representative power spectra of the frequencies are given in Figure 6.7, where the black lines represent the interfacial wave frequencies and the grey lines represent the frequencies of the vortices. Both power spectra are normalized by the maximum peak value. To better distinguish between the two lines, the y-axis of the grey line representing the spectrum of the vortex shedding frequencies has been shifted by +0.2. The peaks of the frequencies for both the interfacial waves and the vortices were found to overlap for cases 1-8, while no other frequencies were identified. This suggests that the von Karman vortices are periodic and cause the interfacial waves, in agreement with previous results from Chapter 5. However, for cases 9-11 the frequencies did not match. It was found that in these cases the power spectrum of the vortex shedding frequencies had strongest peaks with largely greater than the frequency peaks of the interfacial waves. Further discussion on this is given later in this section.

Froude numbers are plotted against the dimensionless depths of submergence in Figure 6.8 for all flow conditions given in Table 6.1 It can be seen that the flow conditions with matched frequencies have relatively low depths of submergence and Froude numbers compared to the cases that have non-matched frequencies. From the 11 flow conditions investigated, an approximate boundary could be drawn separating the flow conditions that have matched frequencies and the conditions that do not match, as shown in the figure with a dashed line.

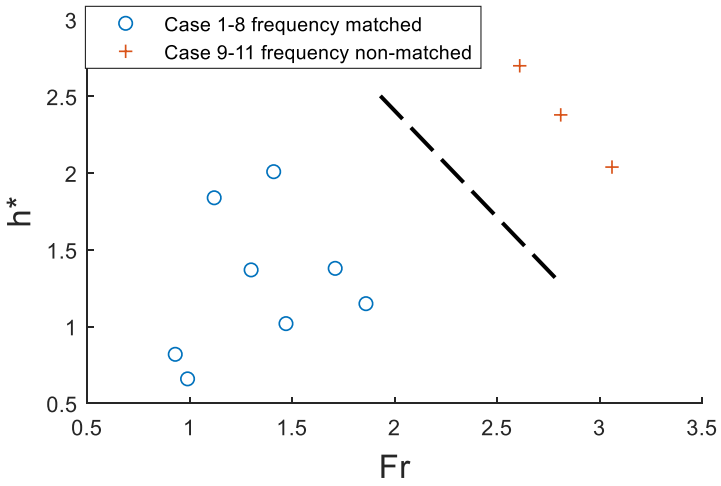

Figure 6.8 Froude number vs depth of submergence for all flow conditions

The two parameters h* and Fr do not only affect the wave frequencies but also other wave characteristics such as the distance at which the waves develop downstream of the cylinder and the wave amplitudes. The wave generation and characteristics can be visualized using a spatio-temporal map as shown in Figure 6.9, where the colour bars represent the fluctuations of the interface from the mean interface height measured in mm. The streaks slightly inclined to the x-axis represent the interfacial waves travelling downstream of the cylinder in time and distance, and the colours show the relative position of the interface to the mean interface height (i.e dark blue and dark red colours are

equivalent to the wave trough and wave crest). As can be seen in all cases, the streaks are equally spaced showing the periodic generation of waves immediately downstream of the cylinder. The effect of h* at the same Fr can be seen in Figure 6.9a. As h* decreases, the distance at which the waves develop is reduced (waves form at x = 30 for case no.6 and at x = 20 for case no.5). In addition, at low h* the waves have larger amplitude in general as there is more interaction between the interface and the cylinder. On the other hand, the Froude number does not have a significant effect on the distance at which the waves first form and the wave amplitude (Figure 6.9b).

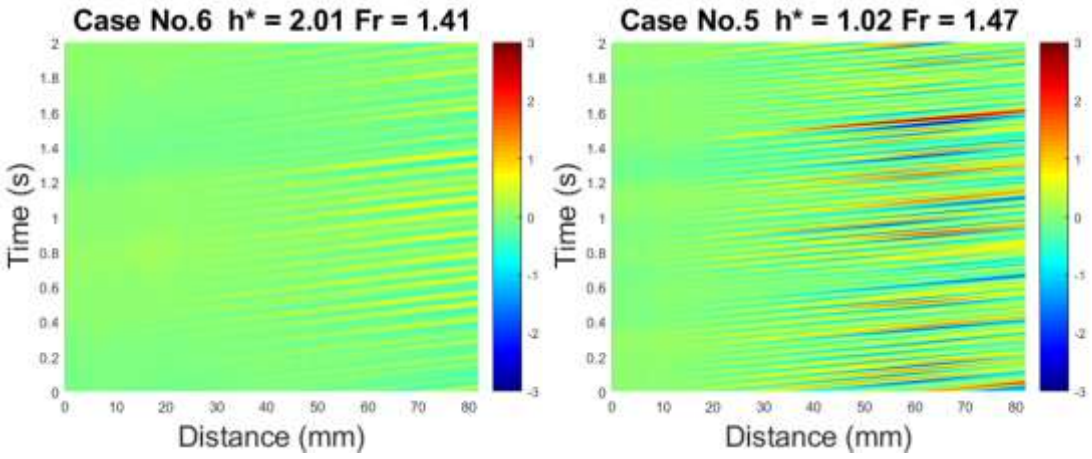

a) Effect of depth of submergence h*

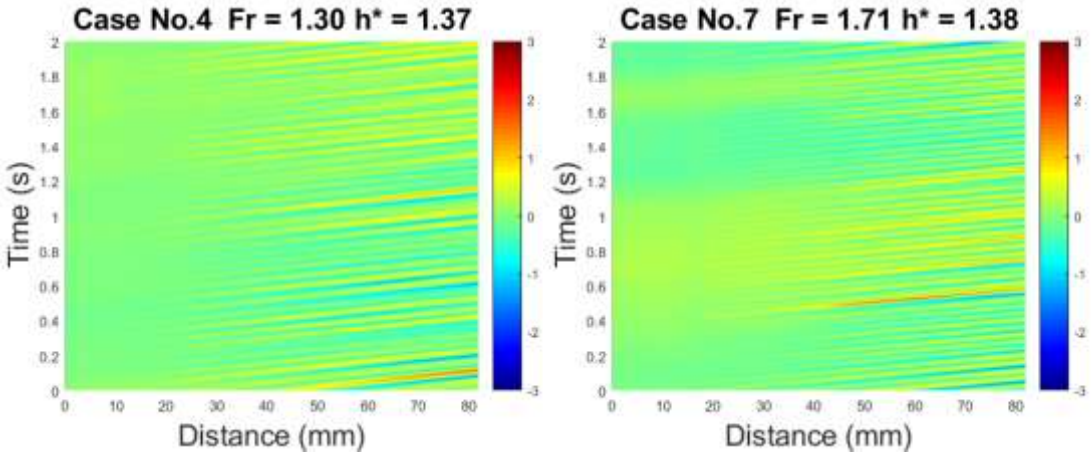

b) Effect of Froude number Fr

Figure 6.9 Spatio-Temporal plot of waves generated downstream the cylinder at different flow conditions. Colour bars represent the fluctuation of the interface measured from the mean height, measured in mm

Given that flow parameters h* and Fr can have an impact on the wave characteristics such as the frequency and amplitude, it is necessary to investigate how the two parameters also affect the vortical structures downstream of the cylinder. For this purpose the velocity fields of the aqueous phase behind the cylinder are further considered. Approximately 20~35 instantaneous flow fields at the same phase of the vortex shedding cycle have been averaged for each flow condition. Cases with matched

frequencies between the wave and the vortex were considered at first. The maximum number of vortices within the field of view varied between 2 – 4 depending on the flow conditions. An example is shown in Figure 6.10 for case No.5 (Fr = 1.47, h* = 1.01) where the relative velocity is superimposed on the λ_2 field. To visualize the recirculation cores, for each flow condition the corresponding average wave velocities were subtracted from the axial velocity components. In agreement with the previous finding for the flows with matched frequencies between the waves and the vortex shedding, the vortices travelled at the same velocities as the waves. To compute the average wave velocities, two instantaneous interface signals given in distance, separated by a known time were obtained with the PLIF. Through cross-correlation of the two successive interface signals, the average distance the waves travelled was obtained. Using the distance computed from the cross-correlation and given the time separating the two interface profiles is known, the wave velocity could be computed. As can be seen the swirling regions (negative λ_2 values) overlap with the vortices (circular patterns of velocity vectors) which indicates that there is agreement between the advection velocity of the vortices and the velocity of the waves that was used as a reference.

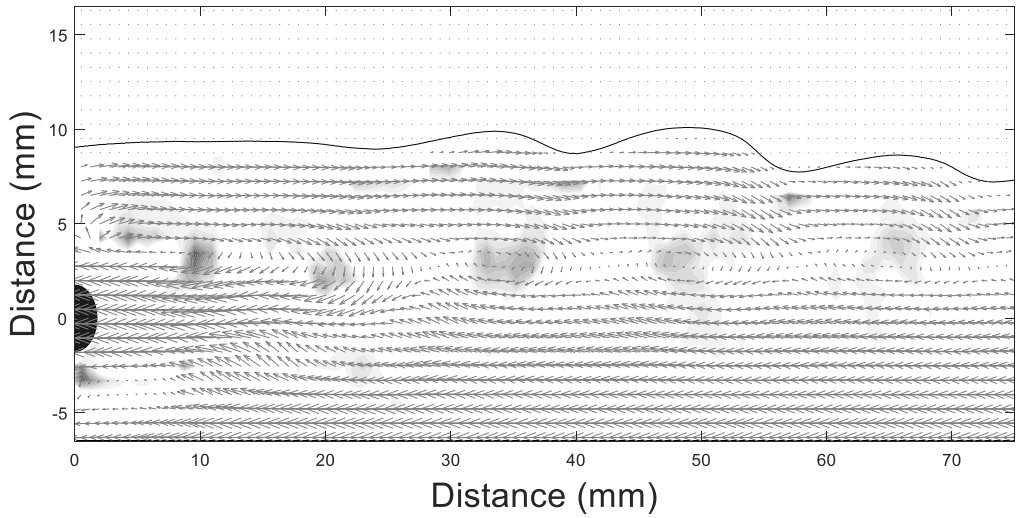

Figure 6.10 Phase averaged $\boldsymbol{\lambda_2}$ with superimposed relative velocity fields with mean wave velocity removed from the U-velocity component for case No.5. Only negative $\boldsymbol{\lambda_2}$ regions are shown in grey

For all flow conditions studied in general, in two phase flows both the negative and positive vorticity regions formed above and below the cylinder and the generated vortices were continuously advected downstream with the bulk flow similar to the single-phase flow at the same velocity as the wave velocity. The locations of the central cores of the clockwise rotating vortices are found on the same x-axis as the locations of the crests of the waves directly above them. Similar observations were reported in the previous Chapter (Chapter 5) where negative vorticity clusters (clockwise rotating vortices) were found underneath the wave crests. However, for the range of conditions studied in the current work, positive vortex clusters (anti-clockwise rotating vortices) were not observed beneath wave troughs. As previously shown in section 6.1 (see Figure 6.4) it was found that the positive vorticity generated from the bottom of the cylinder interacts with vorticity from the wall-side, and cancels out.

Vortex strength and trajectory-

First the impact of h* and Fr are studied here and two aspects are considered objectively; 1) effect of h* and Fr on the evolution of the vortices with distance; and 2) impact of h* and Fr on the generation of vortices i.e looking at the absolute values of the vortex strengths. Given that for the conditions studied the vortices are easily identifiable, the strengths of the vortices generated by the cylinder are calculated in terms of the average circulation Γ estimated from Eq. 6.2. The average circulation is equivalent to an area integral of the vorticity divided by the total area of the vortex defined as:

$$\Gamma = \frac{\iint_A \omega_Z . dxdy}{dA} \quad \text{Eq. (6.2)}$$

The integration area was defined by the regions of swirling and the centres of the vortices were considered as the positions of the local extrema of the vorticity regions (Wang and Tan 2008). The circulation parameter is plotted in Figure 6.11a against the distance of the vortex centres from the cylinder for the 8 cases where the vortex shedding and the wave frequencies matched. It can be seen that in general the strengths of the vortices decrease with distance as their energy is dissipated due to the viscosity of the fluid. In addition, the rate at which the vortices decay with distance for different flow conditions are comparable, with an average decay rate of approximately 4.1 % per cylinder diameter of travel over 35 – 70 mm (equivalent to 10 – 20 D) from the cylinder with standard error of 16%. This result suggests the dimensionless distance h* and Fr do not have a significant impact on the decay of the vortices with distance. The results agree with the numerical simulations by Ponta (2010) for an isolated cylinder which gave an average vorticity decay rate of 4.9% per cylinder diameter of travel over the distance of 10 – 20 D at Re = 100. It appears that the presence of the wall and the oil-water interface do not seem to have a significant effect on the decay rate of the vortices away from the cylinder. Wang and Tan (2008) also reported decay rates in the presence of a wall ($0.2 < \gamma < 2$), were comparable to those of an isolated cylinder (Cantwell and Coles, 1983) but their study was focused at closer distance from the cylinder (<6D).

Now considering the actual values of the strengths of the vortices, it can be seen from Figure 6.11 that in general, the vortices are stronger at higher Fr numbers. For example, at 50 mm away from the cylinder the vortex for case no.8 is approximately 40% stronger than that of case no.3. Similarly at 70mm, the vortex for case no.8 is much stronger than that of cases no 1 and 2. These differences in strengths of the vortices at different Fr was expected, as at higher Fr numbers the velocity of the aqueous phase is higher (Eq 5.1) and the vorticity generated by the cylinder would be greater. However, it appears that the aqueous phase velocity (or Fr) is not a sole factor determining the strengths of the vortices especially when h* is small and this can be seen in Figure 6.11b. In the figure the vortex strengths are normalized by the cylinder diameter and the corresponding actual water velocity. It can be seen that the normalised vortex strengths are comparable for the flow conditions except for cases no 1 and 2 where the

corresponding h* are the smallest. These results suggest vortex strengths are affected both by h* and Fr.

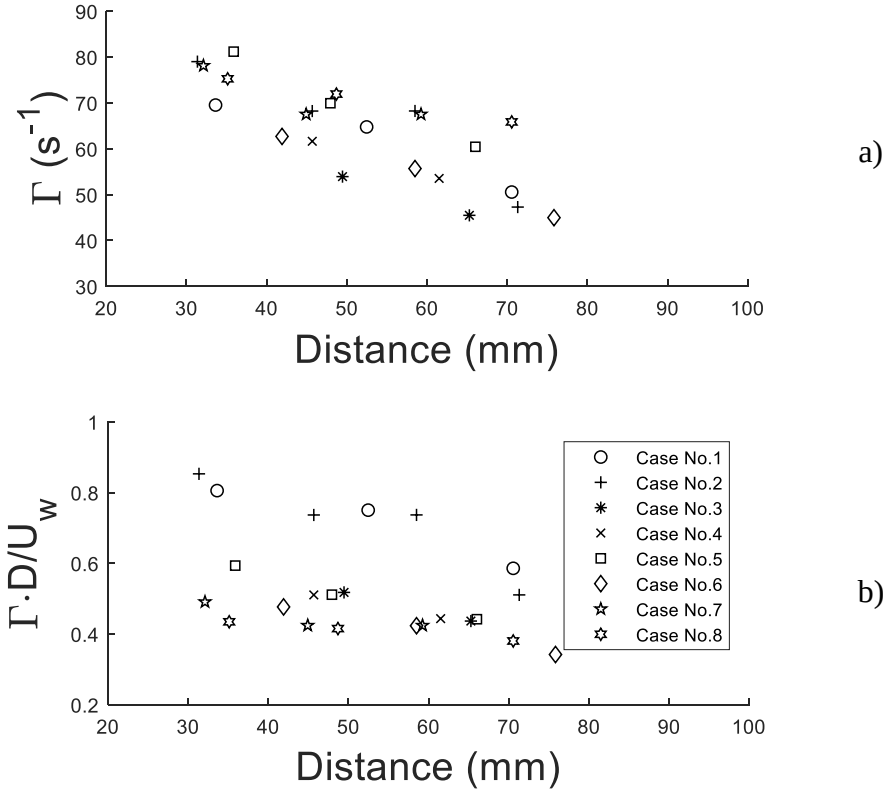

Figure 6.11 Evolution of discrete vortices at different distances away from the cylinder a) absolute vortex strength and b) normalized vortex strength. Distance measured from cylinder centre at x = 0

The impact of the two parameters on the vortex trajectories is given in Figure 6.12 As can be seen from the figure the majority of the vortices are approximately positioned 2.7 mm (0.8D) above the cylinder centre line and only a few vortices are found slightly above at 3.4 (1D) mm or slightly below it at 2.0 mm away from the cylinder. Considering the fact that the accuracy of the positions was limited by the size of the PIV correlation box which is equal to 8 pixels or 0.75 mm, the vertical movement of the vortices are at its minimum. In addition, when compared to the movement of the vortices observed in the previous Chapter (see Figure 5.10 – vortices are positioned at almost 2D above the cylinder centre line), shifting of the vortices observed with the flow conditions studied in this Chapter is relatively small. More discussion on the impact of the vortex strengths and the trajectories on the waves are given in the following section.

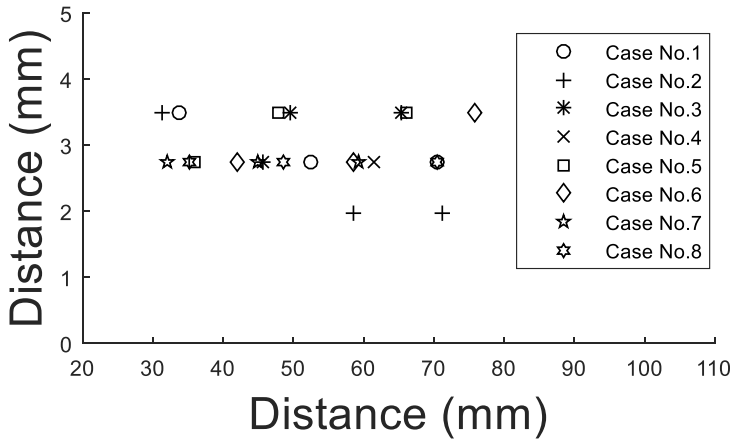

Figure 6.12 Trajectory of discrete vortices – measured from the cylinder centre positioned at x = 0, y = 0

Interaction of vortices with interface

To further investigate the interaction between the vortical structures and the waves, phase-average wave amplitudes on the same location as the vortex centres were obtained (Figure 6.13a). As can be seen the wave amplitudes increased with distance downstream of the cylinder in agreement with the previous finding in Chapter 4. To better visualize the general trend, the standard deviations of the fluctuations of the interface (STDV) are plotted for the entire field of view of the images studied (Figure 6.13b). Interestingly, the rate at which the waves grow seems to depend on the value of h* and the lines shown in Figure 6.13b overlap for similar h* values irrespective of the Fr number values (e.g. similar trends are observed between cases no. 5 and 8, cases no. 3 and 6, cases no. 7 and 4).

Looking at the relationship between the observed trend to the vortex strengths, taking cases no. 5 and 8 first, it can be seen that they have the largest STDV amongst the 8 conditions shown. The vortex strengths for the two cases are among the strong ones as shown in Figure 6.11a with small differences between the two cases – differences are less than 5% between the vortices found at 35 mm and 45 mm for the two conditions. At the same time, the two cases with the smallest STDV values (cases no. 6 and 3) have vortices that are one of the weakest. It appears that stronger vortices tend to generate waves with larger amplitudes and the strength depends on both Fr and h*. However, it seems when the strengths of the vortices are not so different, the wave growth rate is largely influenced by h*.

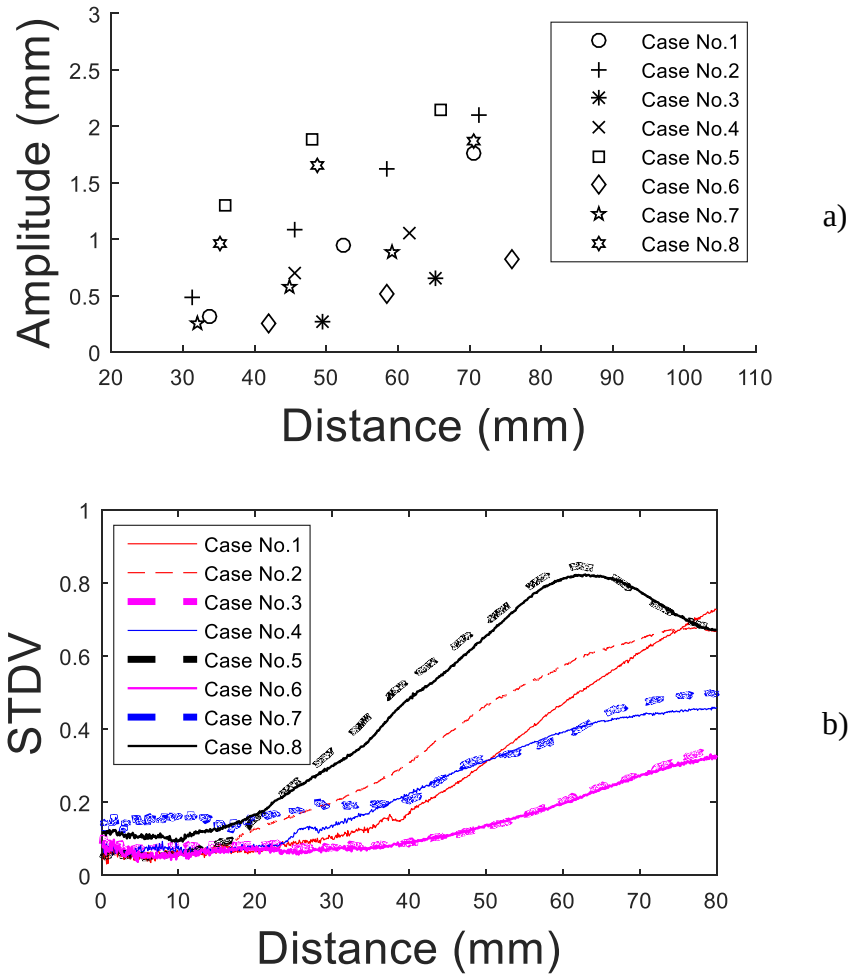

Figure 6.13 a) phase-averaged wave amplitudes above obtained discrete vortices. b) Standard deviation of the fluctuation of the interface signal

Flow conditions with frequencies non-matched

A total of 3 conditions (Case No. 9-11) had the frequencies between the vortex shedding and the interface signals not matched. According to the above findings, the depth of submergence has a significant impact on the flow downstream of the cylinder. As shown in Figure 6.8, in these three conditions h* is large, suggesting that the interactions between the cylinder and the interface would be small.

Looking at the interfacial signals, at these conditions no regular waves were generated as shown in Figure 6.14; the waves are irregular and the distances between the streaks and their thickness are not uniform. Due to the interface signal being non-stationary and non-linear behind the cylinder, it was difficult to carry out a power spectrum analysis via the FFT. Instead, the Hilbert-Huang Transform (HHT) was implemented (Huang, 2014) which can be applied to both non-stationary and non-linear signals. As part of the HHT, the original signal must be broken down into several components called 'Intrinsic Mode Functions (IMF)' via the Empirical Mode Decomposition (EMD) method (further details are given by Huang et al. (1998). By definition, each IMF should satisfy the conditions where:

1) the number of extrema and the number of zero-crossings must either be equal or differ at most by one; and 2) the mean value of the envelope defined by the local maxima and the local minima is zero. In general, each IMF can be regarded as a simple oscillation as a counter part of a harmonic signal (raw signal) such that the sum of all the obtained IMFs will represent the original signal, and usually each IMF carries a physical meaning. For this reason, since its first introduction (Huang et al., 1998), HHT has been used in a wide range of applications in many different fields of studies. For instance, Rai and Mohanty (2007) detected faults in mechanical bearings by identifying the characteristic defect frequencies using the HHT followed by the application of the FFT to the obtained IMFs. Many other applications are mentioned by Wang et al. (2007).

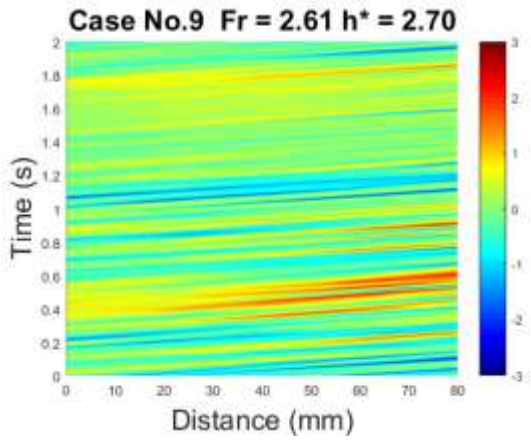

Figure 6.14 Spatio-Temporal plot of waves generated downstream the cylinder for Case No. 9. Mean interface position has been subtracted

For the three cases studied (Case No. 9-11), it was found that on average the interfacial signal could be broken down into 8 to 9 IMFs. Taking Case No. 9 as an example, 8 IMFs were obtained which are given in Figure 6.15. Power spectra for each signal IMF were also obtained and it was found that the 3rd IMF had the matching frequency to that of the vortex shedding frequency. However, as can be seen in Figure 6.15 the 5th and the 6th IMFs have the largest amplitudes suggesting they carry the highest energy. The differences in the energy or the powers of each IMF can be clearly seen in Figure 6.15. From Figure 6.15b it can be seen the 6th IMF has a clear peak at 2.5 Hz and it is the strongest, with the second strongest a peak at 6.5 Hz from the 5th IMF. The power of the 3rd IMF is 3 orders of magnitude smaller than that of the 5th IMF. For the flow conditions with matched frequencies between the wave and the vortex shedding, it was found that the strongest IMFs of the interfacial signals had the same frequencies to those of the vortices. From this it can be said that the interfacial signal downstream of the cylinder for the non-matched cases do entail the characteristic frequencies of the vortices but the impact is very small. It appears that there are other factors that affect the overall characteristics of the interface downstream of the cylinder. However at this stage it is difficult to know the sources of other contributing frequencies and further investigation should be carried out in order to better understand the physical meanings of each IMF obtained.

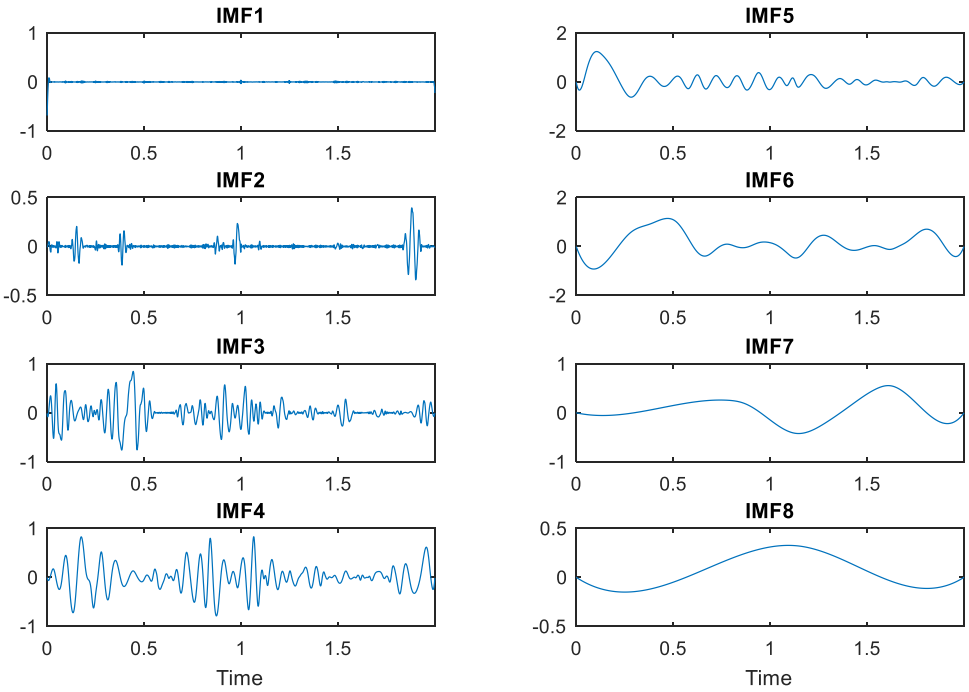

Figure 6.15 IMFs of the interfacial signal for Case No. 9

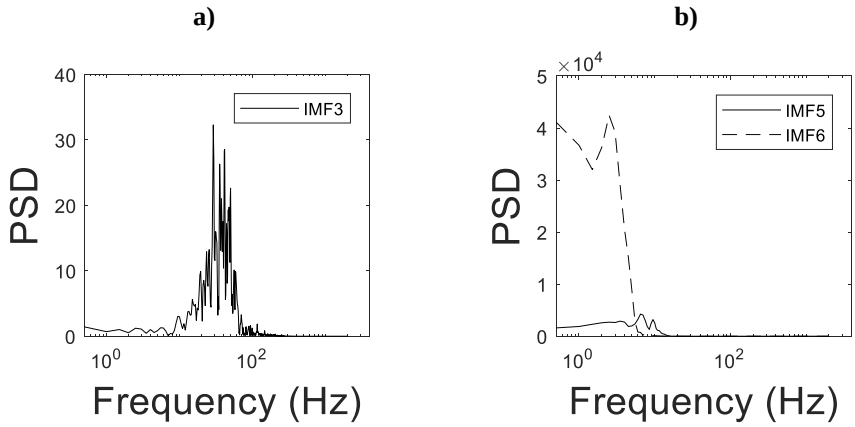

Figure 6.16 PSD of IMFs for Case No. 9. a) IMF3 – peak at 30 Hz. b) IMF5 and IMF6 – peaks at 2.5 and 6.5 Hz

For the three cases only the instantaneous velocity fields could be obtained because the waves are irregular and the phase-averaged flow fields could not be obtained. It was found that the vortices remained horizontal most of the time similar to cases 1-8. However, intermittently, the vortices deviated from the horizontal axis upwards and disturbed the interface. It is possible that this kind of phenomena is related to the fluctuation of the interface approaching the cylinder. However, as the fluctuations of the interface approaching the cylinder were small (< 1 mm), to clearly see the effect cases with larger fluctuations were investigated in the following section.

6.3 Non-stationary interface approaching the cylinder

In previous studies of the interaction of free surface waves with cylindrical bluff bodies, usually the approaching waves were fully characterized beforehand with a chosen amplitude and frequency (Oshkai and Rockwell, 1999). Often the trajectories of the vorticity patterns were investigated at a specific time during a periodic wave cycle. In the current study, however, the waves generated upstream of the cylinder were not preset with chosen amplitude and wavelength, and they were generated naturally due to the slip between the two phases joining at the inlet. At the same time, the waves generated immediately downstream of the cylinder were also irregular in amplitude and shape. Therefore an effort has been put in to qualitatively describe different flow features observed with fluctuating interfaces in comparison to the flows with flat / smooth interfaces approaching the cylinder. In addition the HHT was applied to the signals. For this two cases were considered; Case A (Fr = 2.23 h* = 0.69) and case B (Fr = 3.32 h* = 1.76) and the summary of the flow conditions is given in Table 6.2 below. In both cases no breaking waves were observed or droplets were generated.

Table 6.2 Summary of the two flow conditions studied in section 6.3

			Frequency		
	Fr	h*	incoming flow	vortex	wave
case A	2.23	0.69	8	13.5	*36
case B	3.32	1.76	18	39	*19 **41

* Frequency of the strongest IMF

** Frequency of the second strongest IMF

The frequencies of the interfacial fluctuations were obtained. The frequencies of the fluctuating interface approaching the cylinder were taken at approximately 2D before the cylinder by using the same dataset used to obtain the frequencies of the waves at 50 mm downstream of the cylinder. It was confirmed that in both cases, the incoming flow had strong peaks at non-zero frequencies. Case A showed a strong peak at 8 Hz with a weaker peak at 19 Hz and case B showed a strong peak at 18 Hz.

Now looking at the interfacial signal at 50 mm downstream of the cylinder, case A had a dominant frequency peak at 36 Hz whereas case B had a strong peak at 19 Hz with a second strong peak at 41 Hz – this was obtained via looking at the PSD of the two strongest IMFs. For case B it was found the strongest IMF had almost the same frequency to that of the incoming fluctuations whereas in case A the frequency of the waves was greater than that of the incoming flow. With regards to the vortex shedding frequencies, case A had a peak at 23 Hz, and case B with a peak at 41 Hz. Comparing all three frequencies, case A had no matching frequencies between the incoming flow, vortex shedding and the wave downstream of the cylinder. Case B had matching frequencies between the incoming flow and the interfacial waves downstream of the cylinder, and the vortex shedding frequency was found to be

the second strongest frequency of the wave signal downstream of the cylinder. It was found the number of IMFs was 15 for each case A and B which is higher when compared to the cases with flat interface approaching the cylinder. This suggests the flow is more complex when the incoming flow fluctuates and there are other factors that need to be accounted for to characterize the flow behind the cylinder. In addition, the flow structures behind the cylinder were different when compared to the flows with smooth interface approaching the cylinder.

A typical velocity field with the mixture velocity subtracted from the u-velocity component is superimposed on the λ_2 field as shown in Figure 6.17a for case A. It was found that the flow structures immediately downstream of the cylinder were similar in both cases A and B. As can be seen, the flow is very chaotic and characteristic features of typical von Karman vortex shedding generated by the cylinder are difficult to observe visually. Negative regions of λ_2 of different sizes are rather randomly distributed and the size of the vortices also varies. Unlike the cases with flat interface approaching the cylinder and matched frequencies between the waves and the vortex shedding, clock-wise rotating vortices (negative) are not found beneath the wave crests, for instance several clock-wise rotating vortices, at approximately 25, 32, 27 mm away from the cylinder, are attached along both the wave crest and the trough. The vorticity plot shown in Figure 6.17b suggests that there is a greater interaction between the positive vorticity layer generated at the bottom of the cylinder and the negative vorticity layer from the bottom pipe wall. The negative vorticity layer at the pipe bottom wall is strongly disturbed and breaks off (at 15 and 30 mm downstream of the cylinder in the black circle), and as this happens a new vorticity layer is formed which is stretched in the diagonal direction. It appears that this vorticity layer is long and strong enough to disturb the interface. This break off of the negative boundary layer from the bottom pipe wall did not just occur at the two distances presented (at 15 and 30 mm) but occurred along other axial distances away from the cylinder.

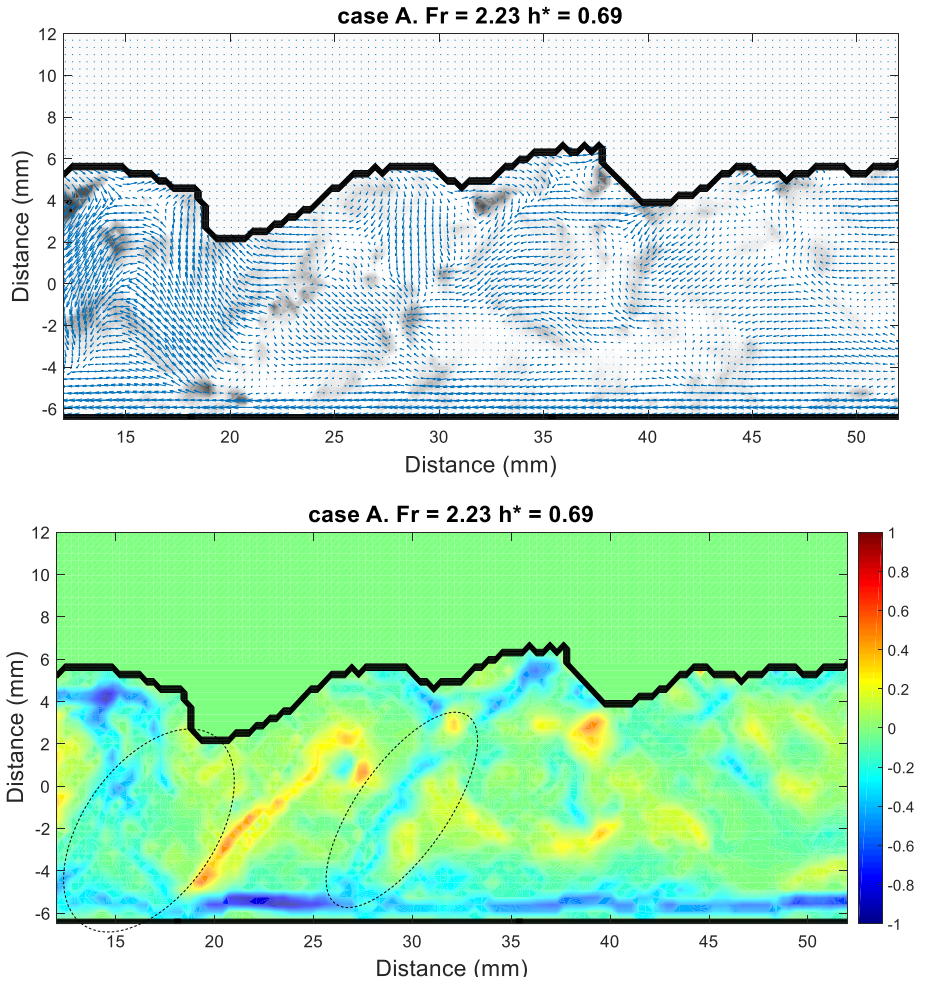

Figure 6.17 Instantaneous flow fields a) $\boldsymbol{\lambda_2}$ with superimposed relative velocity fields with mixture velocity removed from the U-velocity component. Negative $\boldsymbol{\lambda_2}$ regions are shown in grey. b) vorticity plot normalised by its maximum value

6.4 Conclusion

In this Chapter the studies of Chapter 5 are extended and the interaction between oil-water interface and a cylindrical bluff body placed inside a pipe has been experimentally studied by matching the refractive index of the test fluids. As a measuring technique a simultaneous PIV and PLIF were implemented. The velocity fields and velocity profile obtained in single phase flow showed good agreement with the results from the previous Chapter and the frequencies of vortex shedding compared well with the literature ones of unbounded flows. In two-phase flows the frequency of the von Karman vortex shedding and of the interfacial wave frequency showed good agreement for most of the cases investigated with flat interface approaching the cylinder. A few conditions where the two frequencies did not match had relatively large Froude numbers and depth of submergence. The phase averaged flow fields revealed stronger vortices were formed at higher Froude numbers. The decay rate of the vortices with the presence of the interface and the wall was comparable to that of an isolated cylinder. The trajectory of the vortices showed that the majority of the vortices stayed almost horizontal slightly above

the cylinder. In addition, stronger vortices were found to generate waves that are larger in amplitude although the amplitude was more affected by the depth of submergence rather than the Froude number.

For the flow conditions with non-matched frequencies between the waves and the vortex shedding, the interfacial signals were strongly non-linear and non-stationary. However, it was possible to find the vortex shedding frequency in the interfacial signal via the HHT analysis. However other frequencies than the vortex shedding ones had greater impact on the overall flow. Lastly for flow conditions with non-smooth interface approaching the cylinder, the flow fields were rather chaotic due to a high level of interaction between the vorticity layer generated from the bottom of the cylinder and the one from the pipe bottom wall.

By matching the refractive index of the fluids it was possible to study the flow near the oil-water interface that was not possible in Chapter 5 because of the reflection of the light near the oil-water interface. However, in both flow systems, a parametric study investigating the isolated impact of h* and Fr is still difficult. Also, further investigations of the velocity fields in the oil phase are still needed to reveal the flow structures and their interactions with the aqueous phase and the cylinder.

CHAPTER 7. COMPARISON OF FLOWS UPSTREAM VS DOWNSTREAM

In this Chapter, results focusing on the flow characteristics and flow patterns obtained using the flow facility with the matching refractive index liquids are presented and discussed. In section 7.1, flow characteristics immediately downstream of the cylinder are compared against the flow characteristics further downstream (at 4 m from the inlet). Characteristics such as the flow patterns, wave frequencies and average interface height are discussed. In section 7.2 a qualitative description of ligament breaking from non-linear waves immediately behind the cylinder is given.

7.1 Flow comparison between upstream and downstream

7.1.1 Flow patterns

In this section more qualitative description is added to the effects of cylinder on the flow pattern transition boundaries from stratified to non-stratified flows which were briefly discussed in In Chapter and 6. Flow patterns at 4 m downstream (150D) from the inlet with and without the presence of the bluff body were identified from the high speed imaging. Experiments have been carried out for mixture velocities between 0.14 - 0.74 m/s and input oil-to-water flow rate ratios between 0.21 - 5.5. In both setups, a total of 5 different flow patterns were observed, namely; Stratified (ST), Intermediate (INT), Dual Continuous (DC), Oil dispersed in Water (o/w), and Annular and Dual Continuous (Annular/DC). The flow pattern maps for the two systems are plotted in terms of superficial input velocities as shown in Figure 7.1.

Similar flow patterns were observed in both systems. At low oil and water superficial velocities, stratified flow was seen. As the oil superficial velocity is increased, the transition from stratified to intermediate flow takes place. Further increase in the superficial oil velocity leads to transition from intermediate to dual continuous flow. At very low oil-to-water flow rate ratio, when the water superficial velocity is very high compared to the oil superficial velocity, dispersed oil in water flow is observed and at these conditions as the oil superficial velocity is increased, then annular/dual continuous like flow, where an annular-like oil bubbles are found at the upper part of the pipe with the presence dispersed oil droplets in the continuous water phase is observed (see Figure 7.2d). When both oil and water superficial velocities are high then dual continuous flow is observed. However, the transition is delayed to input flow rate ratios close to 1, where the relative velocities between the phases are low (Barral and Angeli, 2013). From Figure 7.1b it can be seen for the system with the bluff body present,

the transition boundary from stratified to non-stratified flow is shifted to lower superficial oil and water velocities which agree with the trend observed in the previous study (Chapter 4). However, the transition boundary between the dispersed oil in water flow and annular/DC flows regions is not largely affected by the presence of the bluff body. This is because at these flow conditions, the oil dispersion forms at the inlet before the oil-water interface reaches the bluff body.

A direct comparison of different flow patterns observed in the two systems under the same flow conditions is shown in Figure 7.2. In general, for stratified flows (Figure 7.2a), the mean positions of the interface heights remain almost the same with and without the presence of the cylinder, and the effect of the bluff body does not seem to have any impact on the flow far downstream of the cylinder (this is further discussed in section 7.1.2). For non-stratified flows a measure on the degree of dispersion, such as drop size distribution has not been carried out in the current thesis, although from visual observations it appears that there is a larger number of droplets when the bluff body is present (Figure 7.2d and 7.2e). From high speed imaging captured at furthest distance downstream the inlet both with and without the cylinder, no droplet detachment phenomena was captured. From this it can be said the droplets are mainly generated in the upstream at the inlet or immediately behind the cylinder. In addition, the generated droplets did not appear to coalesce with the bulk flow even at far downstream the cylinder or the inlet.

Lastly, the flow pattern maps for the two flow facilities (System 1 and 2) are plotted together in Figure 7.3. It is found that the transition boundaries between stratified to non-stratified flows in both systems appear at similar flow conditions. Considering that the two systems have a number of flow parameters that are different, such as the fluid density, viscosity and the pipe sizes, this is very interesting. For flow conditions in stratified flow regime with the bluff body installed in System 1, the range of Re of the aqueous phase, which were calculated using the hydraulic diameters, varied between 12000 and 17000 where the flows are fully turbulent. For system 2 the Re varied between 300 and 2350 where the majority of the flow conditions studied are laminar. Oil-to-water viscosity ratios are 5.5 and 0.5 and the density ratios are 0.83 and 0.80 for System 1 and 2 respectively. For these geometrically similar systems the difference in the fluid physical properties does not seem to have an impact on the transition boundaries at least for the current design of the bluff body as both systems have the same design parameters. However, a more systematic approach would be required to investigate the effect of each parameter such as the size of the bluff body and the position, as well as physical properties of the fluids mentioned.

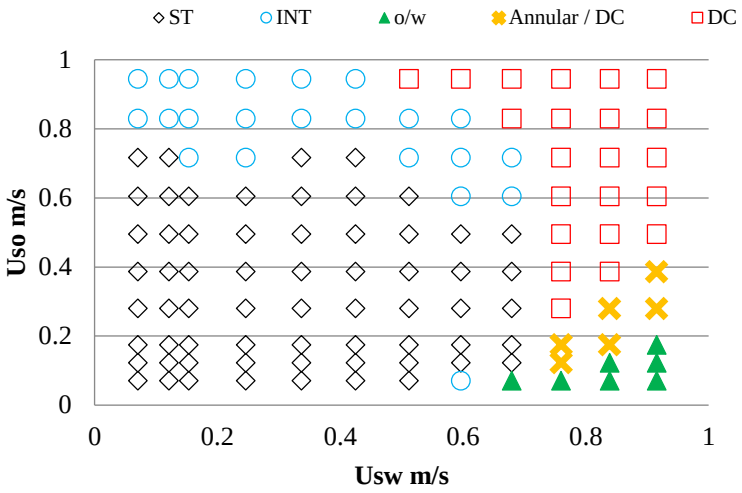

a) Without the presence of the bluff body

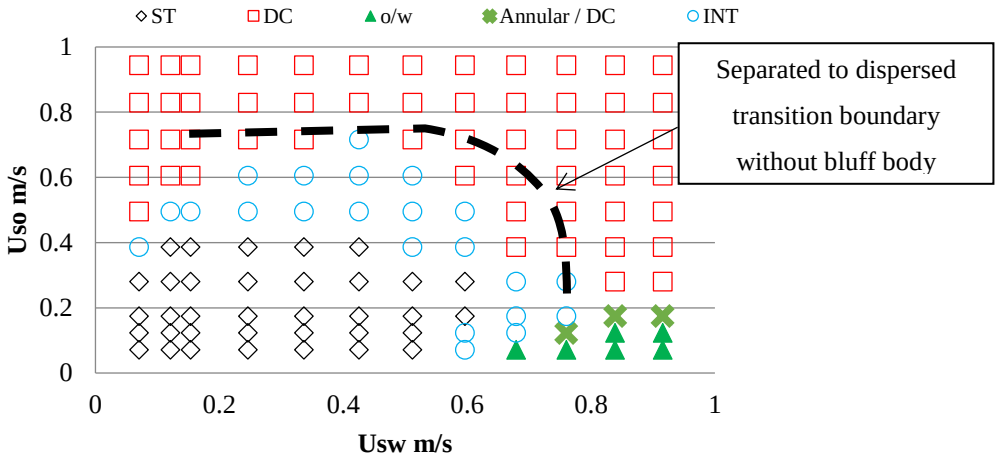

b) With the presence of the bluff body

Figure 7.1 Flow pattern map at 4m downstream from the inlet

Stratified (ST)

a) Usw = 0.07 m/s Uso = 0.17 m/s

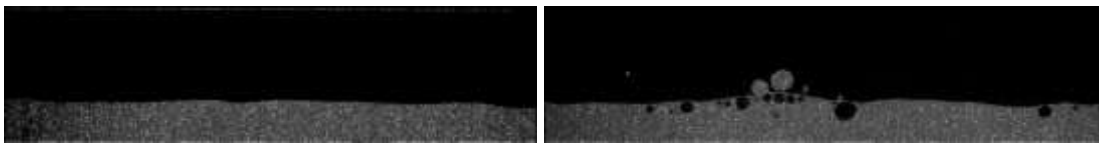

Stratifield (ST, left) Dual Continuous (DC, right)

b) Usw = 0.12 m/s Uso = 0.49 m/s

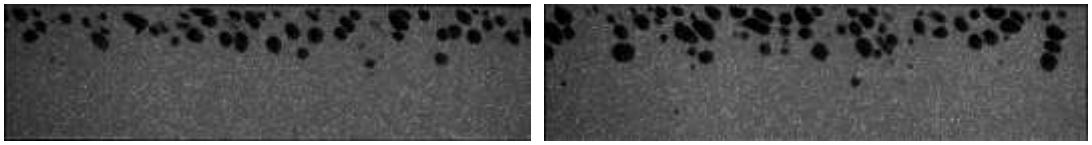

Oil dispersed in water (o/w)

c) Usw = 0.68 m/s Uso = 0.07 m/s

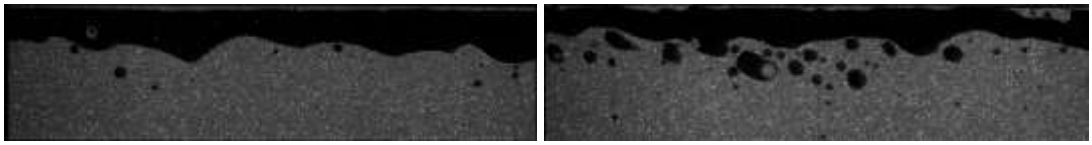

Annular / Dual Continuous (Annular/DC)

d) Usw = 0.92 m/s Uso = 0.17 m/s

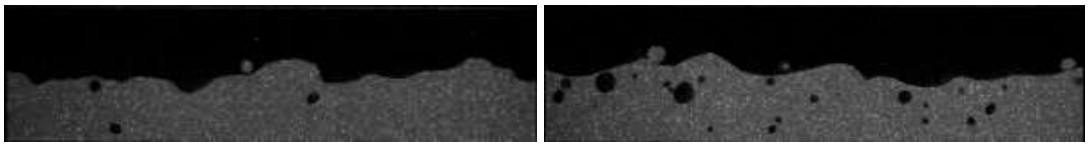

Dual continuous (DC)

e) Usw = 0.68 m/s Uso = 0.72 m/s

Figure 7.2 Comparison of the flow patterns at 4m downstream the inlet without (left) and with the cylinder present (right)

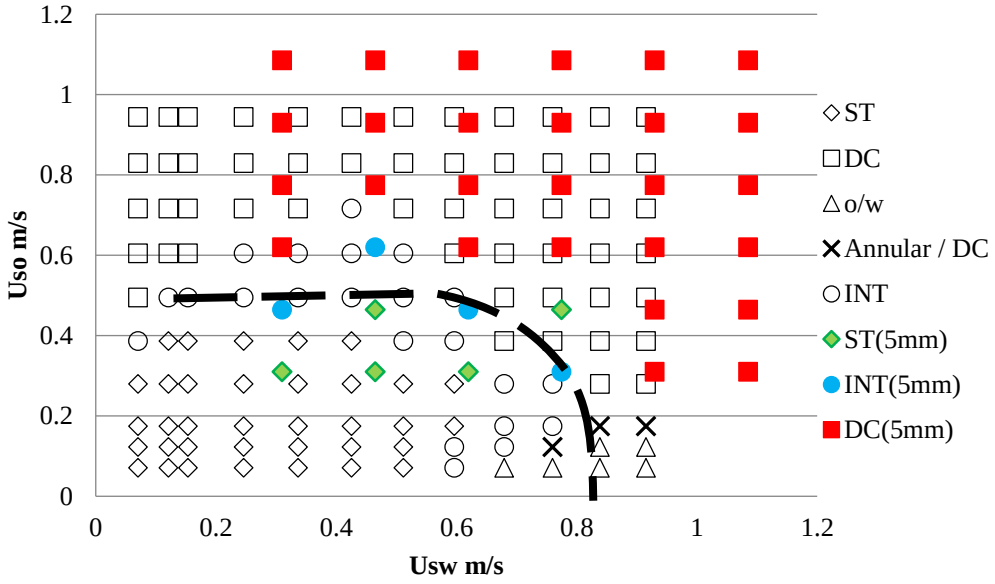

Figure 7.3 Flow pattern maps for the two systems with the cylinder present. In colour: 7 m downstream with 5 mm bluff body in the 37 mm pipe ID (System 1). In black: 4 m downstream with 3.5 mm bluff body in the 26 mm pipe ID (System 2). Dashed line showing the overlapping transition boundary from separated to dispersed flows.

7.1.2 Interface height and frequency

Visual observations were made at two axial locations, immediately after the cylinder when there were waves and at 4 m downstream the cylinder, both with and without the bluff body. It was found that for under certain flow conditions, waves were generated either at the junction where the two fluids meet (i.e at the inlet) or immediately downstream the cylinder with the cylinder present. For the same flow conditions where the waves were observed upstream, at 4 m downstream no visually identifiable waves were seen. To further investigate if any waves are still present at 4m from the inlet, the FFT of the interface signal has been computed to check the dominant frequency for the flow conditions that generated waves immediately downstream of the cylinder. Two flow conditions, previously discussed in Chapter 6, have been selected and the corresponding power spectra and the instantaneous velocity fields are shown in Figure 7.5. In line with the above observations, distinct wave frequencies are detected from the interfacial signal immediately downstream the cylinder (Figures 7.3a and d). On the other hand, PSD obtained using the interfacial signal at 4m downstream the cylinder have strong peaks closer to 0 Hz suggesting the interface is almost constant and flat. In addition, the instantaneous velocity fields obtained represent well of a typical laminar stratified flow where the interface is smooth and with very small velocity fluctuations in radial direction. An attempt has been made to check the presence of any recirculation cores by subtracting the corresponding mixture velocity from the u-velocity components but no observable recirculation cores were found and only negligible vertical velocity fluctuations were seen. The results suggest that the interfacial waves generated close to the inlet, including the waves generated due to the presence of the cylinder, disappear with distance in agreement with the previous finding reported by Barral (2014).

The effect of the cylinder on the mean position of the interface at 4 m downstream the cylinder was also investigated. The average interface at 4 m downstream of the inlet, for a total of 25 flow conditions in stratified regime for both cases with and without the cylinder present is shown in Figure 7.4. For each flow condition, 8000 images were averaged which is equivalent to 2 seconds. Standard deviations of the interface heights in time are shown as error bars. It can be seen that the differences in the average interface heights between the two systems, with and without the presence of the cylinder, are within the error bars. However, there are a few flow conditions where the mean positions between the two systems are outside the standard deviations of the two mean values. It was found from the one-dimensional two-fluid model (see Appendix A), where this model is used to predict the pressure drop and the mean position of the interface (Al-Wahaibi and Angeli, 2007; Al-Wahaibi et al., 2007; Brauner and Moalem, 1992a), that these deviations are within the error margin which could come from the flow meter as the input flow velocities are manually adjusted using a gate valve. The model was written in MATLAB and was used to cross-validate the experimental results obtained for stratified flows. This model showed good agreement with the experimental results.

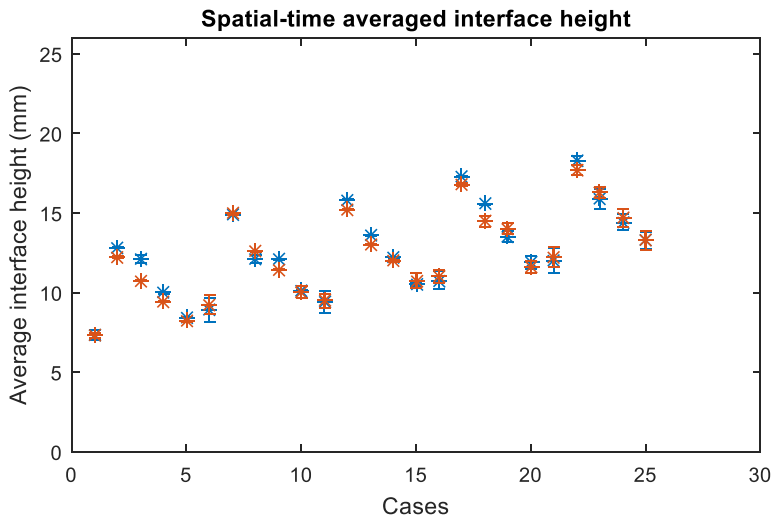

Figure 7.4 Spatial and time averaged interface height for 25 flow conditions in ST regime. Blue marker – system with the bluff body and Red marker – system without the bluff body

Case No.3 Fr = 1.12 h* = 1.84

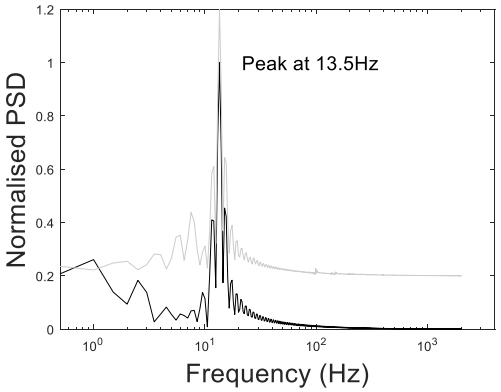

a) PSD of interfacial signal (gray) and v-velocity components (black) at immediately downstream the cylinder

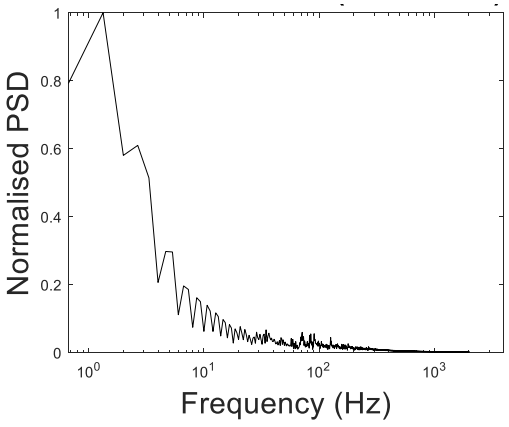

b) PSD of interfacial signal at 4m downstream the bluff body

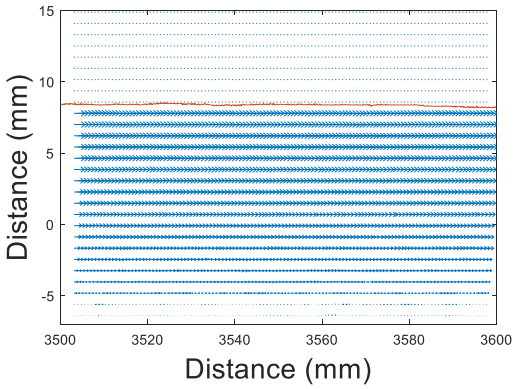

c) Instantaneous velocity field at 4m downstream the cylinder

Case No.5 Fr = 1.47 h* = 1.02

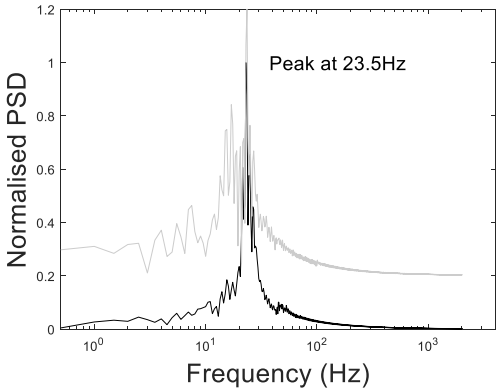

d) PSD of interfacial signal (gray) and v-velocity components (black) at immediately downstream the cylinder

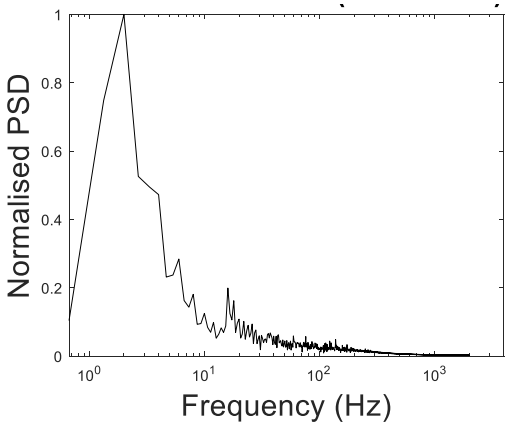

e) PSD of interfacial signal immediately downstream the cylinder

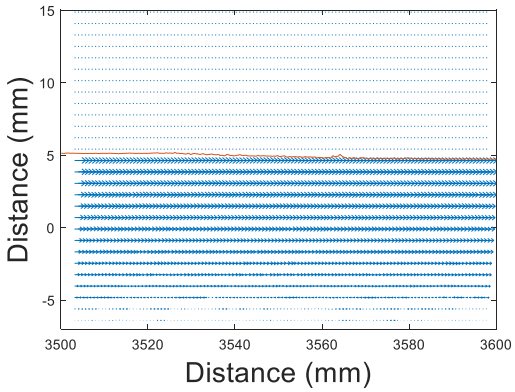

f) Instantaneous velocity field at 4m downstream the cylinder

Figure 7.5 FFT of the interface signal 3.5 m downstream the cylinder and instantaneous velocity field

7.2 Ligament formation and droplet detachment

7.2.1 Visual observation

The mechanism of the ligament breakage from interfacial waves is qualitatively discussed in this section based on the analysis of the high speed PLIF images. The general process of the breakage can be divided into 4 general steps. The first step involves formation of non-linear waves. Figure 7.6 shows the wave formation process due to the presence of the cylinder, which the waves eventually stabilises. Initially the interface is disturbed due to the interaction with the cylinder, and a wave with small amplitude is formed (circled in yellow). As the wave propagates further downstream from the cylinder, it grows in amplitude and at the same time it is deformed with the wave crest tilting towards the direction of the flow. In addition to the presence of the von Karman vortices, this could be caused by the relative movement between the two phases; in the example shown the oil phase velocity is higher, hence the wave crest travels faster than the trough. However further downstream from the cylinder, the wave stabilizes and does not form a ligament. This can be seen from the wave which was formed before the one circled in yellow (circled red) where the wave develops initially but stabilizes at far downstream the cylinder. According to Al-Wahaibi et al. (2007), drop formation from destabilized waves occurs when the destabilizing force from the relative velocity between the phases overcomes the stabilizing force due to surface tension. Following this line of reasoning, the destabilizing waves far downstream the cylinder can be explained from the stratification of the flow, where locally accelerated fluid due to narrowed passage by the presence of the cylinder, starts to decelerate as the distance away from the cylinder is increased (see Chapter 4), causing the slip to be reduced.

Figure 7.7 shows destabilization of waves which forms ligaments and leads to drop detachment. The initial wave formation undergoes the same process as described above where a wave grows in amplitude with distance and becomes non-linear. Here the wave is further deformed and the oil phase is drawn into the aqueous phase as shown by the yellow circle, forming a ligament like thread. Initially this ligament is relatively short and the characteristic thickness of the neck is thicker compared to its length. This ligament grows in length in axial direction and the thickness of the neck is reduced over time. Eventually the neck becomes very thin and the tip breaks off from the ligament as a droplet. The whole process of ligament formation observed in the current system downstream from the cylinder appears to be similar to that of a ligament forming and breaking in a jet-spray system (Umemura and Wakashima, 2002; Umemura, 2007; Shinjo et al., 2009). It is difficult to say, however, if the 'pinch-off' phenomenon of the ligament bulb tip is caused by the presence of capillary waves on the ligament, which has a typical characteristic length of $3.6a_L$ (Shinjo et al., 2009), where a_L is the ligament radius. It is possible that such capillary waves are present, but are not resolved with the current acquisition system. As can be seen in yellow circles from Figure 7.7, unlike the ligaments found in jet-spray systems, the radius is almost constant throughout the entire length of the ligament. According to Shinjo and Umemura (2010) the presence of a capillary wave leads to contraction motion of the ligament bulb tip which eventually leads to the growth of the bulb tip and thinning of the ligament at the same time. In the current system, it appears that the stretching and the thinning of the ligament is rather caused by the relative velocity difference between the advection velocity of the bulb tip and the velocity of the root of the ligament

which is attached to the bulk flow which in this case is the organic phase (silicone oil). It was observed that the formation and breaking of ligaments in the first flow rig (System 1) also follows the same pattern as described here.

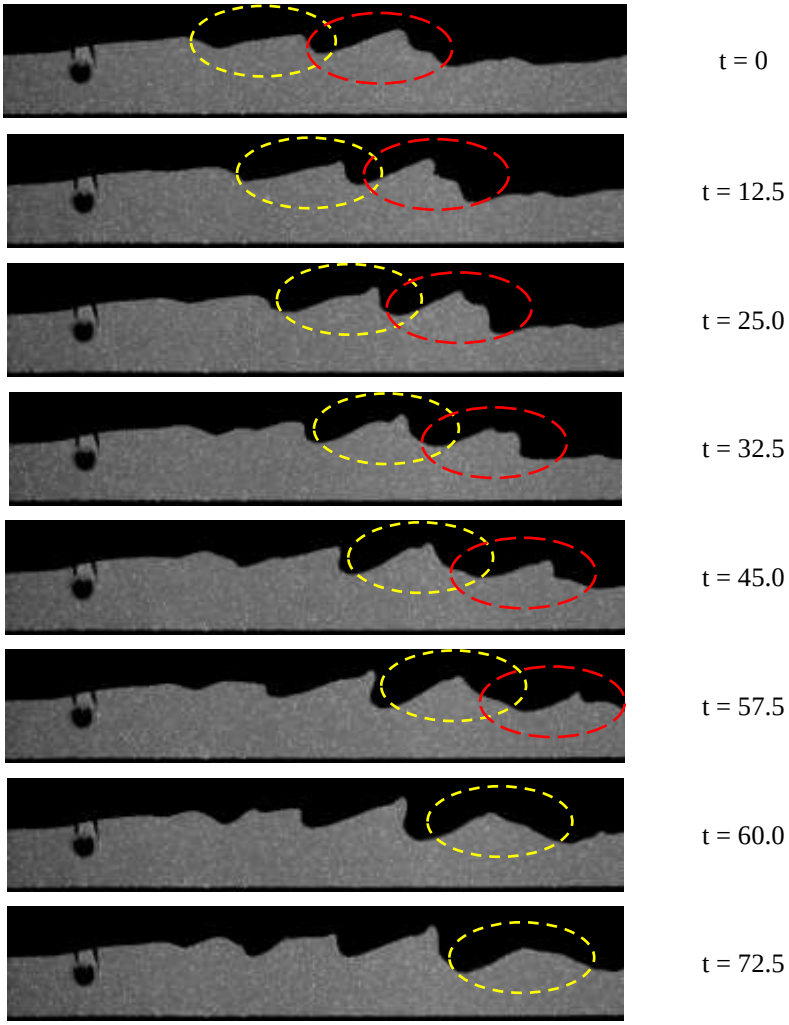

Figure 7.6 Non-linear wave formation. Usw = 0.07 m/s, Uso = 0.28 m/s. Flow direction is from left to right and time delay between images is 12.5 ms

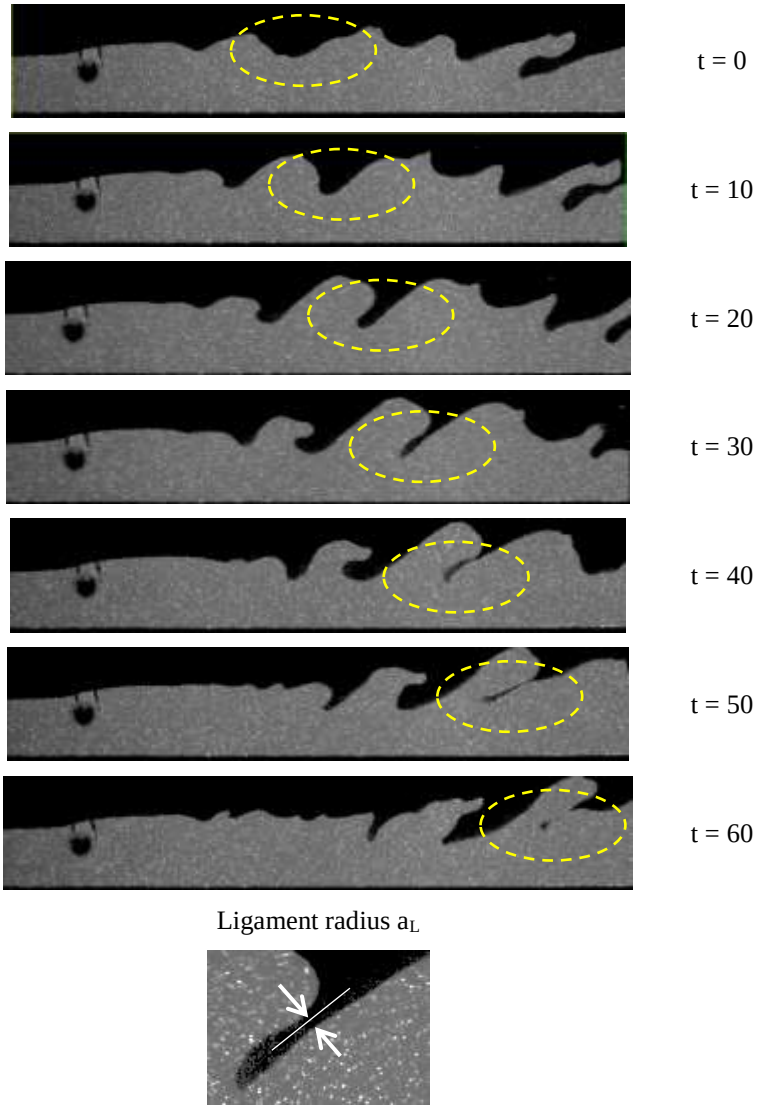

Figure 7.7 Ligament formation and breaking from non-linear waves. Usw = 0.16 m/s, Uso = 0.50 m/s. Flow direction is from left to right and time delay between images is 10 ms

7.2.2 Velocity field around the ligament

In Figure 7.8, the instantaneous velocity fields corresponding to the Figure 7.6 at two different times are shown. As can be seen the very first wave (shown in red circle) has high u-velocity components concentrated at the front of the wave crest. As this wave travels further downstream, the magnitude of the u-velocity component at the wave front is reduced and the concentrated region of high velocity components is shifted towards the central position of the wave. As the shift happens the overall magnitude of the velocity components is also reduced (red circle, Figure 7.8a). Eventually further downstream from the cylinder (> 60 mm), the velocity magnitude is evenly distributed in the axial direction beneath the wave and the waves are not deformed further. Velocity fields around a breaking ligament are shown Figure 7.9. In line with the previous discussion, the wave starts to grow with high velocity components concentrated at the tip of the crest (black circle). These high velocity components remain concentrated at the wave crest as the wave further deforms to form a ligament. On the other hand, the velocity component at the ligament tip (red circle) is relatively low. It is believed that this

velocity difference between the root of the ligament and the ligament bulb tip caused the ligament to stretch and eventually break. In Figure 7.10, the same velocity fields given in Figure 7.8 at t =45 and in Figure 7.9 at t = 30 is shown but with the velocity of the corresponding waves (red and black circles in Figures 7.8 and 7.9, respectively) removed from the u-velocity components. The wave velocity was computed using the distance which the crest of the wave travelled between two separate frames, for instance the wave travelled approximately 20 mm between t = 0 and t = 45 as shown in Figure 7.8, divided by the time separating the two frames. It can be seen in both cases large clock-wise rotating vortices are attached at the wave crests as circled in black arrows. For the non-breaking wave (Figure 7.10a) the central location of the vortex (shown in black dot) is rather shifted towards the rear of the wave crest, with relatively strong negative v-velocity vectors on the wave front causing the wave to stabilize. For the breaking wave (Figure 7.10b) the central location of the vortex core is at the wave crest with strongly positive v-velocity components causing the wave to grow further. Shinjo and Umemura (2010) described the ligament formation processes in two different locations along a liquid jet; from the tip edge and from the liquid core. At the liquid core, ligaments were from the surface waves which were generated due to the relative velocity between the bulk liquid jet and the surrounding air. At the liquid tip, ligaments were mainly formed due to the shear generated from the vortices which were generated behind the tip that rolled into a mushroom shape. As Shinjo and Umemura (2010) suggested, from the current result it appears the presence of the vortices is one of the contributing parameters in generating ligaments to form droplet detachment. However, the velocity fields in the organic phase cannot be obtained at this stage using the current setup, therefore the effect of the slip velocities between the aqueous and the organic phase cannot be investigated. To fully understand the mechanism of ligament formation and breaking in the current system, further analysis on the velocity fields of the organic phases should be obtained.

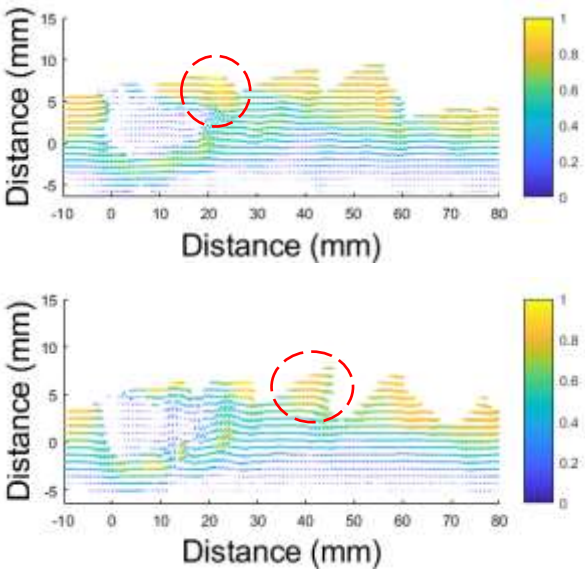

t = 0

t = 45.0

Figure 7.8 Instantaneous velocity fields downstream the cylinder. Usw = 0.07 m/s, Uso = 0.28 m/s. Velocity magnitude has been normalized

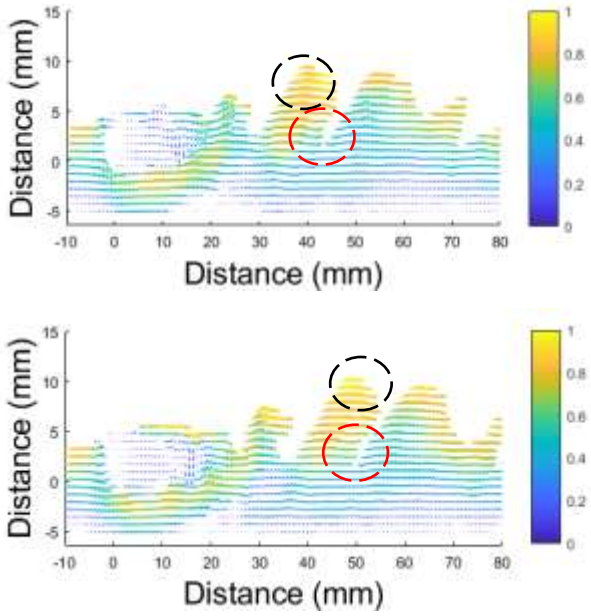

t = 20

t = 30

Figure 7.9 Instantaneous velocity fields downstream the cylinder. Usw = 0.16 m/s, Uso = 0.50 m/s. Velocity magnitude has been normalized

a) Usw = 0.07 m/s, Uso = 0.28 m/s (from Figure 7.8)

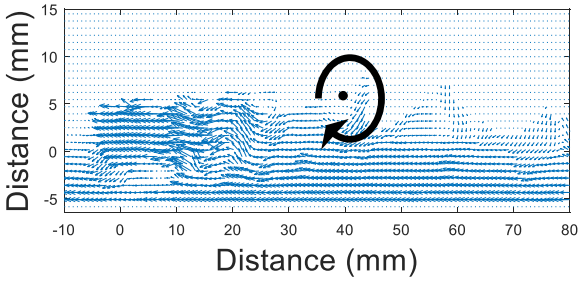

t = 45

b) Usw = 0.16 m/s, Uso = 0.50 m/s (from Figure 7.9)

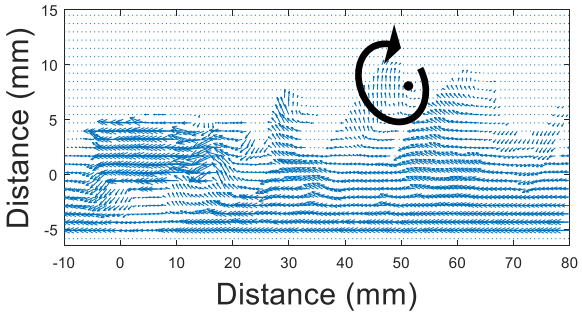

t = 30

Figure 7.10 Instantaneous velocity fields downstream the cylinder for the two flow conditions given in Figures 7.8 and 7.9 with corresponding wave velocity removed from the U-velocity components

7.3 Conclusions

In this Chapter from the image analysis it was found that the presence of the cylinder affected the flow patterns observed further downstream from the inlet. However, waves generated immediately downstream from the cylinder disappeared with distance for wavy flows. From visual observation and from the high speed imaging the flows were stratified with very smooth interfaces. When the droplets were generated upstream, it was found that they did not coalesce with the bulk flow. At the inlet under certain flow conditions, strongly non-linear waves were generated and droplet detachment occurred. Ligaments formed primarily from non-linear waves that were generated at the inlet or immediately downstream the cylinder, which had crests that travelled faster than the troughs. Further thinning and stretching of the ligament eventually led to breaking of the ligament to generate a droplet. The mechanism of wave deformation immediately downstream of the cylinder that led to ligament formation and breaking, which to some extent appear to be similar to that of a process in a jet-spray systems, but requires further analysis and investigation such as obtaining velocity fields in the organic phase.

CHAPTER 8. CONCLUSIONS AND RECOMMENDATIONS FOR FUTURE WORK

8.1 Conclusions

In this Thesis, the effect of a transverse cylinder on the flow pattern actuation and the localisation of interfacial waves and drop formation in horizontal liquid-liquid flows has been investigated. The investigations were carried out with the aid of high speed imaging, double wire conductance probes, particle image velocimetry (PIV) and planar laser induced fluorescence (PLIF) in two different flow loop systems with measurements conducted at different axial locations from the inlet.

The idea of positioning a transverse bluff body closer to an oil-water interface was first inspired from a previous study carried out by Duncan (1981). The hydrodynamics immediately downstream a hydrofoil submerged in water was studied for ship designs, and the result showed a hydrofoil positioned closer to a free-surface generated breaking waves that gave off droplets. Literature on liquid-liquid and gas-liquid studies revealed a possible need of a new approach in obtaining the experimental data to better understand the flow pattern transitions. From this the author decided to adopt a bluff body in the current investigation to cause and localise drop formation in liquid–liquid pipe flow for the first time.

A total of 3 different fields of study were found to be relevant to the work in this Thesis, and a summary of available literature was given in Chapter 2. First, literature on liquid-liquid and gas-liquid flows illustrated the nature and behaviour of the flows without the presence of a cylinder. Second, to aid the design of the experiment, key studies related to the flows around a cylinder with and without the presence of solid boundaries were also summarized. Lastly, wave deformation and formation of ligaments in jet-spray systems were also discussed to help explain the ligament breaking phenomena observed in the current system. Detailed description of the two flow loop systems along with the design considerations for the bluff body was provided in Chapter 3. Basic principles of each of the techniques used to investigate the interfacial characteristics downstream of the cylinder were also explained along with the corresponding experimental setups. The procedures for extracting the information on wave characteristics from high speed images, pre-treatment and analysis of the PLIF images, and on obtaining the velocity fields in the water phase were described in detail. From the error analysis the systematic error in PIV measurements were less than 2.3% for both Systems 1 and 2.

The first set of results obtained using the high speed images on the first flow rig system has been analysed and presented in Chapter 4. Flow pattern map comparison before and after the addition of the bluff body showed that the cylinder successfully actuated the transition from stratified to non-stratified flows. It was found that the presence of the rod generated spatially localised waves shortly downstream, from which drops detach, and reduced the mixture velocity for the transition from stratified to non-stratified flows. The extracted interfacial wave characteristics from images showed the average interface height and wave amplitude increased with distance from the rod for a short distance immediately behind the cylinder, while the same waves vanished at far downstream (7 m). Average wave length remained almost constant with distance and wave velocities slightly higher (10%) than the mixture velocities. While the frequencies of the waves increased with increased water velocities, the corresponding Strouhal number remained almost constant at 0.24. This average Strouhal number was found to be comparable to that of the literature value of 0.2 for vortex shedding behind a cylinder in single phase flows with no wall present. At this stage, it was only possible to assume that the vortices generated by the cylinder were responsible for the interfacial waves which were formed immediately downstream of the cylinder. To validate and to further study the flow structures and interaction between the cylinder and the oil-water interface, high speed PIV was implemented on the same system.

Flow structures and interaction between the cylinder and the oil-water interface were further studied in Chapter 5 using a high speed PIV in single and two-phase flows. From the velocity profiles and flow structures obtained in the middle plane of the pipe in single phase flows, it was found that the flow behind the cylinder was similar to the two dimensional cases. The presence of the lower pipe wall, however, diverted the vorticity layers towards the top of the pipe. In two-phase flows, in high Froude numbers and low depths of submergence the counter rotating von Karman vortices generated by the cylinder interacted with the interface. In this case, the vorticity clusters from the top of the cylinder were seen to attach to the wave crests. At high depths of submergence, a jet like flow appeared between the top of the cylinder and the interface. However, only a limited number of flow conditions that generated smooth waves were investigated and presented in Chapter 5. Due to the non-matched refractive indices of the test fluids, strongly non-linear waves generated at higher flow velocities caused severe distortion of the images and scattering of the laser beam especially near the oil-water interface and the velocity fields were not obtainable.

To overcome the issue caused by the test fluids having different refractive indices, different test fluids to that of System 1 were used in System 2 to gain a closer look near the oil-water interface and near the pipe walls. Simultaneous PIV and PLIF technique was implemented on this flow rig system and the results obtained from the second flow facility was presented in Chapter 6. Some of the import design parameters, such as the gap ratio and the blockage ratio were kept the same as the first system. The velocity fields and the velocity profiles obtained from the single phase was similar to that of the results given in Chapter 5, which were also comparable to a two dimensional flow. Frequencies of the vortex shedding were slightly above those of an isolated cylinder but still comparable to an unbounded flow.

In two phase flows with flat / smooth interface approaching the cylinder, the frequencies between the vortex shedding and the interfacial waves were matched except for flows with high Froude number and depth of submergence. From the phase averaged data the vortex strengths and trajectories were obtained. The rate at which the vortices decayed were similar between cases with different values of Fr and h*, although the depth of submergence had a greater impact on the strengths of the vortices generated underneath the wave crests as well as on the amplitude of the waves in comparison to the impact of the Froude number. The interaction between the shear layer generated at the bottom of the cylinder and the shear layer at the pipe bottom wall was also observed. For flows with fluctuating interface approaching the cylinder, the frequencies between the vortex shedding and the waves were not matched. The flows were rather chaotic and no regular pattern of a typical von Karman vortex shedding was observed.

In Chapter 7, a detailed analysis of the flow patterns with and without the presence of a cylinder was carried out further downstream at 4 m from the inlet. In agreement with the findings in Chapter 3, there was a large shift in the transition boundaries from stratified to non-stratified flows towards lower mixture velocities. The power spectrum of the interfacial signals and the velocity fields showed that the presence of the cylinder did not have an effect on the flows at this location in the pipe when compared to the flows without it. To some extent, the process of ligament formation was comparable to that in jet-spray systems. Waves were initially deformed because the wave crest travelled faster compared to the wave trough, and as the waves continued to deform a ligament was created. Stretching and thinning of the ligament eventually led to droplet detachment.

8.2 Recommendations for future work

The results presented in this Thesis offered insights on the interaction of wakes generated by a fixed transverse cylinder submerged in water, with the interface in a stratified oil-water pipe flow. As part of the main goal, passive actuation of the flow pattern map and spatial localisation of the drop detachment phenomena was achieved. From the flow pattern map it showed the cylinder had no impact on the flows far downstream the inlet at least for stratified flows, hence advanced characterization of the flow immediately downstream the inlet is necessary. Despite the physical insight on the effect of the two main parameters (h* and Fr) affecting the flow, these two parameters are strongly interrelated. The current setup does not allow a control of each parameter separately. From this point of view, a pipe section where the vertical position of the cylinder is controllable should be adopted. This way the effect of the distance away from the pipe wall (gap ratio) as well as the distance from the oil-water interface (depth of submergence) can also be studied at constant flow rates and flow rate ratios. This approach can help achieve the ultimate goal of this study which is to achieve active actuation, where the cylinder will move in motion within the pipe to further generate dispersion to enhance mixing of the two phases, or to dampen the flow approaching the cylinder in order to minimise mixing of the phases.

The FFT results of the vortex shedding signals behind the cylinder matched that of the waves in two phase flows. As the frequency of the shedding is characterized by the size of the cylinder, the investigation should be extended to different sizes and shapes of the cylinder to control the frequency

of the waves. Varying the frequency of the waves / breaking waves could enable a better understanding of the level of dispersion as well as the effect on the flow pattern transition boundaries. Although a qualitative description of the generation of ligaments is briefly given in the final chapter of this thesis, developing a predictive model to describe the transition boundaries in relation to ligament formation and breaking with the cylinder present will help design the future systems. A different design of the inlet can also be considered and possibly with the aid of a CFD.

In addition, to further study the mechanism of drop detachment from ligaments, much larger dataset would need to be obtained and analysed. Planar optical measurement techniques are useful in obtaining the information in the central plane of the pipe. However, high speed imaging from the first flow system showed the ligament formation is rather 3-dimensional than 2-dimensional suggesting the breaking does not always occur in the central plane of the pipe. Using stereo or volumetric measurement techniques, in addition to high resolution camera, would help capture the real shape of the ligament as well as the fluid dynamics around the ligaments. Fluids with different physical properties can also be considered to see the effect of the viscosity and the density on the formation of the ligaments.

REFERENCES

Achenbach, E. and Heinecke, E., 1981. On vortex shedding from smooth and rough cylinders in the range of Reynolds numbers 6× 10 3 to 5× 10 6. *Journal of fluid mechanics*, *109*, pp.239-251.

Adrian, R.J. and Westerweel, J., 2011. *Particle image velocimetry* (No. 30). Cambridge University Press.

Al-Wahaibi, T. and Angeli, P., 2007. Transition between stratified and non-stratified horizontal oil–water flows. Part I: Stability analysis. *Chemical engineering science*, *62*(11), pp.2915-2928.

Al-Wahaibi, T. and Angeli, P., 2008. Droplet size and velocity in dual continuous horizontal oil–water flows. *chemical engineering research and design*, *86*(1), pp.83-93.

Al-Wahaibi, T. and Angeli, P., 2011. Experimental study on interfacial waves in stratified horizontal oil–water flow. *International Journal of Multiphase Flow*, *37*(8), pp.930-940.

Al-Wahaibi, T., 2012. Pressure gradient correlation for oil–water separated flow in horizontal pipes. *Experimental Thermal and Fluid Science*, *42*, pp.196-203.

Al-Wahaibi, T., Smith, M. and Angeli, P., 2007. Transition between stratified and non-stratified horizontal oil–water flows. Part II: Mechanism of drop formation. *Chemical engineering science*, *62*(11), pp.2929-2940.

Al-Wahaibi, T.K., 2006. *Investigations on the transition between stratified and non-stratified horizontal oil-water flows*(Doctoral dissertation, University of London).

Angeli, P. and Hewitt, G.F., 1999. Pressure gradient in horizontal liquid–liquid flows. *International journal of multiphase flow*, *24*(7), pp.1183-1203.

Angeli, P. and Hewitt, G.F., 2000. Flow structure in horizontal oil–water flow. *International journal of multiphase flow*, *26*(7), pp.1117-1140.

Angrilli, F., Bergamaschi, S. and Cossalter, V., 1982. Investigation of wall induced modifications to vortex shedding from a circular cylinder. *Journal of Fluids Engineering*, *104*(4), pp.518-522.

Azzopardi, B.J., 1997. Drops in annular two-phase flow. *International Journal of Multiphase Flow*, *23*(7), pp.1-53.

Bai, R. and Joseph, D.D., 2000. Steady flow and interfacial shapes of a highly viscous dispersed phase. *International Journal of Multiphase Flow*, *26*(9), pp.1469-1491.

Bai, R., 1996. Traveling waves in a high viscosity ratio and axisymmetric core annular flow.

Bannwart, A.C., 1998. Wavespeed and volumetric fraction in core annular flow. *International journal of multiphase flow*, *24*(6), pp.961-974.

Bannwart, A.C., Rodriguez, O.M., de Carvalho, C.H., Wang, I.S. and Vara, R.M., 2004. Flow patterns in heavy crude oil-water flow. *Journal of energy resources technology*, *126*(3), pp.184-189.

Barnea, D. and Taitel, Y., 1993. Kelvin-Helmholtz stability criteria for stratified flow: viscous versus non-viscous (inviscid) approaches. *International journal of multiphase flow*, *19*(4), pp.639-649.

Barnea, D. and Taitel, Y., 1993. Kelvin-Helmholtz stability criteria for stratified flow: viscous versus non-viscous (inviscid) approaches. *International journal of multiphase flow*, *19*(4), pp.639-649.

Barnea, D., 1987. A unified model for predicting flow-pattern transitions for the whole range of pipe inclinations. *International Journal of Multiphase Flow*, *13*(1), pp.1-12.

Barral, A.H. and Angeli, P., 2013. Interfacial characteristics of stratified liquid–liquid flows using a conductance probe. *Experiments in fluids*, *54*(10), p.1604.

Barral, A.H., Ebenezer, A. and Angeli, P., 2015. Investigations of interfacial waves at the inlet section in stratified oil–water flows. *Experimental Thermal and Fluid Science*, *60*, pp.115-122.

Barral, A.H., Edomwonyi-Otu, L.C. and Angeli, P., 2013. Flow patterns and interfacial characteristics in stratified oil–water flows in pipes of different diameter. *Experimental Methods in Multiphase Flows, Jeju, South Korea*, pp.1-6.

Bearman, P. W.,Graham, J. M. R.,Naylor,P.&OBasaju, E. D. 1981. The role of vortices in oscillatory flow about bluff bodies. *In Proceedings of International Symposium on Hydrodynamics and Ocean Engineering*, pp. 621-644.

Bearman, P.W. and Zdravkovich, M.M., 1978. Flow around a circular cylinder near a plane boundary. *Journal of Fluid Mechanics*, *89*(1), pp.33-47.

Bearman, P.W., 1984. Vortex shedding from oscillating bluff bodies. *Annual review of fluid mechanics*, *16*(1), pp.195-222.

Bendat, J.S. and Piersol, A.G., 2011. *Random data: analysis and measurement procedures* (Vol. 729). John Wiley & Sons.

Berger, E. and Wille, R., 1972. Periodic flow phenomena. *Annual Review of Fluid Mechanics*, *4*(1), pp.313-340.

Birvalski, M., Tummers, M.J., Delfos, R. and Henkes, R.A.W.M., 2014. PIV measurements of waves and turbulence in stratified horizontal two-phase pipe flow. *International Journal of Multiphase Flow*, *62*, pp.161-173.

Blevins, R.D., 1990. Flow-induced vibration.

Brauner, N. and Maron, D.M., 1989. 2 Phase liquid liquid stratified flow. *Physicochemical Hydrodynamics*, *11*(4), pp.487-506.

Brauner, N. and Maron, D.M., 1992. Flow pattern transitions in two-phase liquid-liquid flow in horizontal tubes. *International Journal of Multiphase Flow*, *18*(1), pp.123-140.

Brauner, N. and Maron, D.M., 1992. Stability analysis of stratfied liquid-liquid flow. *International journal of multiphase flow*, *18*(1), pp.103-121.

Brauner, N. and Moalem Maron, D., 1999. 'Classification of Liquid-Liquid Two-Phase Flow Systems and The Prediction of Flow Pattern Maps. In *2nd International Symposium on Two-Phase Flow Modeling and Experimentation–ISTP* (Vol. 99, pp. 747-754).

Brauner, N., 2001. The prediction of dispersed flows boundaries in liquid–liquid and gas–liquid systems. *International Journal of Multiphase Flow*, *27*(5), pp.885-910.

Buresti, G. and Lanciotti, A., 1979. Vortex shedding from smooth and roughened cylinders in cross-flow near a plane surface. *The Aeronautical Quarterly*, *30*(1), pp.305-321.

Carberry, J., Sheridan, J. and Rockwell, D., 2001. Forces and wake modes of an oscillating cylinder. *Journal of Fluids and Structures*, *15*(3-4), pp.523-532.

Carberry, J., Sheridan, J. and Rockwell, D., 2004. Cylinder oscillations beneath a free-surface. *European Journal of Mechanics-B/Fluids*, *23*(1), pp.81-88.

Carberry, J., Sheridan, J. and Rockwell, D., 2005. Controlled oscillations of a cylinder: forces and wake modes. *Journal of Fluid Mechanics*, *538*, pp.31-69.

Chaplin, J.R., 1981. On the irrotational flow around a horizontal cylinder in waves. *Journal of Applied Mechanics*, *48*(4), pp.689-694.

Chaplin, J.R., 1984. Nonlinear forces on a horizontal cylinder beneath waves. *Journal of Fluid Mechanics*, *147*, pp.449-464.

Charles, M.E., Govier, G.T. and Hodgson, G.W., 1961. The horizontal pipeline flow of equal density oil-water mixtures. *the Canadian Journal of Chemical engineering*, *39*(1), pp.27-36.

Chen, J.H., Pritchard, W.G. and Tavener, S.J., 1995. Bifurcation for flow past a cylinder between parallel planes. *Journal of Fluid Mechanics*, *284*, pp.23-41.

Cheng, E., Ahmadi, A. and Cheung, K.C., 2015. Measurement of the oscillatory flow field inside tapered cylindrical inkjet nozzles using micro-particle image velocimetry. *Microfluidics and Nanofluidics*, *19*(3), pp.635-646.

Chinaud, M., Roumpea, E.P. and Angeli, P., 2015. Studies of plug formation in microchannel liquid–liquid flows using advanced particle image velocimetry techniques. *Experimental Thermal and Fluid Science*, *69*, pp.99-110.

Choi, J.H. and Lee, S.J., 2000. Ground effect of flow around an elliptic cylinder in a turbulent boundary layer. *Journal of Fluids and Structures*, *14*(5), pp.697-709.

Chomaz, J.M., 2005. Global instabilities in spatially developing flows: non-normality and nonlinearity. *Annu. Rev. Fluid Mech.*, *37*, pp.357-392.

Clanet, C. and Villermaux, E., 2002. Life of a smooth liquid sheet. *Journal of fluid mechanics*, *462*, pp.307-340.

Coutanceau, M. and Defaye, J.R., 1991. Circular cylinder wake configurations: a flow visualization survey. *Applied Mechanics Reviews*, *44*(6), pp.255-305.

Cox, A.L., 1985. *A Study of Horizontal and Down Hill Two-phase Oil-water Flow*. University of Texas at Austin.

de Castro, M.S. and Rodriguez, O.M., 2015. Interfacial waves in stratified viscous oil–water flow. *Experimental Thermal and Fluid Science*, *62*, pp.85-98.

de Castro, M.S., Pereira, C.C., Dos Santos, J.N. and Rodriguez, O.M., 2012. Geometrical and kinematic properties of interfacial waves in stratified oil–water flow in inclined pipe. *Experimental Thermal and Fluid Science*, *37*, pp.171-178.

Dimas, A.A., 1998. Free-surface waves generation by a fully submerged wake. *Wave motion*, *27*(1), pp.43-54.

Ding, H., Shu, C., Yeo, K.S. and Xu, D., 2004. Simulation of incompressible viscous flows past a circular cylinder by hybrid FD scheme and meshless least square-based finite difference method. *Computer Methods in Applied Mechanics and Engineering*, *193*(9-11), pp.727-744.

Dipankar, A. and Sengupta, T.K., 2005. Flow past a circular cylinder in the vicinity of a plane wall. *Journal of Fluids and Structures*, *20*(3), pp.403-423.

Duncan, J.H. and Dimas, A.A., 1996. Surface ripples due to steady breaking waves. *Journal of Fluid Mechanics*, *329*, pp.309-339.

Duncan, J.H., 1981. An experimental investigation of breaking waves produced by a towed hydrofoil. *Proc. R. Soc. Lond. A*, *377*(1770), pp.331-348.

Duncan, J.H., 1983. The breaking and non-breaking wave resistance of a two-dimensional hydrofoil. *Journal of Fluid Mechanics*, *126*, pp.507-520.

Edomwonyi-Otu, L.C. and Angeli, P., 2015. Pressure drop and holdup predictions in horizontal oil–water flows for curved and wavy interfaces. *Chemical Engineering Research and Design*, *93*, pp.55-65.

Edomwonyi-Out, L.C., Barral, A.H. and Angeli, P., 2013, June. Influence of drag reducing agents on interfacial wave characteristics in horizontal oil-water flow. In *16th International Conference on Multiphase Production Technology*. BHR Group.

Faeth, G.M., 1996, January. Spray combustion phenomena. In *Symposium (international) on combustion* (Vol. 26, No. 1, pp. 1593-1612). Elsevier.

Funada, T. and Joseph, D.D., 2001. Viscous potential flow analysis of Kelvin–Helmholtz instability in a channel. *Journal of Fluid Mechanics*, *445*, pp.263-283.

Gerrard, J.H., 1966. The mechanics of the formation region of vortices behind bluff bodies. *Journal of fluid mechanics*, *25*(2), pp.401-413.

Gerrard, J.H., 1978. The wakes of cylindrical bluff bodies at low Reynolds number. *Phil. Trans. R. Soc. Lond. A*, *288*(1354), pp.351-382.

Gondret, P., Ern, P., Meignin, L. and Rabaud, M., 1999. Experimental evidence of a nonlinear transition from convective to absolute instability. *Physical review letters*, *82*(7), p.1442.

Grass, A.J., Raven, P.W.J., Stuart, R.J. and Bray, J.A., 1984. The influence of boundary layer velocity gradients and bed proximity on vortex shedding from free spanning pipelines. *Journal of Energy Resources Technology*, *106*(1), pp.70-78.

Griffin, O.M. and Hall, M.S., 1991. Vortex shedding lock-on and flow control in bluff body wakes. *Journal of fluids engineering*, *113*(4), pp.526-537.

Guzhov, A.I.G., Medredev, V.F., Medredeva, O.P., 1973. Emulsion formation during the flow of two immiscible liquids in a pipe. *Neft Khoz (in Russian)* 8: 58-61

Hernandez Barral, A., 2014. *Stratified wavy oil-water flows*(Doctoral dissertation, UCL (University College London)).

Hewitt, G.F., Pan, L. and Khor, A.H., 1997. Three-phase gas-liquid-liquid flow: flow pattern, holdup and pressure drop. *ISMF*, *97*, pp.7-10.

Hsiang, L.P. and Faeth, G.M., 1992. Near-limit drop deformation and secondary breakup.

Hu, B. and Angeli, P., 2006. Phase Inversion and Associated Phenomena in Oil-Water Vertical Pipeline Flow. *The Canadian Journal of Chemical Engineering*, *84*(1), pp.94-107.

Hu, B., Matar, O.K., Hewitt, G.F. and Angeli, P., 2006. Population balance modelling of phase inversion in liquid–liquid pipeline flows. *Chemical Engineering Science*, *61*(15), pp.4994-4997.

Huang, N.E., 2014. *Hilbert-Huang transform and its applications* (Vol. 16). World Scientific.

Huerre, P. and Monkewitz, P.A., 1990. Local and global instabilities in spatially developing flows. *Annual review of fluid mechanics*, *22*(1), pp.473-537.

Ishii, M. and Grolmes, M.A., 1975. Inception criteria for droplet entrainment in two-phase concurrent film flow. *AIChE Journal*, *21*(2), pp.308-318.

Jana, A.K., Das, G. and Das, P.K., 2006. Flow regime identification of two-phase liquid–liquid upflow through vertical pipe. *Chemical engineering science*, *61*(5), pp.1500-1515.

Jensen, B.L. and Sumer, B.M., 1986. Boundary layer over a cylinder placed near a wall. *Institut of Hydrodynamic and Hydraulic Engineering., Progress Report*, *64*, pp.31-39.

Jeong, J. and Hussain, F., 1995. On the identification of a vortex. *Journal of fluid mechanics*, *285*, pp.69- 94.

Jurman, L.A., Deutsch, S.E. and McCready, M.J., 1992. Interfacial mode interactions in horizontal gas—liquid flows. *Journal of Fluid Mechanics*, *238*, pp.187-219.

Kadri, U., Mudde, R.F., Oliemans, R.V.A., Bonizzi, M. and Andreussi, P., 2009. Prediction of the transition from stratified to slug flow or roll-waves in gas–liquid horizontal pipes. *International Journal of Multiphase Flow*, *35*(11), pp.1001-1010.

Kumara, W.A.S., Halvorsen, B.M. and Melaaen, M.C., 2009. Velocity and turbulence measurements of oil-water flow in horizontal and slightly inclined pipes using PIV. *Computational Methods in Multiphase Flow V*, *63*, p.277.

Kurban, A.P.A., Angeli, P., Mendes-Tatsis, M.A. and Hewitt, G.F., 1995. Stratified and dispersed oil-water flows in horizontal pipes. In *Mechanical Engineering Publications* (pp. 277-291).

Lei, C., Cheng, L. and Kavanagh, K., 1999. Re-examination of the effect of a plane boundary on force and vortex shedding of a circular cylinder. *Journal of Wind Engineering and Industrial Aerodynamics*, *80*(3), pp.263-286.

Lin J, Pao Y. 1979.Wakes in stratified fluids. Annu. *Rev. Fluid Mech*. 11:317–38.

Lin, J.C. and Rockwell, D., 1995. Evolution of a quasi-steady breaking wave. *Journal of Fluid Mechanics*, *302*, pp.29-44.

Lin, J.C. and Rockwell, D., 1996. Force identification by vorticity fields: techniques based on flow imaging. *Journal of Fluids and Structures*, *10*(6), pp.663-668.

Lin, J.C. and Rockwell, D., 1999. Horizontal oscillations of a cylinder beneath a free surface: vortex formation and loading. *Journal of Fluid Mechanics*, *389*, pp.1-26.

Lin, J.T. and Pao, Y.H., 1979. Wakes in stratified fluids. *Annual Review of Fluid Mechanics*, *11*(1), pp.317-338.

Lin, P.Y. and Hanratty, T.J., 1987. Effect of pipe diameter on flow patterns for air-water flow in horizontal pipes. *International journal of multiphase flow*, *13*(4), pp.549-563.

Lin, W.J., Lin, C., Hsieh, S.C. and Dey, S., 2009. Flow characteristics around a circular cylinder placed horizontally above a plane boundary. *Journal of engineering mechanics*, *135*(7), pp.697-716.

Lovick, J. and Angeli, P., 2004. Experimental studies on the dual continuous flow pattern in oil–water flows. *International journal of multiphase flow*, *30*(2), pp.139-157.

Lum, J.Y.L., Lovick, J. and Angeli, P., 2004. Low Inclination Oil-water Flows. *The Canadian Journal of Chemical Engineering*, *82*(2), pp.303-315.

Malavasi, S. and Guadagnini, A., 2003. Hydrodynamic loading on river bridges. *Journal of Hydraulic Engineering*, *129*(11), pp.854-861.

Malavasi, S. and Guadagnini, A., 2007. Interactions between a rectangular cylinder and a free-surface flow. *Journal of Fluids and Structures*, *23*(8), pp.1137-1148.

Malavasi, S., Franzetti, S. and Blois, G., 2004, June. PIV investigation of flow around submerged river bridge deck. In *Proceedings of the International Conference of River Flows, Napoli, Italy* (pp. 601-608).

Malinowsky, M.S., 1975. *An experimental study of oil-water and air-oil water flowing mixtures in horizontal pipes* (Doctoral dissertation, University of Tulsa).

Marmottant, P. and Villermaux, E., 2004. On spray formation. *Journal of fluid mechanics*, *498*, pp.73-111.

Maull, D.J. and Milliner, M.G., 1978. Sinusoidal flow past a circular cylinder. *Coastal Engineering*, *2*, pp.149-168.

Miyata, H., Shikazono, N. and Kanai, M., 1990. Forces on a circular cylinder advancing steadily beneath the free-surface. *Ocean engineering*, *17*(1-2), pp.81-104.

Mohamed-Kassim, Z. and Longmire, E.K., 2004. Drop coalescence through a liquid/liquid interface. *Physics of Fluids*, *16*(7), pp.2170-2181.

Morgan, R.G., Markides, C.N., Zadrazil, I. and Hewitt, G.F., 2013. Characteristics of horizontal liquid– liquid flows in a circular pipe using simultaneous high-speed laser-induced fluorescence and particle velocimetry. *International Journal of Multiphase Flow*, *49*, pp.99- 118.

Mu, H., 2001. *Experimental research on oil-water horizontal pipe flow* (Doctoral dissertation, Master Thesis, University of Petroleum, Beijing, China).

Nädler, M. and Mewes, D., 1997. Flow induced emulsification in the flow of two immiscible liquids in horizontal pipes. *International journal of multiphase flow*, *23*(1), pp.55-68.

Ng, T.S., 2002. *Interfacial structure of stratified pipe flow*(Doctoral dissertation, Imperial College London).

Ngan, K.H., Ioannou, K., Rhyne, L.D. and Angeli, P., 2011. Effect of glycerol addition on phase inversion in horizontal dispersed oil–water pipe flows. *Experimental thermal and fluid science*, *35*(4), pp.628-635.

Ninomiya, N. and Yasuda, K., 2006. Visualization and PIV measurement of the flow around and inside of a falling droplet. *Journal of visualization*, *9*(3), pp.257-264.

Nobach, H. and Bodenschatz, E., 2009. Limitations of accuracy in PIV due to individual variations of particle image intensities. *Experiments in fluids*, *47*(1), pp.27-38.

Oertel Jr, H., 1990. Wakes behind blunt bodies. *Annual Review of Fluid Mechanics*, *22*(1), pp.539-562.

Oglesby, K.D., 1979. *An experimental study on the effects of oil viscosity, mixture velocity and water fraction on horizontal oil-water flow*. University of Tulsa, Fluid Flow Projects.

Oliemans, R.V.A., 1989. The lubricating-film model for core-annular flow.

Oshkai, P. and Rockwell, D., 1999. Free surface wave interaction with a horizontal cylinder. *Journal of Fluids and Structures*, *13*(7-8), pp.935-954.

Pomeau, Y. and Villermaux, E., 2006. Two hundred years of capillarity research. *Physics Today*, *59*(3), p.39.

Prasad, A.K., 2000. Stereoscopic particle image velocimetry. *Experiments in fluids*, *29*(2), pp.103-116.

Price, S.J., Sumner, D., Smith, J.G., Leong, K. and Paidoussis, M.P., 2002. Flow visualization around a circular cylinder near to a plane wall. *Journal of Fluids and Structures*, *16*(2), pp.175-191.

Reichl, P., Hourigan, K. and Thompson, M.C., 2005. Flow past a cylinder close to a free surface. *Journal of Fluid Mechanics*, *533*, pp.269-296.

Rodriguez, O.M.H. and Baldani, L.S., 2012. Prediction of pressure gradient and holdup in wavy stratified liquid–liquid inclined pipe flow. *Journal of Petroleum Science and Engineering*, *96*, pp.140-151.

Rodriguez, O.M.H. and Bannwart, A.C., 2006. Analytical model for interfacial waves in vertical core flow. *Journal of Petroleum Science and Engineering*, *54*(3-4), pp.173-182.

Rodriguez, O.M.H. and Oliemans, R.V.A., 2006. Experimental study on oil–water flow in horizontal and slightly inclined pipes. *International Journal of Multiphase Flow*, *32*(3), pp.323-343.

Roshko, A., 1955, On the Wake and Drag of Bluff Bodies, *J. Aeronaut. Sci.*, Vol. 22, pp. 124–132

Roshko, A., 1961. Experiments on the flow past a circular cylinder at very high Reynolds number. *Journal of Fluid Mechanics*, *10*(3), pp.345-356.

Russell, T.W.F., Hodgson, G.W. and Govier, G.W., 1959. Horizontal pipeline flow of mixtures of oil and water. *the Canadian Journal of Chemical engineering*, *37*(1), pp.9-17.

Sallam, K.A., Dai, Z. and Faeth, G.M., 2002. Liquid breakup at the surface of turbulent round liquid jets in still gases. *International Journal of Multiphase Flow*, *28*(3), pp.427-449.

Sarpkaya, T. 1969 Analytical study of separated flow about circular cylinders. Physics of Fluids 12, Supplement II, 145

Sarpkaya, T., 1968. An analytical study of separated flow about circular cylinders. *Journal of Basic Engineering*, *90*(4), pp.511-518.

Sarpkaya,T. & Isaacson, M. 1981 Mechanics of wave Forces on offshore Structures. New York

Schewe, G., 1983. On the force fluctuations acting on a circular cylinder in crossflow from subcritical up to transcritical Reynolds numbers. *Journal of fluid mechanics*, *133*, pp.265-285.

Schlichting, H., 1974. *Boundary-layer theory*. McGraw-Hill 1968..

Sheridan, J., Lin, J.C. and Rockwell, D., 1997. Flow past a cylinder close to a free surface. *Journal of Fluid Mechanics*, *330*, pp.1-30.

Shi, H., Cai, J.Y. and Jepson, W.P., 1999, June. The effect of surfactants on flow characteristics in oil/water flows in large diameter horizontal pipelines. In *BHR Group Conference Series*

Publication (Vol. 35, pp. 181-200). Bury St. Edmunds; Professional Engineering Publishing; 1998.

Shinjo, J. and Umemura, A., 2010. Simulation of liquid jet primary breakup: Dynamics of ligament and droplet formation. *International Journal of Multiphase Flow*, *36*(7), pp.513-532.

Shinjo, J. and Umemura, A., 2011. Detailed simulation of primary atomization mechanisms in diesel jet sprays (isolated identification of liquid jet tip effects). *Proceedings of the Combustion Institute*, *33*(2), pp.2089-2097.

Shinjo, J., Matsuyama, S., Mizobuchi, Y., Ogawa, S., Umemura, A., 2009. A numerical study on ligament disintegration mechanism by propagative capillary waves. *Atomization*, 36–43

Simmons, M.J.H. and Azzopardi, B.J., 2001. Drop size distributions in dispersed liquid–liquid pipe flow. *International journal of multiphase flow*, *27*(5), pp.843-859.

Singh, S., 1979. Forces on bodies in an oscillatory flow.

Soleimani, A., 1999. Phase Distribution and Associated Phenomena in Oil-Water Lows in Horizontal Tubes. *Ph. D. Thesis, Imperial College of Science, Technology & Medicine*.

Stanislas, M., Okamoto, K., Kähler, C.J., Westerweel, J. and Scarano, F., 2008. Main results of the third international PIV challenge. *Experiments in Fluids*, *45*(1), pp.27-71.

Stone, H.A., 1994. Dynamics of drop deformation and breakup in viscous fluids. *Annual Review of Fluid Mechanics*, *26*(1), pp.65-102.

Taitel, Y. and Barnea, D., 1990. A consistent approach for calculating pressure drop in inclined slug flow. *Chemical engineering science*, *45*(5), pp.1199-1206.

Taitel, Y. and Dukler, A.E., 1976. A model for predicting flow regime transitions in horizontal and near horizontal gas-liquid flow. *AIChE journal*, *22*(1), pp.47-55.

Tănase, N.O., Broboană, D. and Bălan, C., 2014. Free surface flow in vicinity of an immersed cylinder. In *Proc. Rom. Acad., Ser. A* (Vol. 15, No. 4, pp. 371-378).

Taniguchi, S. and Miyakoshi, K., 1990. Fluctuating fluid forces acting on a circular cylinder and interference with a plane wall. *Experiments in Fluids*, *9*(4), pp.197-204.

Tatsuno, M. and Bearman, P.W., 1990. A visual study of the flow around an oscillating circular cylinder at low Keulegan–Carpenter numbers and low Stokes numbers. *Journal of Fluid Mechanics*, *211*, pp.157-182.

Theunissen, R., Scarano, F. and Riethmuller, M.L., 2008. On improvement of PIV image interrogation near stationary interfaces. *Experiments in Fluids*, *45*(4), pp.557-572.

Torres-Monzón, C.F., 2006. *Modeling of oil-water flow in horizontal and near horizontal pipes* (Doctoral dissertation, University of Tulsa).

Trallero, J.L., 1995. *Oil-water flow patterns in horizontal pipes*. University of Tulsa Fluid Flow Projects.

Trallero, J.L., Sarica, C. and Brill, J.P., 1997. A study of oil-water flow patterns in horizontal pipes. *SPE Production & Facilities*, *12*(03), pp.165-172.

Triantafyllou, G.S. and Dimas, A.A., 1989. Interaction of two-dimensional separated flows with a free surface at low Froude numbers. *Physics of Fluids A: Fluid Dynamics*, *1*(11), pp.1813-1821.

Tritton, D.J., 1959. Experiments on the flow past a circular cylinder at low Reynolds numbers. *Journal of Fluid Mechanics*, *6*(4), pp.547-567.

Umemura, A. and Wakashima, Y., 2002. Atomization regimes of a round liquid jet with near-critical mixing surface at high pressure. *Proceedings of the Combustion Institute*, *29*(1), pp.633-640.

Umemura, A., 2007. Self-Destabilizing Mechanism of Circular Liquid Jet. *Japan Society of Aeronautical Space Sciences*, *55*, pp.216-223.

Valle, A. and Utvik, O.H., 1997. Pressure drop, flow pattern and slip for two phase crude oil/water flow: experiments and model predictions. In *Ichmt Digital Library Online*. Begel House Inc..

Valle, A., 1998. Multiphase pipeline flows in hydrocarbon recovery. *Multiphase Science and Technology*, *10*(1).

Varga, C.M., Lasheras, J.C. and Hopfinger, E.J., 2003. Initial breakup of a small-diameter liquid jet by a high-speed gas stream. *Journal of Fluid Mechanics*, *497*, pp.405-434.

Vedapuri, D., Bessette, D. and Jepson, W.P., 1997, June. A segregated flow model to predict water layer thickness in oil-water flows in horizontal and slightly inclined pipelines. In *BHR Group conference series publication*, Vol. 24, pp. 75-106.

Voulgaropoulos, V. and Angeli, P., 2017. Optical measurements in evolving dispersed pipe flows. *Experiments in Fluids*, *58*(12), p.170.

Wang, G., Chen, X.Y., Qiao, F.L., Wu, Z. and Huang, N.E., 2010. On intrinsic mode function. *Advances in Adaptive Data Analysis*, *2*(03), pp.277-293.

Wang, X.K. and Tan, S.K., 2008. Comparison of flow patterns in the near wake of a circular cylinder and a square cylinder placed near a plane wall. *Ocean Engineering*, *35*(5-6), pp.458-472.

Wang, X.K. and Tan, S.K., 2008. Near-wake flow characteristics of a circular cylinder close to a wall. *Journal of Fluids and Structures*, *24*(5), pp.605-627.

Wang, Y., Im, K.S. and Fezzaa, K., 2008. Similarity between the primary and secondary air-assisted liquid jet breakup mechanisms. *Physical review letters*, *100*(15), p.154502.

Wang, Z., Gabriel, K.S. and Manz, D.L., 2004. The influences of wave height on the interfacial friction in annular gas–liquid flow under normal and microgravity conditions. *International journal of multiphase flow*, *30*(10), pp.1193-1211.

Westerweel, J., 1997. Fundamentals of digital particle image velocimetry. *Measurement science and technology*, *8*(12), p.1379.

Williamson, C.H., 1988. Defining a universal and continuous Strouhal–Reynolds number relationship for the laminar vortex shedding of a circular cylinder. *The Physics of fluids*, *31*(10), pp.2742-2744.

Williamson, C.H., 1989. Oblique and parallel modes of vortex shedding in the wake of a circular cylinder at low Reynolds numbers. *Journal of Fluid Mechanics*, *206*, pp.579-627.

Williamson, C.H., 1996. Vortex dynamics in the cylinder wake. *Annual review of fluid mechanics*, *28*(1), pp.477-539.

Williamson, C.H.K., 1996. Three-dimensional wake transition. *Journal of Fluid Mechanics*, *328*, pp.345-407.

Yih, C.S., 2012. *Stratified flows*. Elsevier.

Yusuf, N., Al-Wahaibi, T., Al-Wahaibi, Y., Al-Ajmi, A., Al-Hashmi, A.R., Olawale, A.S. and Mohammed, I.A., 2012. Experimental study on the effect of drag reducing polymer on flow patterns and drag reduction in a horizontal oil–water flow. *International Journal of Heat and Fluid Flow*, *37*, pp.74-80.

Yusuf, N., Al-Wahaibi, Y., Al-Wahaibi, T., Al-Ajmi, A., Olawale, A.S. and Mohammed, I.A., 2012. Effect of oil viscosity on the flow structure and pressure gradient in horizontal oil–water flow. *Chemical Engineering Research and Design*, *90*(8), pp.1019-1030.

Zandian, A., Sirignano, W.A. and Hussain, F., 2016. Three-dimensional liquid sheet breakup: vorticity dynamics. In *54th AIAA Aerospace Sciences Meeting* (p. 1593).

Zdravkovich, M.M., 1997. Flow around circular cylinders volume 1: fundamentals. *Oxford University Press, Oxford*, *19*, p.185.

Zhou, B., Wang, X., Guo, W., Zheng, J. and Tan, S.K., 2015. Experimental measurements of the drag force and the near-wake flow patterns of a longitudinally grooved cylinder. *Journal of Wind Engineering and Industrial Aerodynamics*, *145*, pp.30-41.

Zovatto, L. and Pedrizzetti, G., 2001. Flow about a circular cylinder between parallel walls. *Journal of Fluid Mechanics*, *440*, pp.1-25.

APPENDIX A. TWO-FLUID MODEL

The two-fluid model is commonly used predict pressure drops in liquid-liquid systems. Flow of gas-liquid fluids have longer history of scientific research than liquid-liquid flows which only recently drew attention in the past 20 years or so. Directly application of theories and knowledge developed around gas-liquid flows are sometimes found inadequate to represent liquid-liquid flow systems. This is usually due to the difference in the density and viscosity ratios between the two fluids. The first theoretical work for studying liquid-liquid flows was developed by Neima Brauner and David Moalem Maron. The developed model (Brauner and Maron, 1989) looks at pressure driven stratified flow of oil and water in circular pipes, and all flow parameters are represented in terms of the mean interface height.

The input parameters required for this model is the input flow rates and physical properties of the system, such as the pipe diameter, density and viscosity of the fluids. In return the model predicts the pressure drop of two fluids flowing in a smooth pipe in stratified flow regime and the height of the interface. This is advantageous since time-averaged interface height of the flow system can easily be obtained thus the equations used in the model can also be used calculate the real flow parameters using the experimental data.

Also, there are several assumptions for this model and they are listed as below:

- Both flows are fully developed and are at equilibrium (steady-state)
- Interface between the two fluids is flat
- Momentum and continuity of the mixture and each phase is conserved
- System is pressure-driven and pressure drop of each phase are the same at equilibrium
- System is isothermal

The model comprises both continuity equations and momentum equations. For a fully developed 2 liquids flowing in a pipe, the integral forms of the linear momentum equations for the two layers of fluid are given below where the pressure and shear stresses are regarded as internal forces and gravity as an external force.

$$-A_w(dp/dz) - \tau_w S_w + \tau_i S_i + \rho_w A_w g sinB = 0$$

$$-A_o(dp/dz) - \tau_o S_o - \tau_i S_i + \rho_o A_o g sinB = 0$$

For a horizontal stratified flow in a smooth pipe under the assumption of steady state, when the flows are fully developed it is assumed the pressure drop on both phases are equal. By taking the two momentum balances for each phase and equating them, the following equation is derived as

$$F = -\frac{\tau_w S_w}{A_w} + \frac{\tau_o S_o}{A_o} + \tau_i S_i \left(\frac{1}{A_w} + \frac{1}{A_o} \right) = 0$$

where τ_w, τ_o, τ_i are the water, oil and interfacial shear stresses respectively. Also, $\rho_w A_w g \sin B$ term becomes negligible as the pipe is horizontal in this case (value of B equal zero) The wall shear stresses, τ_w and τ_o are expressed in terms of the corresponding fluid friction factors, f_w and f_o;

$$\tau_w = f_w \frac{\rho_w U_w^2}{2};\ f_w = m \mathrm{Re}_w^{-n} = m \left(\frac{D_w U_w \rho_w}{\mu_w} \right)^{-n}$$

$$\tau_o = f_o \frac{\rho_o U_o^2}{2};\ f_o = m \mathrm{Re}_o^{-n} = m \left(\frac{D_o U_o \rho_o}{\mu_o} \right)^{-n}$$

Smooth pipes and fanning friction factors are considered here. The coefficient m and the exponent n are equal to 0.046 and 0.2 for turbulent flow and to 16 and 1.0 for laminar flow respectively. D_w and D_o are the equivalent hydraulic diameters and the phase with a greater velocity is considered for calculations of equations shown below;

$$D_w = \frac{4A_w}{(S_w + S_i)};\ D_o = \frac{4A_o}{(S_o)}\ for\ U_w > U_o$$

$$D_o = \frac{4A_o}{(S_o + S_i)};\ D_w = \frac{4A_w}{(S_w)}\ for\ U_w < U_o$$

$$D_o = \frac{4A_o}{(S_o)};\ D_w = \frac{4A_w}{(S_w)}\ for\ U_w \approx U_o$$

where the parameters S_i, S_o, S_w, A_o and A_w are defined in Table A.1.

The interfacial shear stress is given by

$$\tau_i = f_i \frac{\rho_i (U_o - U_w)|U_o - U_w|}{2};\ f_i = m\,\mathrm{Re}_i^{-n} = m\left(\left(\frac{S_i}{\pi}\right)\frac{U_i \rho_i}{\mu_i}\right)^{-n}$$

Where

$$\rho_i, U_i, \mu_i = \begin{Bmatrix} \rho_w, U_w, \mu_w \ if\ U_w > U_o \\ \rho_o, U_o, \mu_o \ \ if\ U_w < U_o \end{Bmatrix}$$

By by combining the linear momentum equations with the wall shear stress expressions and removing $\tau_i S_i$, term, an expression for the pressure drop of the liquid-liquid system in a horizontal pipe is obtained thus;

$$Dp/Dz = (-\tau_w S_w - \tau_o S_o)/A$$

Where A is the cross sectional area of the pipe as defined as $A_w + A_o$.in Table A.1. When the ratio of the two phase velocities is between 0.98 and 1.05 (Brauner and Moalem Maron, 1989) then there is no interfacial shear stress and both phases are assumed to flow as in an open channel. The above model is coded in MATLAB.

Table A.1. Geometric parameters used in the two-fluid model

	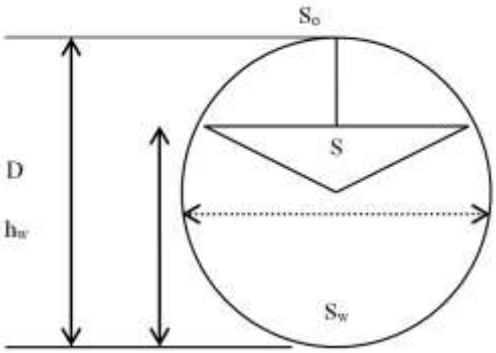
Interfacial length (S_i)	$D \times \left(1 - \left(2\frac{h_w}{D} - 1\right)^2\right)^{0.5}$
Wall perimeter of oil phase (S_o)	$D \times \cos^{-1}\left(2\frac{h_w}{D} - 1\right)$
Wall perimeter of water phase (S_w)	$\pi D - S_o$
Cross sectional area of the pipe (A)	$\frac{\pi}{4}D^2$
Area oil phase (A_o)	$\frac{D}{4} \times (S_o - S_i \times (2\frac{h_w}{D} - 1))$
Area water phase (A_w)	$A_w = A - A_o$
Oil hold-up (H_o)	A_o / A
Water hold-up (H_w)	A_w / A
In-situ oil velocity (U_o)	U_{so} / H_o
In-situ water velocity (U_w)	U_{sw} / H_w

APPENDIX B. PUMP POWER ESTIMATION AND DESIGN

As mentioned in the previously in Chapter 5, one of the problems which occur in making visual observations is optical distortion of the images and it is mainly due to 3 reasons: the difference in the refractive index of the pipe and the fluids, difference in the refractive index between the fluids causing extra reflections of light at the interface, and distortion due to the nature of the pipe geometry, i.e curvature of the circular pipe wall. Going back to the original goal of the thesis which is to study the onset of droplet entrainment, such problems makes it very difficult to make quantitative observations especially in two-phase flows with high flow rates where the interfacial motions are more developed than in stratified flow regimes.

This issue can be of a great problem when it comes to PIV experiments. PIV experiments require very fine calibration of the camera and laser settings as small deviations or errors in optical adjustments can have great impact on the final results such as in the calculation of the mean velocity field. The last two problems mentioned are difficult to eliminate and it is inevitable that there is some degree of optical distortions when making visual observations. However visual observations could be improved through matching refractive index.

Morgan et al. (2013) tried to resolve this issue by adopting a calibration target which tackles the basic problem of setting up camera system (this is more discussed in the next chapter) but also tried to match the refractive index of the fluids. A number of investigations have already been published using two fluids with matched index (Morgan et al., 2013; Ninomiya and Yasuda, 2006). Theoretically by matching the index between the test fluids means reflections on the interface between oil and water does not exist. This would allow me to study closer to the boundary of the interface and this will also help to obtain the velocity field within the developing breaking waves.

B.1 Objectives

There are two main objectives for this upgrade - first is to identify appropriate fluids which have the same refractive index and have reasonable physical properties and second is to replace existing pump and replace with appropriate pumps according to the chosen fluids as well as to improve PVC pipe connections. The PVC pipe connections are also considered in this upgrade since it was found that there are too many unnecessary fittings which largely affects flow pressure drop and contribute towards the

heating process of the fluid temperature. The main test section, separator and storage tanks are excluded as they have relatively small contribution towards overall pressure loss of the system.

B.2 Fluids in consideration

As test by previous researchers, silicon oil and water/glycerol mixture are considered as the two test fluids. In order to save time and cost, an option of keeping the current oil and using water/glycerol mixture was also considered, however, it turned out the amount glycerol required for the water/glycerol mixture was too high resulting the fluid to be too viscous. Several other aspects had to be carefully examined and considered in choosing the correct test fluids as any errors in the early stage of the process can give bad results later. Some of the factors which are taken into account in making the decision are explained further below.

B.2.1 Physical properties

In order to have an experimental setup which could be comparable to the current system, one of the key factors which needs to be taken into account are the physical properties of the fluids. As seen in the previous Chapters, the density and viscosity ratios take important roles in the formation of waves, especially at the inlet. Also, too viscous fluids will require high input flow rates in order to form a turbulent flow where as low viscous fluids tend to have low refractive index which is difficult to match with the acrylic pipe (although there are no fluids that matches the refractive index of the current acrylic pipe, it is helpful to reduce distortion by minimizing the difference between the two). Therefore it is important to find test fluids that have similar physical properties, and keeping the ratios of the two-fluids as near as possible to the current fluids (properties of the current fluids can be found in Table 5).

B.2.2 Safety

Safety aspect is one of the most important factor to be considered when working in labs. The chosen fluids are not hazardous and they are easy to handle. It is well known that glycerol is soluble in water and they do not have chemical reactions, and no reaction between the silicone oil and water/glycerol mixture. Flash points of the silicone oil is also checked. The chosen silicone oil has a flash point of about 120 which is very similar to that of the current oil and it can be regarded as safe. The working environment of the lab does not involve exposure to fire and temperature of the lab is maintained with a good ventilation system.

B.2.2 Availability

Silicone oil and water/glycerol mixture are immiscible, therefore in theory, unless they are contaminated, they can be used for long term with via continuous recycling of the fluids with no further addition of new fluids into the system. However, it is inevitable that there will be some losses of water/glycerol mixture during pipe fittings and cleaning processes therefore it is important to choose fluids that are widely available. Tap water is considered for the water/glycerol mixture and since glycerol are used widely, the chosen fluids are suitable for long term investigation using the system.

B.3 Separation time - preliminary test

A simple and quick test of the separation time between the new test fluids were carried out. Since the separator would not be modified (for now), it was important to have an idea of the separation time and whether the current Knit-Mesh would be functional with the new fluids.

A glass beaker containing 20ml of silicone oil and 20ml of water/glycerol mixture (50%vol) was prepared. Initially 10 ml of water and glycerol were added to the beaker and stirred manually using a stirring rod until the mixture became crystal clear with no visible clusters of glycerol. 20 ml of silicone was then carefully added. Similarly, same amount of the current oil and water was prepared in the same way. Using an electric stirrer, each beaker was stirred for 10 seconds at the same frequency and as soon as the impeller was removed from the beaker, the time was measured. It was the time taken to obtain a smooth interface between oil and water without the presence of visible droplets on the interface.

Results showed that the separation time between the new fluids were much faster (about 2 times) than with the current fluids. This was expected as the separation is normally due to the gravity (density difference) and the density ratio between the new fluids are greater. From this it can be said that the chosen fluids are suitable for the purpose of this experiment.

B.4 Design, layout and calculation

Planning the modification of the pipe connections and choosing the correct size pumps could not be achieved in a single process. Firstly, prior to pre-assessment from an external company (specialists in pump supply and design), a rough estimate of the pump size was required as this work formed a basis to start the project.

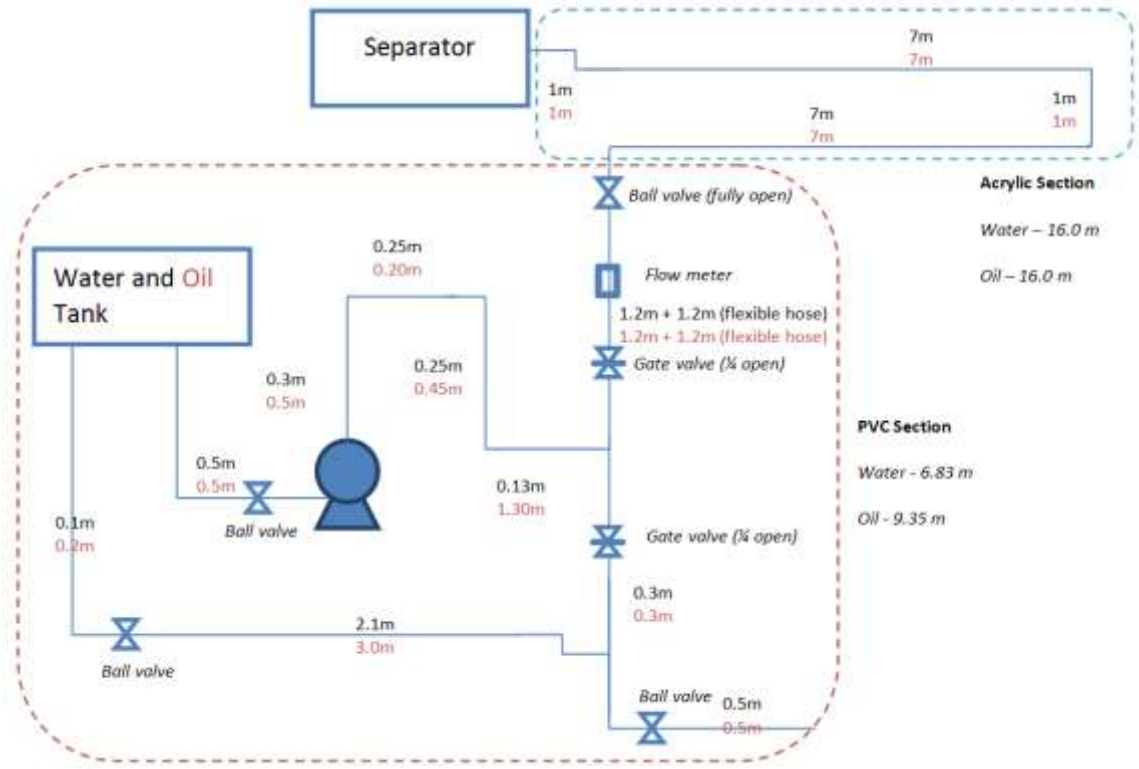

Figure B.1 Schematic diagram of the flow rig system with real pipe lengths shown

Based on the above schematic diagram, the number of existing pipe fittings and valves were counted. Elevation of test pipe section and the separator is 2 m from the ground level. Using this data, the equivalent pipe diameters were calculated which were used later in the power requirement estimation. Although the selection of the new test fluids are more or less decided towards using the silicone oil and water/glycerol mixture, it would be wise to design a system which would be capable/compatible for long term use (in case of trying other fluids) and for future students. It is also found that in two-phase flows, at the point of phase inversion there is a large change in the mixture viscosity. Based on this finding, there are many different models which predict the phase inversion point by looking at the viscosity of the fluid and the pressure drop of the flow. Therefore taking into account the necessity of the future use and physical behaviour of the fluids giving very high viscosity (than its original state when not flowing), the maximum viscosity which is 10 times greater than the oil viscosity (50 cP) is used for the pump size estimation.

First pump power estimation (pump head) was calculated by the author based on the above schematic diagram. New design and layout of the PVC pipe connections were proposed by an external company based on this initial calculation and the calculations were revised again based on the suggested new layout of the rig. Below are the calculations for the power estimation based on the new rig design.

B.4.1 Sample calculation

It is assumed that the maximum mixture flow rate in the test section is 300 L/min. However the system should be capable to vary the water fraction from 0 to 1 sustaining the constant maximum flow rate in

the test section. The system entails three sections - PVC water section, PVC oil section and the main acrylic pipe test section.

PVC pipe for water section comprises 2.65m x 1½" PVC pipe, 4 x 1½" PVC elbows, 1 x flow into T-leg, 1 x 1½ pressure sustaining valve, 1 x 17.5mm orifice plate and 1 x flowmeter. Ball valves being used are full flow and providing they are used fully open there will be negligible pressure loss across them. Return pipe-work consists 2 m x 1½" PVC pipe and 4 x 1½" PVC elbows.

PVC pipe for oil section comprises 4.51m x 1½" PVC pipe, 5 x 1½" PVC elbows, 1 x flow into T-leg, 1 x 1½ pressure sustaining valve, 1 x 17.5mm orifice plate and 1 x flowmeter. Ball valves being used are full flow and providing they are used fully open there will be negligible pressure loss across them. Return pipe-work consists 1.5 m x 1½" PVC pipe and 2 x 1½" PVC elbows.

The above circuits combine into a common acrylic test section comprising 16m x 38mm acrylic pipe, 3 x elbows 1 x ball valve and 1 x separator.

Table B.1 New fluid properties

		At 20 C		
		ρ (kg/m3)	μ (pa.s)	*n* (index)
Silicon Oil	5cP	918	0.005	1.397
Water/Glycerol	50% W	1126.3	0.006	1.39809
Average (1:1 mixture)		1022	0.050	

Calculations for 300l/min water or 300l/min oil

PVC Pipe

Internal diameter of 1½" pipe (d) = 0.041m

CSA of 1½" PVC pipe = $\pi r^2 = \pi.0.0205^2 = \pi.0.0004202 = 0.00132m^2$

Length of pipe (L) for water = Pipe length + elbows (equivalent 35 x d) = 2.65 + (4 x (35x0.041)) + (0.041x90) = 12.08m

Length of pipe (L) for oil = Pipe length + elbows (equivalent 35 x d) = 4.51 + (5 x (35x0.041)) + (0.041x90) = 15.375m

Velocity of flow (V) = Flow rate Q (m^3/s) / Area A (m^2) = 0.005 / 0.00132 = 3.79m/s

For water (using properties from Table B.1 above) calculation of Reynolds number (Re) as follows:

$Re = \rho Vd / \mu = (1126.3 . 3.79 . 0.041) / 0.006 = 29169.29$

For oil (using properties from Table B.1 above) calculation of Reynolds number (Re) as follows:

$Re = \rho Vd / \mu = (918 . 3.79 . 0.041) / 0.005 = 28529.60$

Mean height of roughness (ε) for PVC = 0.0015
Relative pipe roughness for PVC = ε/d = 0.0015/0.041 = 0.0367 ≈ 0.04

Using Moody diagram (Figure B.5) with the above calculated values for Re and ε/d the friction factor (Ø) is found to be ≈ 0.065 for both fluids.

Pressure loss for water = Ø .(L / d).(V²/2g) = 0.065.(12.08 / 0.041).(3.79² / 19.62) = 14.02m
Pressure loss for oil = Ø .(L / d).(V²/2g) = 0.065.(15.375 / 0.041).(3.79² / 19.62) = 17.85m

Recycle Stream
Length of pipe (L) for water = Pipe length + elbows (equivalent 35 x d) = 2 + (4 x (35x0.041)) = 7.74m
Length of pipe (L) for oil = Pipe length + elbows (equivalent 35 x d) = 1.5 + (2 x (35x0.041)) = 4.575m

$Re_{recycle}$ water = 1/3 x Re water = 9723
$Re_{recycle}$ oil = 1/3 x Re oil = 9510

Using Moody diagram (Figure B.5) with the above calculated values for Re and ε/d the friction factor (Ø) is found to be ≈ 0.069 for both fluids.

Pressure loss for water = Ø .(L / d).(V²/2g) = 0.069.(7.74 / 0.041).((3.79/3)² / 19.62) = 1.05m
Pressure loss for oil = Ø .(L / d).(V²/2g) = 0.069.(4.757 / 0.041).((3.79/3)² / 19.62) = 0.65m

Acrylic Pipe
Internal diameter of 37mm pipe (d) = 0.037m
CSA of 37mm acrylic pipe = πr² = π.0.0185² = 0.001075 m²
Length of pipe (L) = Pipe length + elbows (equivalent 35 x d) = 16 + (3 x (35x0.037)) = 19.885m

Velocity of flow (V) = Flow rate Q (m³/s) / Area A (m²) = 0.005 / 0.001075 = 4.65m/s

For water (using properties from Table B.1 above) calculation of Reynolds number (Re) as follows:
Re = ρVd / μ = (1022*4.65*0.037) / 0.05 = 3516
For oil (using properties from Table B.1 above) calculation of Reynolds number (Re) as follows:
Re = Same as for water since average density and viscosity is used = 3516

Using Moody diagram with the above calculated values for Re and based on smooth pipe the friction factor (Ø) is found to be ≈ 0.045 for both fluids.

Pressure loss = Ø .(L / d).(V²/2g) = 0.045*(19.885 / 0.037).(4.65² / 19.62) = 26.7m

Total Pressure Drop

Taking into account the following: -

Pressure drop across pressure sustaining valve	=	15m
Pressure drop across flow meter	=	6.8m
Pressure drop across separator	=	0.1m
Pressure drop in PVC circuit	=	14.0m
Pressure drop in PVC recycle circuit	=	1.1m
Pressure drop in acrylic circuit	=	26.7m
TOTAL PRESSURE DROP IN WATER CIRCUIT	=	***63.7m***

Total Pressure Drop

Taking into account the following: -

Pressure drop across pressure sustaining valve	=	15m
Pressure drop across flow meter	=	6.8m
Pressure drop across separator	=	0.1m
Pressure drop in PVC circuit	=	17.9m
Pressure drop in PVC recycle circuit	=	0.7m
Pressure drop in acrylic circuit	=	26.7m
TOTAL PRESSURE DROP IN OIL CIRCUIT	=	***67.2m***

B.4.2 Proposed layout and design of the new rig

The calculated pump head is used to determine the actual size of the pumps. Major changes are in the pumps and the PVC pipe fittings as for the main objectives of this upgrade. Variable speed centrifugal pumps will be used instead of fixed rate pump to save power and reduce pressure losses due to excess bypass flows. Pipes are rearranged and a number of fittings is optimised to bring down pressure loss and reduce warming of the fluids due to friction. The upgrade is now complete and the system is in use. Schematic drawings used for this process can be found on the next few pages.

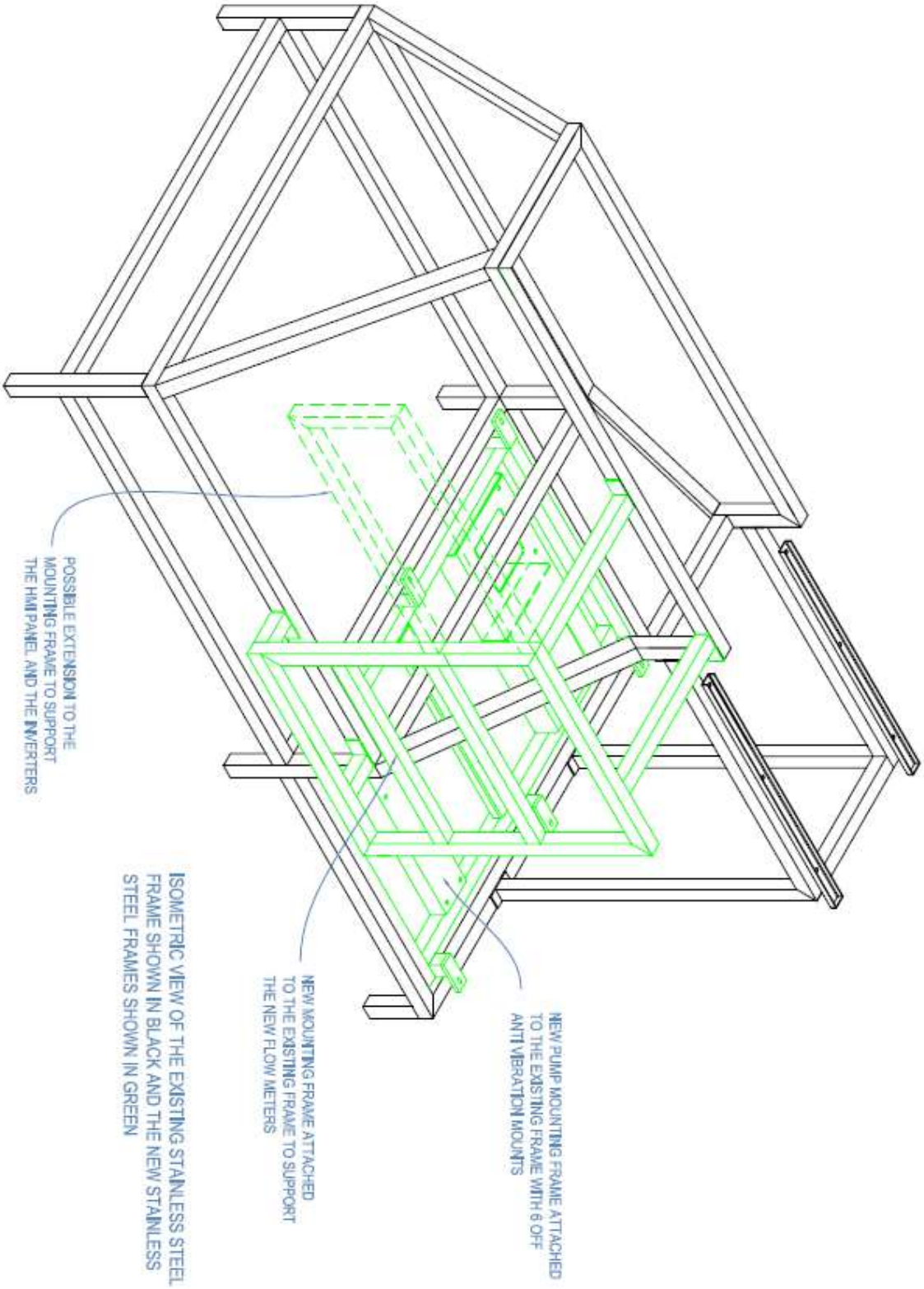

Figure B.2 Proposed design & sketch of the new metallic frame for control panel

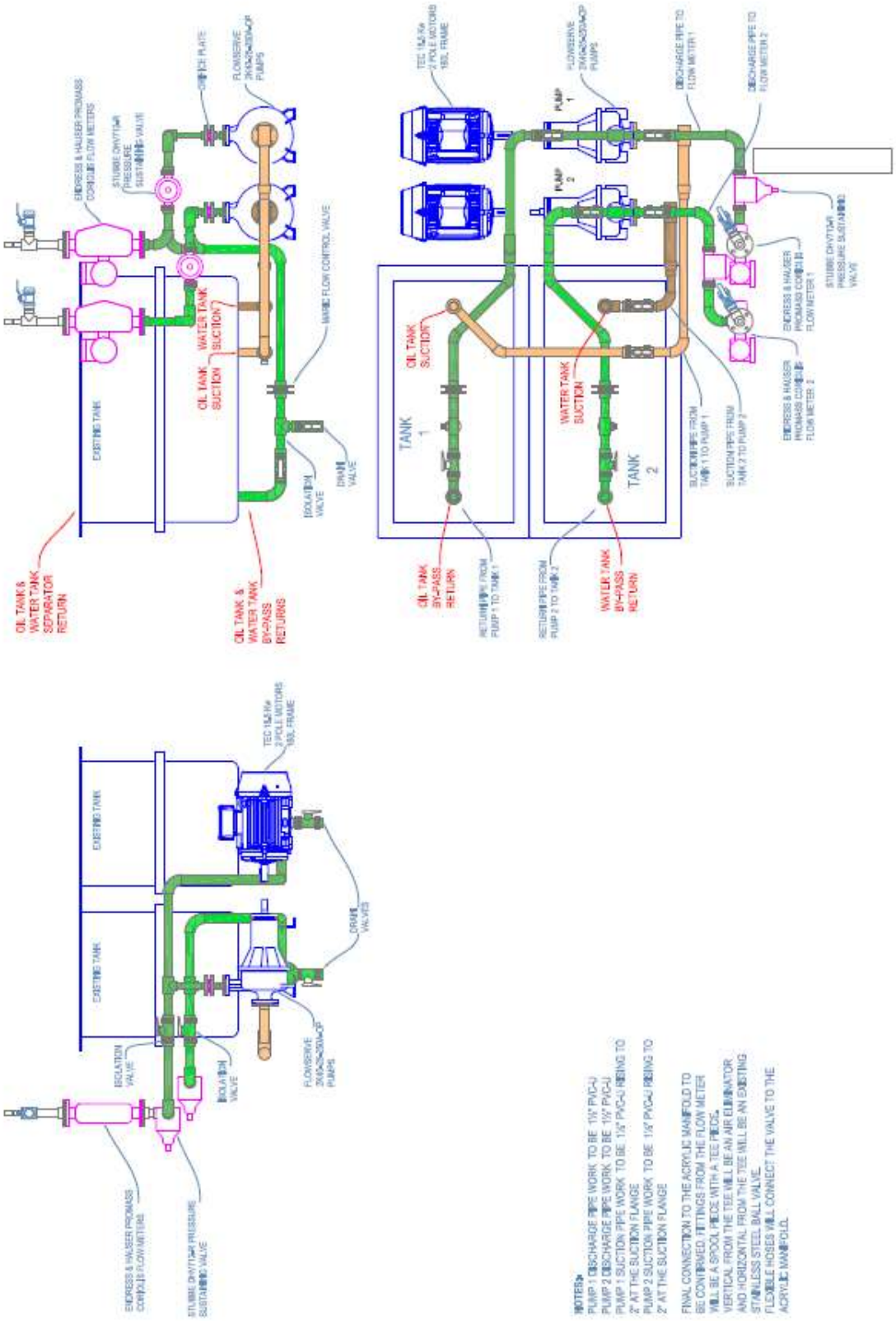

Figure B.3 Proposed design & sketch of the new pipe fittings and layout

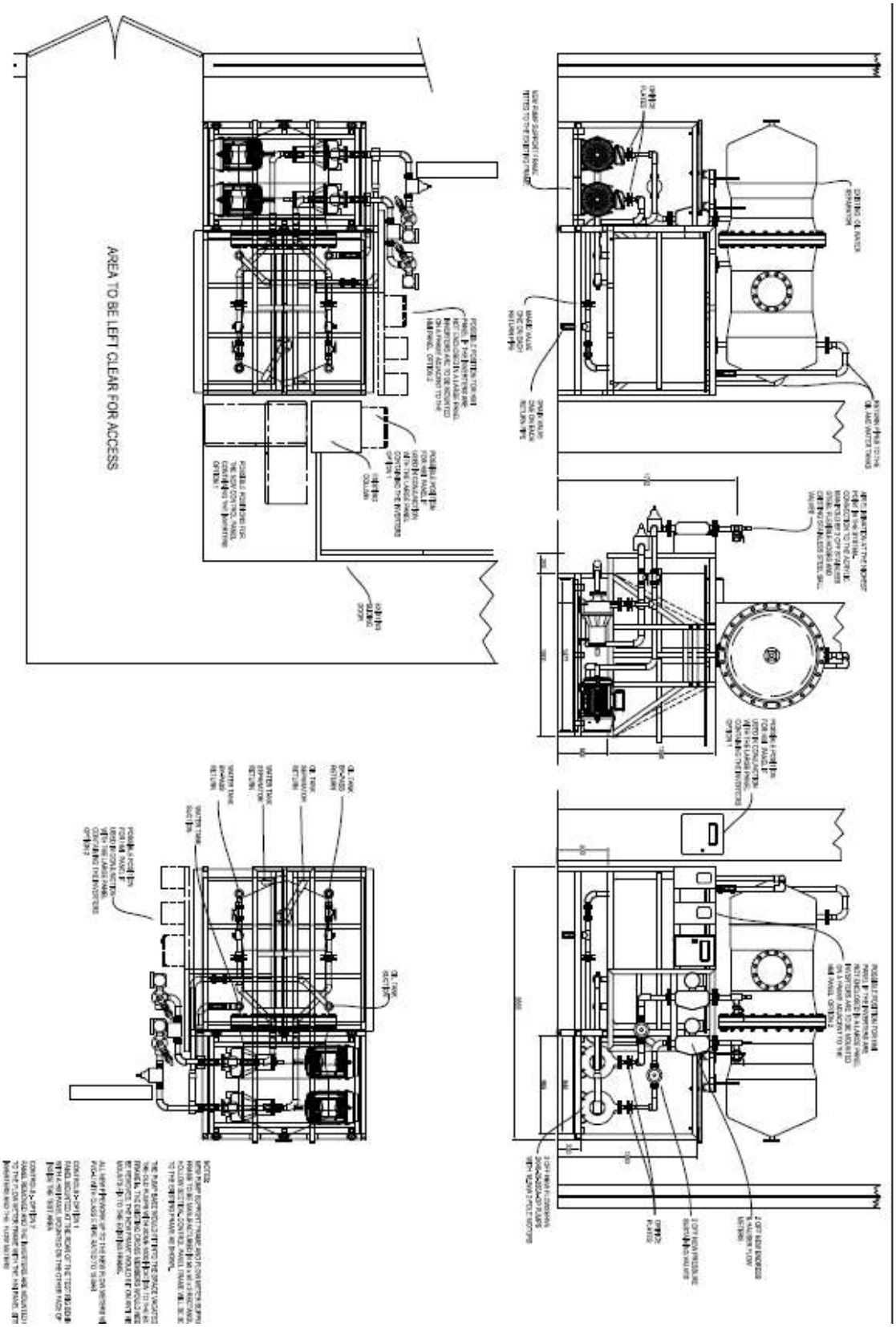

Figure B.4 Proposed design & sketch of the new pipe fittings and layout

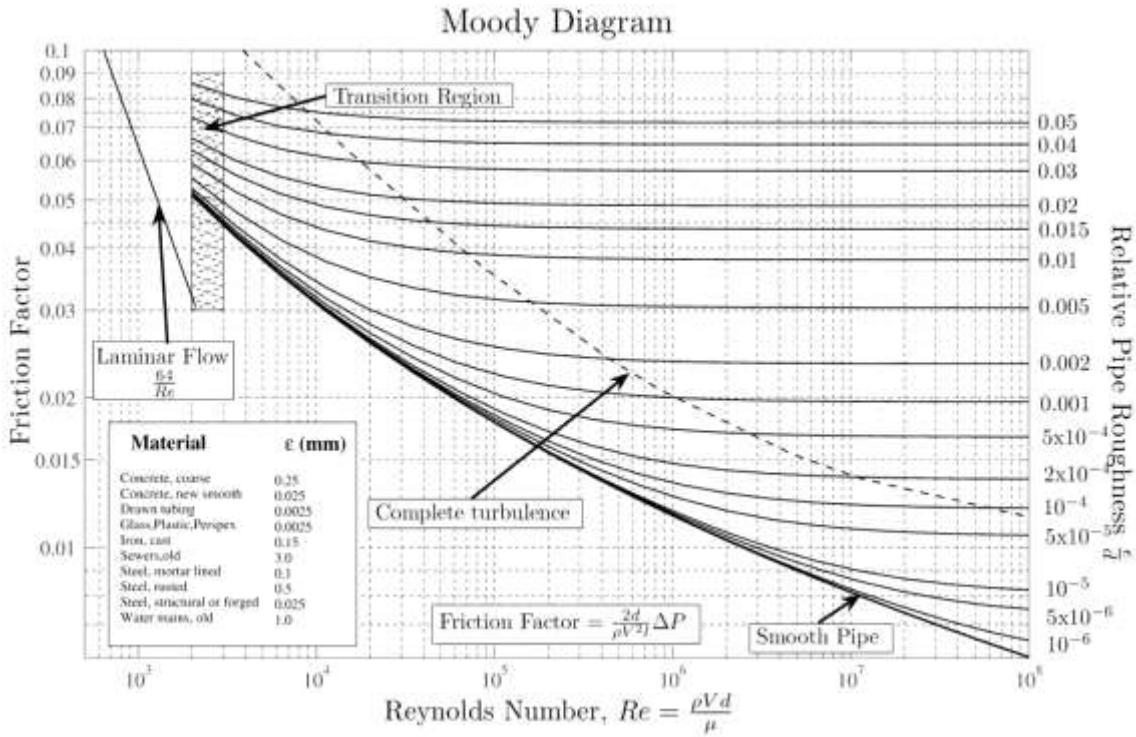

Figure B.5 Moody chart